Lancaster University

Theoretical and computational studies of the correlated ionic motion in narrow ion channels

Miraslau L. Barabash

Graduate in Physics Scientific-Research activities,
from the Belarusian State University, June 2014

Thesis submitted for the degree of
Doctor of Philosophy

Department of Physics
Lancaster University
Lancaster, UK

July 2019

Acknowledgements

I express my gratitude to my supervisors Dr. Dmitry G. Luchinsky and Prof. Peter V.E. McClintock, for supporting my love of theory, for fostering and stimulating creative thinking, and for their wisdom and sufficient patience, that assisted me not only in physics but in conveying ideas and transmitting purposefulness throughout our work. I thank Dr. Carlo Guardiani and Dr. William A.T. Gibby for maintaining the fruitful research atmosphere. I am grateful to Prof. Robert S. Eisenberg for helpful, motivating and insightful talks, as well as to Dr. Neil Drummond and Prof. Nigel Stocks for many useful comments on the essence of the work. Many thanks to Prof. Aneta Stefanovska for her pertinent comments on the subject.

I have also been fortunate to have the support of willing and patient colleagues, in particular Dr. Olena Fedorenko and her family, as well as Dr. Stephen K. Roberts and Prof. Igor A. Khovanov. Many thanks to Rev. Jonathan A. Hemmings and Dr. Kleio Kehagia. I would like to thank my office and group mates: Gemma, Valentina, Zhenia, Aleksandra, Maxime, Yunus, Mahmoud, Bastian, Federico, Hala, Saltan, Julian, Ben, and Sam for providing a light-hearted atmosphere in and outside the office.

Finally I would like to thank my Mum, Grandma and the recently deceased Grandad for their perpetual love and support.

This work was supported by a 3-year PhD Scholarship from the Faculty of Science and Technology of Lancaster University, together with writing-up support from the Engineering and Physical Sciences Research Council (grant EP/M016889/1).

Declaration

This thesis is my original work and has not been submitted, in whole or in part, for a degree at this or any other university. Nor does it contain, to the best of my knowledge and belief, any material published or written by another person, except as acknowledged in the text.

Abstract

An ion channel is a protein with a hole down its middle embedded into the cytoplasmic membrane of a living biological cells. Ion channels facilitate ionic transport across the membrane, thus bridging the intra- and extra-cellular compartments. Properly functioning channels contribute to the healthy state of an organism, making them one of the main targets for pharmaceutical applications. The description and prediction of a channel's performance — conductivity, selectivity, blocking etc., — under arbitrary experimental conditions starting from its crystal structure thus appears as an important challenge in contemporary theoretical research.

The main obstacle for such description arises from the presence of the multiple non-negligible interactions in the system. These include ion-ion, ion-water, ion-ligands, ion-pore, and other interactions. Their self-consistent consideration is essential in narrow ion channels, where due to inter-ion interactions and atomic confinement, the ions move in a single-file highly-correlated manner. Molecular dynamics, the most detailed computational tool to date, does not allow one routinely to evaluate the properties of such channels, while continuous methods overlook the ion-ion interactions. Therefore, one needs a method that combines atomic details with the ability to estimate ionic currents.

This thesis focuses on the classical treatment of ion channels. Namely, a Brownian Dynamics simulation is described where the interactions of the ion with other ions and the channel are incorporated via the multi-ion potential of the mean force (PMF). This allows one to model the channel's behaviour under various experimental conditions, while preserving the details of the structure and nanoscale interactions with atomic precision. Secondly, we use the concept of a quasiparticle to describe the highly-correlated ionic motion in the selectivity filter of the KcsA channel. We derive the quasiparticle's effective potential from the multi-ion

atomic PMF, thus connecting the quasiparticle's properties with the nanoscale features of the channel. We also evaluate the rates of transition between different quasiparticles by virtue of the BD simulation. These ingredients comprehensively describe the quasiparticle's dynamics which hence serves as an intermediary between the crystal structure and the experimentally observed properties of a narrow ion channel.

Lastly, an analytical method to describe the ion-solvent interaction is proposed. It incorporates the ion-solvent and ion-lattice radial density functions, and hence automatically accounts for the pore shape, the type of atoms comprising the lattice, the type of solvent, and the ion's location near the pore entrance. This method paves the way to an analytical decomposition of single-ion PMFs, what is of fundamental importance in predicting the conductive and selective properties of mutated biological ion channels. This method can also find application in designing functionalized artificial nanopores with on-demand transport properties for efficient water desalination.

List of publications

Peer-reviewed papers:

1. C. Guardiani, W. A.T. Gibby, **M. L. Barabash**, D. G. Luchinsky, P. V. E. McClintock, Exploring the pore charge dependence of K+ and Cl- permeation across a graphene monolayer: a Molecular Dynamics study, RSC Adv., **9**, 20402 (2019)

2. **M. L. Barabash**, W. A.T. Gibby, D. G. Luchinsky, C. Guardiani, I. A. Khovanov, and P. V. E. McClintock, The dynamics of quasiparticles in a toy model of the KcsA biological ion channel, EasyChair Preprint no. 966 `https://easychair.org/publications/preprint/s8ZP`, *25th International conference of noise and fluctuations (ICNF)*, 18-21 June 2019, Microcity, Neuchâtel, Switzerland

3. C. Guardiani, **M. L. Barabash**, W. A. T. Gibby, D. G. Luchinsky, I. A. Khovanov, P. V. E. McClintock, Prehistory probability distribution of ion transition through graphene nanopore C. Guardiani, EasyChair Preprint no. 930 `https://easychair.org/publications/preprint/DgZX`, *25th International conference of noise and fluctuations (ICNF)*, 18-21 June, Microcity, Neuchâtel, Switzerland

4. W. A. T. Gibby, **M. L. Barabash**, C. Guardiani, D. G. Luchinsky, P. V. E. McClintock, Statistical theory of mixed-valence selectivity in biological ion channels, EasyChair Preprint, *25th International conference of noise and fluctuations (ICNF)*, 18-21 June, Microcity, Neuchâtel, Switzerland

5. D. G. Luchinsky, H. Hafiychuk, **M.L. Barabash**, V. Hafiychuk, T. Ozawa, K. Wheeler and P.V.E. McClintock, Atomistic model of reptation at polymer interfaces, EasyChair Preprint no. 931 `https://easychair.org/publications/preprint/b8BN`, *25th International conference of noise and fluctuations (ICNF)*, 18-21 June, Microcity, Neuchâtel, Switzerland

6. **M. L. Barabash**, W. A. T. Gibby, C. Guardiani, D. G. Luchinsky, P. V. E. McClintock, From the potential of the mean force to the quasiparticle's effective potential in narrow ion channels, Fluct. Noise Lett. **18**(2) 1940006

7. W. A. T. Gibby, **M. Barabash**, C. Guardiani, D. G. Luchinsky, O. Fedorenko, S. K. Roberts, P. V. E. McClintock, Theory and experiments on multi-ion permeation and selectivity in the NaChBac ion channel, Fluct. Noise Lett. **18**(2) 1940007

8. W. A. T. Gibby, **M. Barabash**, C. Guardiani, D. G. Luchinsky, and P. V. E. McClintock, The role of noise in determining selective ionic conduction through nano-pores, *IEEE 13th Nanotechnology Materials and Devices Conference (NMDC)*, IEEE Xplore, DOI: 10.1109/NMDC.2018.8605825

9. D. G. Luchinsky, W. A. T. Gibby, I. Kh. Kaufman, **M. L. Barabash**, D. A. Timucin, and P. V. McClintock, Multicomponent Conduction and Selectivity of Biological Channels, Biophys. J., **114**(3), Suppl. 1 (Meeting abstract), 480a

Conference presentations and workshops:

1. **M. L. Barabash**, W. A.T. Gibby, D. G. Luchinsky, C. Guardiani, I. A. Khovanov, and P. V. E. McClintock, The dynamics of quasiparticles in a toy model of the KcsA biological ion channel, *25th International Conference on Noise and Fluctuations (ICNF)*, 18-21 June 2019, Neuchatel, Switzerland

2. W.A.T. Gibby, **M.L. Barabash**, C. Guardiani, D.G. Luchinsky, P.V.E.McClintock, Statistical theory of mixed-valence selectivity in biological ion channels, *25th*

International Conference on Noise and Fluctuations (ICNF), 18-21 June 2019, Neuchatel, Switzerland

3. C. Guardiani, M.L. Barabash, W.A.T. Gibby, D.G. Luchinsky, I.A. Khovanov, P.V.E. McClintock, Prehistory probability distribution of ion transition through graphene nanopore, *25th International Conference on Noise and Fluctuations (ICNF)*, 18-21 June 2019, Neuchatel, Switzerland

4. D. Luchinsky, H. Hafiychuk, **M. Barabash**, V. Hafiychuk, T. Ozawa, K. Wheeler, P. McClintock, Atomistic model of reptation at polymer interfaces, *25th International Conference on Noise and Fluctuations (ICNF)*, 18-21 June 2019, Neuchatel, Switzerland

5. **M. L. Barabash**, W. A. T. Gibby, C. Guardiani, D. G. Luchinsky, P. V. E. McClintock, The motion of quasiparticles in the toy model of the biological KcsA ion channel, poster at *Statistical Physics of Complex Systems*, 6-11 May 2019, NORDITA, Stockhom, Sweden

6. P.V.E. McClintock, **M. L. Barabash**, W. A. T. Gibby, C. Guardiani, D. G. Luchinsky, Statistical Physics of Ions in Narrow Biological Ion Channels, Invited talk at *Statistical Physics of Complex Systems*, 6-11 May 2019, NORDITA, Stockhom, Sweden

7. **M. L. Barabash**, W. A.T. Gibby, D. G. Luchinsky, C. Guardiani, I. A. Khovanov, and P. V.E. McClintock, The Motion of Quasiparticles in the Model of the Biological KcsA Ion Channel, poster at *Physics of Biological Oscillators (POBO)* workshop, 27 Nov – 01 Dec, Chicheley Hall, UK.

8. D. G. Luchinsky, W. A. T. Gibby, I. Kh. Kaufman, M. Barabash, D. A. Timucin, and P. V. E. McClintock, "Multicomponent conduction and selectivity of biological channels", Biophysical Journal 114, 480A (2018) (meeting abstract)

9. **M. L. Barabash**, W. A.T. Gibby, D. G. Luchinsky, C. Guardiani, I. A. Khovanov, and P. V.E. McClintock, Dynamics of quasiparticles: from molecular dynamics to ionic current, Invited talk at the *8th International conference on Unsolved problems of noise (UPoN)*, 9-13 July, Gdansk, Poland.

10. P.V.E. McClintock, **M. L. Barabash**, W. A. T. Gibby, C. Guardiani, D. G. Luchinsky, Invited talk at *Stochastic Dynamics in Biological Ion Channels*, 05.09.2017, Krakow, Poland

11. M. Barabash, A. Stefanovska, "Model of membrane-potential fluctuations", European Study Group on Cardiovascular Oscillations (ESGCO) April 2016

Contents

List of Tables

List of Figures

Physical constants

Symbol	Name	Value
c	Speed of light	$2.999 \cdot 10^{8}$ m/s
e_0	Charge of electron	$1.68 \cdot 10^{-19}$ Q
N_A	Avogadro constant	$6.022 \cdot 10^{23}\ mol^{-1}$
k_B	Boltzmann constant	$1.38064852(79) \cdot 10^{-23}\ J \cdot K^{-1}$

List of symbols

ϵ	Dielectric permittivity
ϵ_0	Dielectric permittivity of vacuum
D	Diffusivity
ρ	Particle or probability density
k	Boltzmann constant
T	Absolute temperature
α, β, γ, ... (Greek indices)	Ionic species
i, j, k, ... (Latin indices)	Individual ions
ϕ	Electrostatic potential
$\mathbf{E}$	Electrostatic field
$\mathbf{D}$	Electrostatic displacement field
$\mathbf{P}$	Electrostatic polarization field
μ	Chemical potential
$\bar{\mu}$	Excess chemical potential
m	Mass of an ion
$\mathbf{r}$	Radius-vector of an ion
q_N	Position of the N-ion quasiparticle
c_i	Ionic charge
D^α	Diffusivity of species α
$g(\mathbf{r})$	Radial density function
W	Potential of the mean force
G	Helmholtz free energy
ξ	White random noise
γ	Friction coefficient
$\mathbf{v}$	Velocity
$\mathbf{F}$	Force

Nomenclature

AA	All-atom
AMFE	Anomalous mole-fraction effect
ATP	Adenosine triphosphate
BBGKY	Bogolyubov-Born-Green-Kirkwood-Yvon (hierarchy)
BD	Brownian dynamics
BVP	Boundary value problem
CC	Coupled cluster
CG	Coarse-grained
CM	Continuous mechanics
DCK	Differential Chapman-Kolmogorov (equations)
DFT	Density functional theory
EnVarA	Energy variational analysis
FEM	Finite-element method
FP	Fokker-Planck
GCMC	Grand Canonical Monte Carlo
ICB	Ionic Coulomb blockade
IS	Implicit solvent
KcsA	A potassium-selective ion channel
M	Molar, same as mol/litre (1M = 10^3 mol/m^3 = 0.6022 particles/(nm)^3)
MD	Molecular dynamics
MFPT	Mean first-passage time
MM	Molecular mechanics
NaChBac	A sodium-selective ion channel
PNP	Poisson-Nernst-Planck
PB	Poisson-Boltzmann
PMF	Potential of the mean force
QM	Quantum mechanics
QP	Quasiparticle
RDF	Radial distribution function
SF	Selectivity filter

In memory of my grandfather

To my mother and grandmother,

with love and gratitude

1. Introduction

> There is nothing more practical
> than a good theory.
>
> *A. Einstein*

The human body consists of many organs, each of which consists of millions of cells, which represent the smallest functional units. Their functionality is based on the presence, amount, and exchange of physiologically important ions. These include but are not limited to K^+, Na^+, Ca^{2+}, Mg^{2+}, Cl^- and some other ions. The transport of ions occurs via three types of transporters embedded into the cellular membrane: (1) pumps, (2) cotransporters and (3) ion channels. While the pumps require adenosine triphosphate (ATP) to move ions against their electrochemical gradients, co-transporters use the gain of moving one ionic species down its electrochemical gradient to move another species up [2–4].

Ion channels are complex proteins providing fast and selective passive transport of ions down their electrochemical gradient. The proper operation of ion channels defines whether the organism stays in a healthy state or a disease evolves. Given that the total number of all ion channels is very large [5], the list of these diseases is quite extensive: channelopathies (malignant hyperthermia, influenza, diabetes, central core disease, neurological disorders, autoimmune diseases), Liddle syndrome, epilepsy, cystic fibrosis, dominant hearing loss, arrythmias, chronic pain, asthma etc. [6, 7]. That is why 15% of all drugs in the world primarily target the ion channel [8]. This apparent complexity of diseases results from channel's inabil-

ity to present its specific properties (functions), which are conductivity, selectivity, rectification, as well as response to external stimuli (e.g. voltage changes, presence of Ca or Mg, pH level). It is the structure of an ion channel that defines this range of functions. Predicting and controlling these properties given the crystal structure represents the ultimate challenge of the ongoing research [2].

Other than biology, a growing challenge is water quality. According to the World Health Organization, "each and every day some 3,900 children die because of dirty water or poor hygiene; diseases transmitted through water or human excrement are the second-leading cause of death among children worldwide, after respiratory diseases" [9]. Indeed, many researches indicate growing lack of pure water and the consequences it imposes on human health [10]. One of the promising solutions is the creation of highly efficient and cheap desalination structures based on functionalised graphene layers [11]. An efficient technique to find the optimal crystal structure appears on the front edge of the industrial requests.

The aforementioned biological and technological challenges share the same root. Namely, they require a reliable description of ionic and water permeation at the nanoscale. The difficulty arises from the fact that at the nanoscale many entities interact with each other. These interactions include ion-ion, ion-water, ion-amino acid (in ion channels) or ion-carbon (in artificial graphene nanopores), water-water etc. All these contribute to the permeation in a complex way.

Molecular dynamics provides a very detailed tool to investigate nanopores of all kinds. It incorporates all of the aforementioned interactions, in addition to the applied electric field which is required to study ion transport. However, only simple artificial and a small selection of biological structures have been described so far. Moreover, due to the nature of the force fields (see more in Chapter 2) the comparison with experimental data reveals an order-of-magnitude discrepancy [12]. These simulations are also time and resource consuming, which makes the derivation of multiple data points (e.g. to build I-V or I-C curves) almost impossible. Thus, the application of theory to real experimental data is almost impossible due to the

gap between the methods' timescales, as shown in Fig. 1.1. This linking, however, is the key to the biological and technological applications [13].

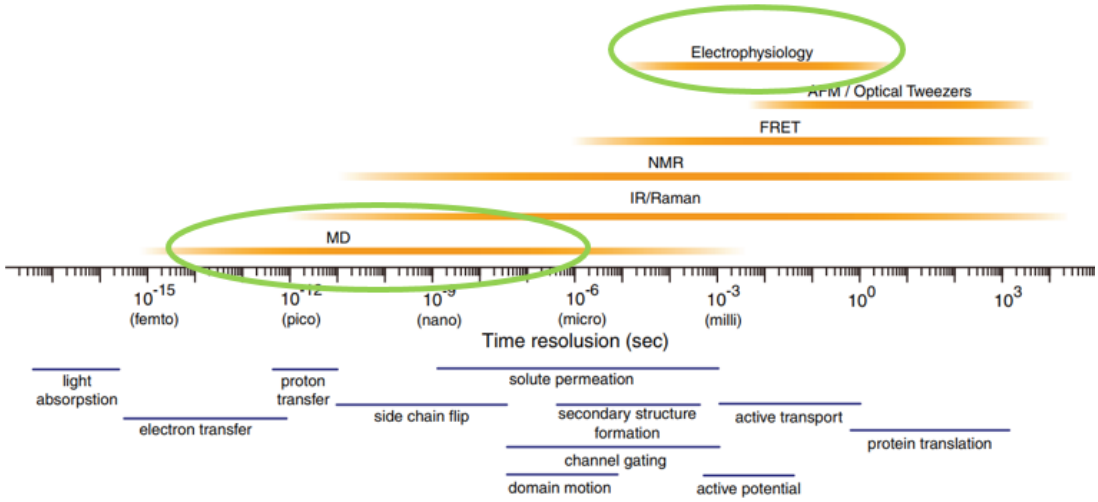

Figure 1.1: Computational and physiological timescales. Linking the gap between the timescales of structure-based computations and electrophysiological measurements is the ultimate goal of the ongoing research and the present thesis. Adapted from Ref. [14].

1.1 Goals and structure of the thesis

The ultimate goal of the present work is to connect the crystal structure of an open channel with the ionic current through it, while incorporating the essential physical effects. Ultimately, such a theoretical model should encompass the scales of time, space and electrolytes' concentration [15], concisely summarize the data [16] and be able to successfully predict ionic currents in new environments and mutated channels [2]. In this task, the most promising method is molecular dynamics (MD). It provides the most detailed classical description of the interactions between the entities involved. However, even with the most powerful supercomputers, only a few channels have been simulated to calculate ionic current. However, even these calculations may reveal discrepancy with the experimental data [12].

Often one-dimensional MD-generated potentials of the mean force (PMFs), which include the important interactions, are incorporated into the Nernst-Planck equation to calculate the current through the channel. However, in doing so the,

the ion-ion interactions are overlooked. This is crucial in narrow channels where ions interact strongly, resulting in highly coordinated motion. Therefore, one needs a method which can combine the level of detail provided by classical MD with the fast and self-consistent calculation of ionic current.

In this thesis, we propose a method to connect the important information from classical MD including the multi-ion energy landscape with the current through the channel. Namely, we use the concept of quasiparticles to describe the correlated ionic motion through a narrow channel. First, we embed the MD generated PMFs into Brownian dynamics (BD) via a bespoke BD simulator. This is an important step as it allows us to incorporate the atomic details of interactions within the channel and previous solvers cannot do this. Ionic currents can be calculated from the BD simulation which can be verified against experimental/MD data.

Secondly, we provide an analytical (probabilistic) description of the correlated ionic motion in a narrow selectivity filter by means of the concept of a quasiparticle (QP). We connect the effective potential, governing the motion of the QP, with atomistic PMFs obtained in MD simulations. We also show that the motion of an ion in the channel mouth is correlated with the motion of the QP. These steps are essential to connect the detailed atomic structure to the transport properties of the pore, and to further compare theoretical predictions with experimental ionic currents.

Of particular importance is the ion-water (hydration) interaction of the ions in both the bulk solution and the pore. To further understand this interaction we provide a novel method to calculate the water structure surrounding an ion and graphene nanopore using the ions radial distribution function (RDF). Thus one get a fast estimation of the energy landscape which in turn can help to understand conductive/selective properties of functionalized artificial nanopores and to design new ones with pre-defined required properties.

In Chapter 1 we provide a general introduction and outline the problems that are tackled in the thesis. In Chapter 2 we outline the arsenal of methods and

discuss their strengths and weaknesses. This chapter also formulates the main research lines of this dissertation. Chapter 3 describes a Brownian dynamics simulation system we have developed, including a justification of the choice of its ingredients. In Chapter 4 the correlated motion of ions in narrow nanopores is described through the concept of a quasiparticle. In chapter 5 we discuss a new method to decompose a PMF in terms of radial distribution functions (RDFs). Finally, chapter 6 summarises the contributions and suggests a number of topics for future works.

1.2 Properties of channels

1.2.1 Conduction

The primary property of ion channels and artificial nanopores is their ability to conduct ions. This process is controlled by the laws of electrodiffusion – the driving force stems from the chemical and electric gradients. In bulks and wide channels, as well as channel cavities, ions can overtake each other in physical space and thus motion is not single-file [17, 18]. In contrast, the selectivity filters (SFs) of very narrow channels such as KcsA [17, 19, 20] prohibit large spatial deviation of ions from the channel's axis and therefore the ionic motion is essentially one-dimensional. While transiting from the channel's cavity into the SF, individual ions do not face a significant energy barrier [21].

Single-file conduction The situation changes drastically when the motion of a charged particle is restricted – ions move in single file [2, 22]. This is evident in narrow ion channels [23] and artificial nanopores [24]. One has to consider carefully ion-ion, ion-water, ion-ligand and ion-electrostatic fields to correctly describe the behaviour of the system. For instance, in the KcsA channel due to the strong inter-ion interactions, ions are found to permeate in a highly-correlated manner [19,23] called "knock-on". This type of conduction resembles a Newton cradle: an

incoming ion is required to "knock" the neighbouring ion (and it in turn knocks its neighbouring ion) so that the outermost ion exits the channel [25,26]. This type of conduction requires an extremely well-tuned energy balance, where the repulsion between ions and the dehydration barrier is counterbalanced by the attraction to ligands (carbonyl groups) forming the binding site [27].

Classical barrier-less permeation, implying that an ion does not face an energy barrier while traversing through the narrow channel, is reminiscent of the inherently quantum phenomenon of superconductivity where current flows without resistance. Both phenomena are of a collective nature and correlations play an essential role [28].

Saturation of currents It was found experimentally that the current-concentration curve at a fixed voltage reveals a sublinear, not linear, dependence on concentration: $I/V = \sigma = \sigma_0/(1 + C_s/C)$. Here σ_0 is the conductance at large concentrations, C_s is the saturation concentration at half-maximum of current and C is the concentration of the given solution. This phenomenon, known in relation to enzymes as Michaelis-Menten saturation [29], occurs because the ion channel can conduct only one ion at a time [30].

1.2.2 Selectivity

Being closely related to conduction, the selectivity of ion channels represents their ability to distinguish between different permeating ionic species. It is characterized as a ratio between current magnitudes of different ionic species [2,31]. The simplest rejection of a solute molecule occurs when its smallest dimension is larger than the diameter of the pore [24]. When the molecule or ion size is smaller than or equal to the pore diameter, selectivity results from two opposite effects: ionic attraction to the channel's charged atoms (e.g. negative amino acids) and the energy to strip off the water molecules [32, 33]. The interplay and quantitative differences in the interaction energies [34] lead to different types of selectivity: by sign of charge,

valence, and ionic size.

By sign (e.g. K^+ *vs.* Cl^-). In a solution, ions start interacting at the Debye length. Beyond comparable distances, there is no selectivity by charge. If the spatial separation is smaller than the Debye length, ionic repulsion or attraction comes into play. Thus, ion channels and nanopores start distinguishing ions by their charge e.g. between K^+ and Cl^- [35, 36].

By valence (e.g. Ca^{2+} *vs.* Na^+). A second type of selectivity implies distinguishing ions by their valence. This kind of selectivity emerges in Ca^{2+} channels [37] between Ca^{2+} and Na^+ ions, the ions that possess very close radii – 0.99Å and 0.95Å, respectively, although different charges. The domination of Ca^{2+} translocations over Na^+ in calcium channels can be explained in electrostatic terms, as a Ca^{2+} ion residing at the binding site can be replaced only by another Ca^{2+} ion and thus blocks the Na^+ pathway; repulsion by a Na^+ ion is insufficient to overcome the attraction imposed by the charged residue of the site [37].

On the other hand, the domination of Na^+ over Ca^{2+} in sodium channels suggests that the Ca^{2+} ions experience a barrier due to incomplete dehydration in the selectivity filter of these channels, in contrast to Na^+ ions [38]. The dimensions of the pore suggest that Na^+ ions are able to bypass Ca^{2+} ions inside the pore, which leads only to the attenuation, instead of complete blocking, of Na^+ currents [38].

By size (e.g. K^+ *vs.* Na^+) Thermodynamic selectivity between alike-charged ions originates from the difference between their radii. Smaller ions have stronger electrostatic field which leads to tighter binding and orientation of water molecules. The denser cloud of the water molecules suggests a higher dehydration barrier and stronger ion-ligand interaction in the channel, thus contributing to the change of the ion's free-energy $\Delta G(X) = \Delta G_{pore}(X) - \Delta G_{bulk}(X)$ while moving from the bulk to the channel [27, 39–43]. It is the difference between the free-energy changes

of two ions which defines selectivity. Numerically, this reads as

$$\Delta\Delta G(Na^+ \to K^+) = [G_{pore}(Na^+) - G_{bulk}(Na^+)] - [G_{pore}(K^+) - G_{bulk}(K^+)]$$

The larger the difference $\Delta\Delta G$, the more selective the channel.

The value ΔG_{bulk} is defined by the ion-water interactions (hydration) in free bulk, while ΔG_{pore} defines that in the channel. The latter includes the interactions with the remaining coordinating waters, the residue of the amino acids and ligand–ligand interactions [44]. These microscopic interactions form the basis of almost barrier-less permeation of K^+ ions in the KcsA potassium channel [19, 27] whereas it rejects e.g. Na^+ ions [27].

The Na^+/K^+ selectivity is usually measured under asymmetrical biionic conditions [45]. In this experiment one of the bulks is filled by, say, KCl while the other one contains NaCl. By measuring the reversal potentials – the transmembrane voltage at which the electric current vanishes, – one extracts information about the K^+/Na^+ selectivity [45].

1.2.3 Anomalous mole-fraction effect

The anomalous mole-fraction effect (AMFE) suggests the non-monotonic dependence of the current through, for instance, a Ca^{2+} channel on increasing the proportion of Ca^{2+} in washing solutions, when both Na^+ and Ca^{2+} ions are present in both solutions. This non-monotonic dependence is revealed as a dip in current, see Fig. 1.2. The explanation reads as follows [47]. At low concentration of Ca^{2+}, Na^+ ions permeate through the channel. Increasing the concentration of Ca^{2+} ions to the μM range [48] increases the probability of blockage of the pore by Ca^{2+} ions, as only another Ca^{2+} ion, not a Na^+, can push through the resident one. With increasing the Ca^{2+} concentration, the probability of pushing increases which results eventually in a increase of current [17, 37] which by now is a C^{2+} current.

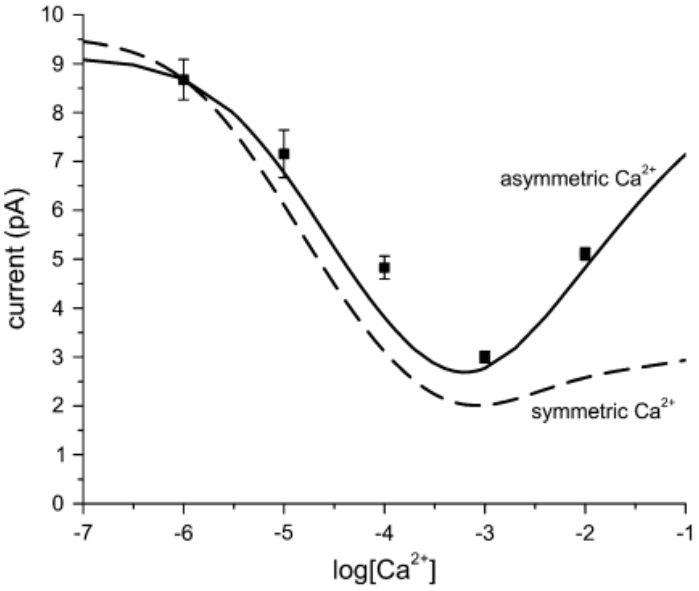

Figure 1.2: Anomalous mole-fraction effect implies non-monotonous change of the current through the channel with increasing mole fraction of one of the ionic species in solutions across the membrane. Reprinted from Ref. [46] with permission from Elsevier.

1.2.4 Activation / inactivation and gating

In addition to their ability to selectively conduct ions, ion channels are capable of sensing external stimuli affecting the closed/open state of the pore. This is referred to as gating, although gating and activation / inactivation are often used interchangeably. By inactivation we denote the ability of the channel to open, while the gating can be represented by the stochastic telegraph noise [49] of openings and closings occurring faster than 1 or 2 μs [50]. This random switching may occur between non-conductive and multiple conductive states [51]. External stimuli can include voltage [52], temperature, pressure, osmotic pressure [53], stretching of the lipid bilayer [54], and the presence of other ions or molecules [2].

A voltage-gated channel possesses a voltage sensor domain, containing a so-called S4 helix which consists of charged arginines [52]. When external voltage is applied, this helix slides along the electric field, translocating the charge [6], and pulls the S4-S5 linker. This in turn bends the S6 segment and opens the pore [55, 56]. This *sliding-helix* mechanism is becoming the common view on

voltage sensing [52].

1.3 Example: KcsA biological ion channel

KcsA (potassium crystallographically-sited activation) is arguably the most studied channel. Since the discovery of its crystal structure in 1998 [19], this channel has become the target and reference specimen on which theoretical models are calibrated. The reason for such a high interest stems from one of its structural features — the presence of the TTVGYG amino acid sequence (**T**hreonine, **V**aline, **G**lycine, T**y**rosine) in its selectivity filter. This sequence is said to be conserved because it is present in most potassium channels, including eurkaryotic channels [2]. Hence, one can extrapolate the mechanisms of permeation and selectivity in this channel to other representatives of the K_v (potassium voltage-gated) superfamily.

The structure of the pore reminds one of an inverted teepee due to its intracellular gate at the bottom [19] (Fig. 1.4). The narrowest part (SF) is highlighted by point 2 and has an average diameter of ~ 2.8Å [59]. It is here that selectivity between different species occurs because this pore can accommodate one dehydrated K^+ ion but not Na^+. The narrowness of the SF prohibits the ions from passing each other during permeation, which results in the highly-correlated single-file conduction through this channel [60–62]. Meanwhile the intracellular cavity (point 4) has an average diameter of ~ 10Å.

The SF is 12Å long and consists of 5 sites, formed by the amino acids carbonyl `C=O` oxygen atoms, where essentially dehydrated ions can bind [63]. Each binding site is formed by 8 carbonyl oxygen atoms [63]. The proximity of ions suggests that their strong Coulomb repulsion leads to rapid conduction [19,59]. Classically, it is assumed [19, 26] that K^+ ions are separated by at least one water molecule. This chain has been observed in MD simulations [31, 60], but also in streaming potential experiments where approximately one water molecule accompanies each permeation through the SF [26]. The ions undergo a soft knock-on mechanism suggesting the pore occupancy changes as $2 \to 3 \to 2$ [19,25,64,65]. However, recently

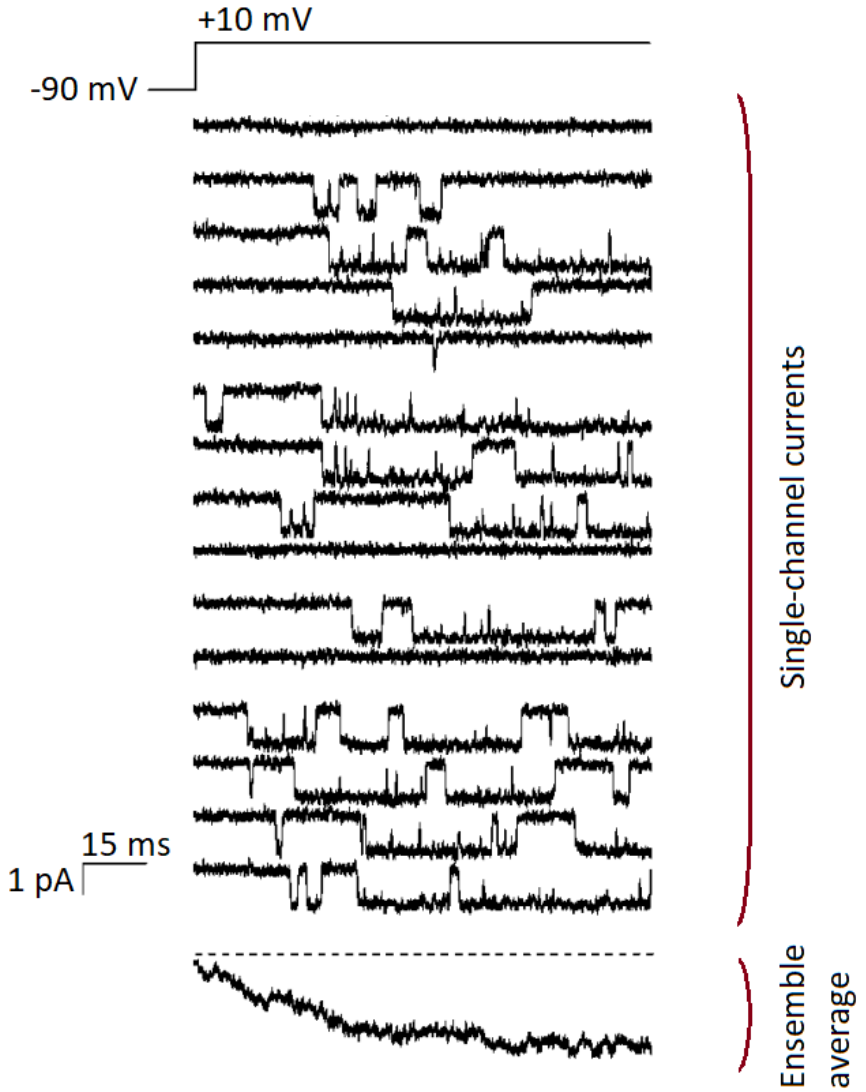

Figure 1.3: Gating and activation of ion channels. At a negative voltage, ion channel is shut and no current flows through it. Once the voltage step is applied, the ion channel activates what is illustrated by step-like noisy traces. These traces, taken from various channels, sum up to the whole-cell current, which is proportional to the ensemble average shown in the bottom picture. The top depicts the voltage pulse protocol stepping from the holding potential of -90 mV to the test potential +10 mV. Bars indicate the time and current scales. Adapted from [57].

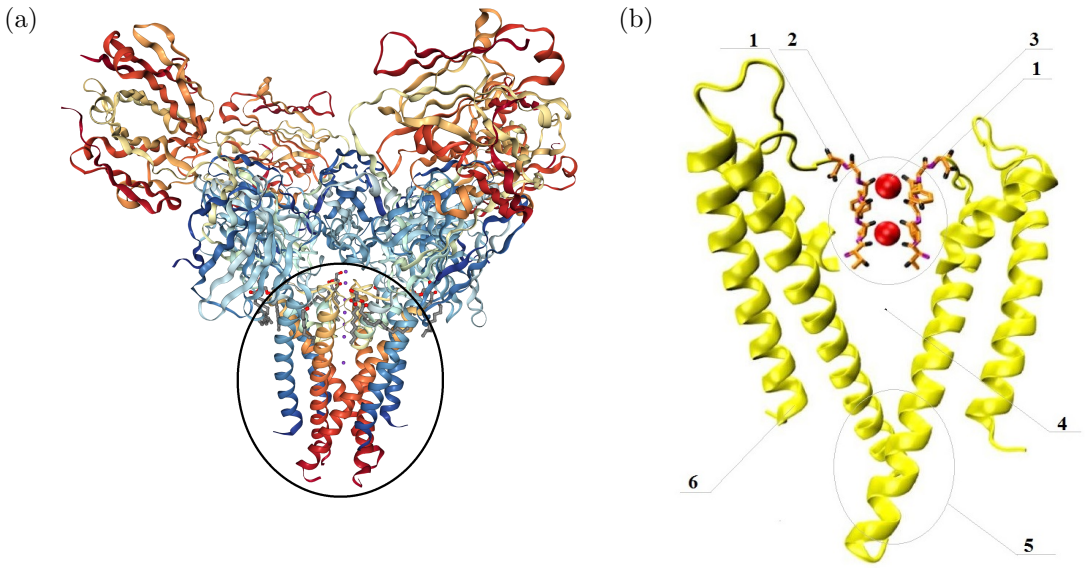

Figure 1.4: (a) Overall structure of the biological KcsA ion channel. The channel consists of four identical subunits each of which includes alpha-helices (shown as spirals) forming the pore region. The black ellipse encircles the pore domain embedded intro the cytoplasmic membrane. The bushy structure on the top is washed by the extracellular solution. (b) The pore domain and the selectivity filter of the KcsA ion channel. The number indicate the elements of the KcsA channel: 1 – aminoacid chain, 2 – selectivity filter, 3 – permeable ion, 4 – central cavity, 5 – gate, 6 – alpha helices of the backbone structure (only two of four alpha helices are shown). (Images generated in VMD [58].)

evidence of hard direct knock-on has been published, based on two-dimensional infrared spectroscopy, indicating that KcsA may conduct ions without interleaving waters [66, 67] as $3 \rightarrow 4 \rightarrow 3$. Although this finding seemingly disagrees with the streaming potential experiments [26], the 2D infrared spectra [68] have been shown to be compatible with the direct knock-on mechanism [67]. Moreover, the two permeation mechanisms possibly coexist [21].

Experimental measurements of current are abundant [69–74]. Typically this channel reveals $\sim$ 7pA current saturation at concentration of $\sim$ 100mM and voltage $\sim$ 100mV, further saturating with the increase of the concentrations and voltage [75]. It favours K over Na at ratios of 1000:1 [39]. The KcsA channel is found to be blocked by intracellular Na^+ [73], or by the presence of Ba^{2+} in either bulk [76]. A number of MD simulations are able to shed light onto the permeation mechanism [77–81]. But there is disagreement here, and even the best estimates of experimental current are almost two orders of magnitude too small [12].

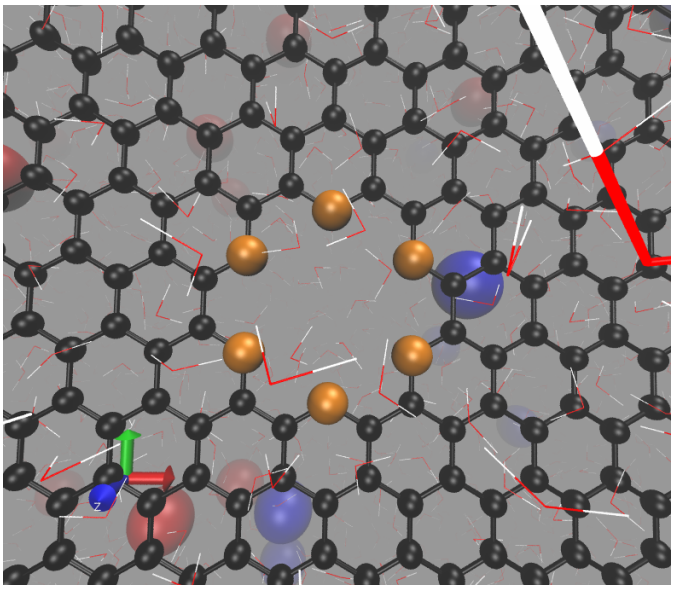

Figure 1.5: Functionalised artificial graphene nanopore. Carbon atoms are shown by black balls, ions are red and blue spheres, water molecules are represented by red and white triangular lines. The golden spheres represent the embedded atoms of another material to illustrate functionalization.

1.4 Applications of nanochannel models

Ion channels, drugs, DNA sequencing As mentioned above, a successful quantitative theoretical method to describe the characteristics of ion channel function in response to experimental settings may lead to a number of goals. One of the first applications lies in the field of medicine, where the design of new efficient drugs is of primary importance [7]. This includes creation of anaesthetics, antibacterial poisons and antidotes to venoms, efficient inhibitors, antibiotics. Secondly, the now growing field of DNA sequencing suggests a fast, ultimately real-time, reading of the human genome in the near future [82]. The physical interactions of the DNA and the sequencer are the same as these an ion faces in an ion channel, so the machinery developed in the field of ion channels equally applies to genome studies on the commercial basis [82].

Functionalised artificial nanopores and nanochannels In attempting to replicate how Nature works, growing interest is now being paid to the development of artificial nanopores mimicking the structure of biological ion channels [83].

This idea implies the use of simple materials, e.g. graphene [84, 85] or MoS_2 [86]. By adding functional groups on the pore rim (Fig. 1.5), selecting diameters, and selecting the substrate material, the researchers have created simplified nanopores able of conducting and selecting ions [11, 35, 36, 86, 87]. Membranes with embedded selective nanochannels may find application to water desalination [11], fuel cells [88], supercapacitors [89] and osmotic water harvesting [90].

1.5 Summary

The description, successful computation and eventually prediction of the transport properties of ion channels is the ultimate goal of our research. In this Chapter, we have discussed transport properties (conduction, selectivity, AMFE etc), and described the structure of one of the most frequently-studied channels, KcsA. We have also outlined some applications of the theory to medicine and technology. In the next Chapter, we provide quantitative methods estimating the above-mentioned properties, discuss their strengths and weaknesses and formulate the aim of the work done in the following chapters.

2. Research methods to study ion channels

> Theories of liquids do not have a small parameter.
>
> *L. D. Landau*

Recent research has provided a rich arsenal of methods to investigate the transport properties of ion channels [17, 20, 91]. These methods can be divided into experimental and theoretical approaches. It is the interplay between the two that is believed to drive the discoveries in the field.

In this Chapter we discuss most the most influential experimental and theoretical methods. In particular we shall analyse the strengths and weaknesses of each theoretical method. This will serve as justification for the goals of the thesis.

2.1 Experimental techniques

There are two main experimental approaches to understanding ion channels. The first is probing the structure through crystallography from which transport properties can be inferred or learned through simulation/theory. The second is direct measurements of ionic current or water flow which are traditionally effected by the patch clamp technique.

2.1.1 Structure studies: X-ray crystallography and cryo-EM

In order to gain information about the spatial and chemical composition of the biological structure, X-ray crystallography was historically the first method [92]. It involves preparing a sample with the protein dissolved in a suitable solvent, rapidly freezing it to 4–100°K and thus getting a solid crystal structure. Next, X-rays in the frequency band $10^{16} - 10^{18}$Hz are scattered from the electron clouds of the comprising molecules, giving rise to an exposure image. This procedure is repeated multiple times to generate enough data. These images are further analysed and the electron density maps of the compound are reconstructed. Using sophisticated techniques [92], researchers are able to further identify and label the chemical groups of the given structure. This scrupulous process results in a 3D structure of the molecule where all constituents and distances are known and can be measured up to some level of precision. Roderick MacKinnon and Peter Agre were awarded the Nobel prize in 2003 for the development of this technique.

Recently another closely related technique has been developed. Cryo-electron microscopy (cryo-EM) [93] suggests freezing the sample and exposing it to a beam of electrons, resulting in scattering patterns. Analogously, the scattering patterns are analysed, and from reverse engineering a 3D structure of the protein can be produced. The reconstructed structures are routinely published at the website RCSB Protein Data Bank [94].

One of the disadvantages of these techniques is that the structure is measured at non-physiological low temperatures [95]. As a result the structure is of a rigid pore that does not include the room temperature fluctuations [34]. Moreover, ions transiting the pore can result in structural changes [34] making flexibility and fluctuations essential for rapid conduction. Therefore, the structural information should be treated with care [15].

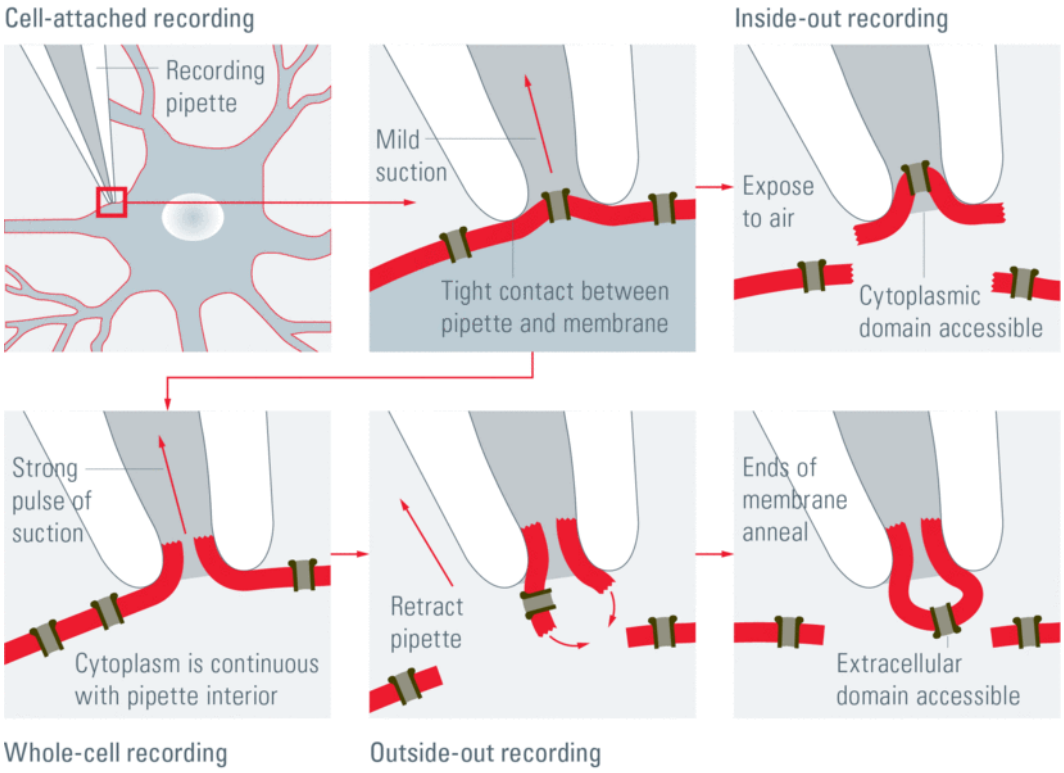

Figure 2.1: Stages of the patch clamp experimenting. From the cell-attached configuration, one can switch either to the whole-cell configuration, or initiate the single-channel recordings (inside-out or outside-out). Taken from [100, 101].

2.1.2 Patch clamp

In the patch-clamp technique [96–98], the researcher establishes an electric contact with the contents of a biological cell, which in turn allows measurement of the current or voltage across the cellular membrane. Due to its ability to study the involvement of ion channels in fundamental cellular processes, this method became the gold standard in biophysics decades ago [2, 99].

The overall workflow is shown in Fig. 2.1. Typically, one first prepares the bathing and intrapipette solutions checking the equality of their pH levels. Then the pipette is placed in contact with the surface of the cell. By applying negative pressure one establishes the high-resistance (10–100 Giga-Ohm) contact with the surface, which literally means no current flow through the gap between the glass pipette and the membrane surface. At this stage, several configurations are possible:

1. **Cell-attached patch.** In this configuration, one can measure the currents

flowing through one or several channels. The advantage here, is that there is minimal disturbance to the cell. The apparent disadvantage is the inability to alter the contents of the cell during the experiment, which may be of interest if one is investigating solely the membrane properties.

2. **Whole-cell.** With further short negative pressure pulse (suction) the membrane is ruptured such that the pipette becomes attached to the cell. During several minutes after that the cytosol is substituted by the intrapipette solution [96,102]. The latter point thus allows to study the conductive properties of the cellular membrane as the chemical composition across it is known explicitly and the transmembrane potential is set. However, in this configuration cellular organelles may be washed out through the pipette tip [96,102] what makes this configuration unsuitable for studies where the natural cellular processes are of interest.

3. **Perforated patch clamp.** If the pipette contains the appropriate antibiotic, the latter will make small holes in the membrane (Perforated patch). Thus, the penetration of the pipette solution into the cell is impeded. The washout of intracellular organelles becomes prevented as well. Thus, one can measure electric properties of a cell with little intervention in its functioning. However, there is little control over the chemical composition of the cell, therefore this configuration is rarely used in ion channel experiments.

4. **Inside-out and outside-out patch clamp.** If one tears off a patch of the membrane into the pipette, this will be an inside-out configuration (what was *inside* is now *outside*). If, additionally, the ends of the patch anneal, this is an outside-out configuration (what was *outside* stays *outside*). This allows one to extract a wealth of information about a single ion channel.

Once a particular configuration is established, one begins experiments according to a specified protocol. For instance, applying a voltage-stepping protocol one measures a set of currents through the channel at different voltages. These

recordings provide information about the selective and conductive properties of the membrane, consisting of the channels of interest.

2.2 Theoretical techniques to study nanochannels

Theoretical studies of nanoscale systems focus on different spatial and temporal scales (Fig. 2.2) of the processes of interest [103]. The main challenge, and yet source of intrigue is the fact that everything interacts with everything [15]: ions interact with other ions including ions of different species, ligands, protein and water molecules, and an applied electric field. The complex nature of these interactions ensures that understanding the consequences remains a challenge in the studies of conduction, selectivity, blocking, channel mutations, and the effects of pore fluctuations. Hence, specific methods have been developed to describe these phenomena at each particular scale, but unfortunately, there exists no single descriptive method capable of covering all the spatiotemporal scales and microscopic nuances [104]. In this section we consider existing theoretical approaches in detail paying particular attention to their strengths and weaknesses.

The overall battery of existing methods is depicted in Fig. 2.2, where the spatiotemporal constraints of each particular method are shown. The overlapping areas indicate the possibility to verify/calibrate one method on the prediction from another, or to create a hybrid approach combining the level of details of one method with the speed of another [13]. A number of reviews, discussing the strengths and weaknesses of the existing methods and their biophysical applications, have been published [17, 20, 105–107].

The most fundamental description suggests using QM, where the wave function Ψ depends on the coordinates of all nuclei and electrons of all species present, while the evolution of the system is governed by the time-dependent Schroedinger equation [108, p.305]. However, this appears extremely computationally expen-

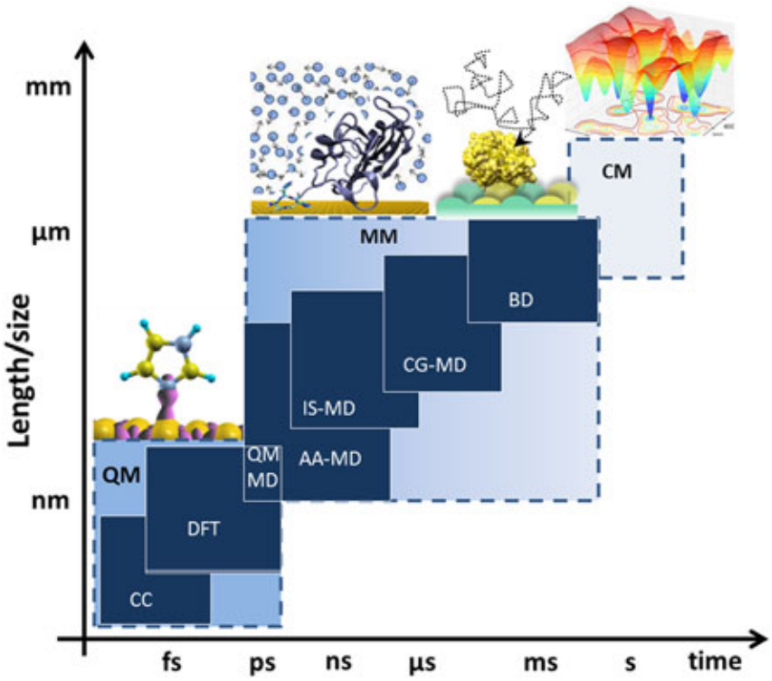

Figure 2.2: Spatial and time scales of the existing theoretical methods, as well as cross-overs between them. Depending on the description approach, the methods are divided into quantum mechanical (QM), molecular mechanical (MM) and continuous mechanics (CM). Abbreviations: coupled cluster (CC), density functional theory (DFT), quantum-mechanical molecular dynamics (QM MD, also known as QM/MM), all-atom (AA), implicit-solvent (IS), coarse-grained (CG), Brownian dynamics (BD). Taken with permission from [103].

sive. The need to include quantum effects in a simulation has led to a QM/MM approach, in which ionic interactions are computed using QM methods while the ionic motion is given by the Newton's second law [108]. The complexity of the QM-related methods makes them unusable for the ion channel studies particularly due to the lack of comparison with experimentally measured ionic currents. However, *ab initio* or DFT methods provide quantitative estimations required in the force fields in the coarser methods such as molecular dynamics [109].

2.2.1 Molecular dynamics

The elimination of the electronic degrees of freedom and consequent parameterization of the atomic interactions leads to a fully mechanistic description of the system by means of molecular dynamics (MD) [110, 111]. At this stage, typically one distinguishes between ions and water molecules. The Hamiltonian of such a

system is [111]

$$
\begin{aligned}
H = & \sum_{atoms} \frac{p_i^2}{2m_i} + \sum_{bonds} k_i^{bond}(r_i - r_0)^2 + \sum_{angles} k_i^{angles}(\theta_i - \theta_0)^2 \\
& + \sum_{dihedrals} k_i^{dihe}\Big[1 + \cos\left(n_1\phi_i + \delta_i\right)\Big] \\
& + \sum_i \sum_{j \neq i} 4\varepsilon_{ij}\left[\left(\frac{\sigma_{ij}}{r_{ij}}\right)^{12} - \left(\frac{\sigma_{ij}}{r_{ij}}\right)^{6}\right] + \sum_i \sum_{j \neq i} \frac{q_i q_j}{4\pi\epsilon_0 \epsilon r_{ij}}.
\end{aligned}
\tag{2.1}
$$

where the kinetic energy is accounted for by the first term, and the remaining terms represent the bonding (second term), rotational (third term), dihedral (fourth), short-range soft Lennard-Jones (fifth) and electrostatic Coulomb (last term) interactions. This Hamiltonian [110] yields the equations for the progressive motion of each molecule:

$$
\begin{aligned}
\mathbf{r}_m &= \frac{\partial H}{\partial \mathbf{p}_m} \\
\mathbf{p}_m &= -\frac{\partial H}{\partial \mathbf{r}_m}
\end{aligned}
\tag{2.2}
$$

Typically simulations are set up as a rectangular box with periodic boundary conditions. Thus, if a particle exits the domain through one of the edges, it immediately re-enters from the opposite side. As a result periodic boundaries limit the simulation to symmetrical solutions on both sides of the membrane [16, 95], unless specific arrangements are made [112]. The minimal image convention in Z dimension is used.

The transition from a purely quantum description to a molecular mechanics suggests two principal reductions [111]. The first one – the Born–Oppenheimer approximation – states the electrons move much faster than the nuclei, and thus they react instantaneously to the motion of their nuclei. Thus, the electrons may be considered independent. The second reduction treats the nuclei, whose mass is three orders of magnitude larger than that of the electrons, as point particles that obey the Newtonian dynamics. In classical molecular dynamics, the presence of the electrons is approximated as single potential energy surface that typically represents the ground state.

The conceptual simplicity and level of details make the MD a *de facto* standard in the nanoscale research. This method does not require the knowledge of random or frictional forces as in Brownian dynamics, and does not make any assumptions about the properties of the solvent, dielectric permittivities or boundaries [106]. In principle, MD includes all interactions (water–ions, water–protein, water–lipid, lipid–protein) and thus allows the researcher to trace the effect of the flexible protein inside the lipid bilayer on the dynamics of the ion channel [106]. Importantly, one can quantify the spatial variation of important parameters such as diffusivity, dielectric constant, potential of the mean force. These paramaters can then be embedded into a coarse-grained or BD simulation to yield experimentally verifiable selective and conductive properties.

Due to the presence of long-range pairwise interactions, the time-frame of an MD simulation grows as N^2 where N stand for the number of separate atoms in the system [110]. It relies heavily on parallel processing, super-computational resources, as well as other acceleration methods. However, the explicit description of hydrogen motion restricts the largest time step to 2.5fs [113], imposing limitations on the simulated time, space, and amount and type of ions present. These limitations cause several difficulties. First, with a few recent exceptions [12, 67], the simulations do not run for a sufficiently long time to produce statistically meaningful currents through the channel which can further be compared with experimental data [78]. For instance, in the KcsA channel under 100mV voltage and 100mM symmetrical concentrations one would expect a 7pA current that implies on average 1 permeation per 23 ns [75]. The latter requires high-end computational resources to gain enough statistics.

As computational power rapidly improves annually, there is no doubt that these issues will eventually be overcome [114]. A more profound issue is determining the force fields describing the interactions in the system. On the fundamental level these interactions are given by the laws of quantum mechanics (see previous section). However, in MD the interactions are usually assumed to be pairwise.

Furthermore, these interactions are quantified by an analytical function with a relatively small set of atom-specific parameters that are calibrated using empirical data under very specific conditions: temperature, pressure, specific molecules (e.g. proteins or lipids) [115], particular composition of solutions, etc. [110]. Thus, the application of these parameters in drastically different environments or conditions may lead to inaccurate results [54, 116]. For instance, this results in different solvation energies which will greatly affect the selectivity of the pore [16].

The force fields often lack polarization effects, thus affecting the energetics of ion-water and ion-protein interactions [117]. The polarization of the first hydration shell occurs due to the high charge density of multivalent cations (e.g. Mg^{2+} and Mg^{2+}) [54]. Non-polarizable models appear unsuitable for the treatment of covalent bonds [115], proton transport and the protonation of ionizable amino acids [16] where the dynamical redistribution of electronic charge play the key role. Polarizable models – AMBER, AMOEBA, Drude, CHARMM, CHEQ – are being developed to cover various types of biomolecule [118].

While searching for current-voltage curves, long-range electrostatics has to be considered carefully. Typically one has to introduce some sort of approximation to deal with the $1/r$ dependence of the interactions [16]. The most common choice is the Particle Mesh Ewald algorithm [119] in which point charges are substituted by Gaussian distributions with std $\sigma = 0.25\text{Å}^{-1}$.

Thus, the MD is the most detailed method, but relatively inefficient as of now. Often, non-physiologically high temperatures, pressures, concentrations and voltages are applied to get sufficient statistics of currents. This abandons the parameter ranges within which living cells function. Therefore, one would hugely benefit from a method combining the MD level of details with sufficient computational speed to estimate currents in realistic conditions. In Chapter 3 we develop such a hybrid method by plugging the MD data into a BD simulation.

Potential of the mean force (PMF)

One of the central quantities in computational studies of nanoscale systems is the potential of the mean force (PMF) [120–122]. It reflects all of the ion's interactions with its environment, involving other ions, protein, and solvent. The PMF is equivalent to the Helmholtz free energy in the NVT ensemble, i.e. the reversible thermodynamic work [91], of bringing the considered set of molecules from infinity into the required configuration [123, p.75]. An N-particle PMF $W_N(\mathbf{r}_1^\alpha, \mathbf{r}_2^\alpha, \dots)$ is [31, 91, 122, 124]

$$e^{-W_N(\mathbf{r}_1^\alpha,\dots,\mathbf{r}_N^\alpha)/k_BT} = C \int \mathrm{d}\mathbf{X}\; e^{-U_{all}(\mathbf{r}_1^\alpha,\dots,\mathbf{r}_N^\alpha,\mathbf{X})/k_BT}. \tag{2.3}$$

Here C is a constant, and $U_{all}(\mathbf{r}_1^\alpha, \dots, \mathbf{r}_N^\alpha, \mathbf{X})$ represents the potential energy due to interactions between *all* atoms, i.e. permeable ions located at $\{\mathbf{r}_1^\alpha, \dots, \mathbf{r}_N^\alpha\}$ and other atoms at $\mathbf{X} = \{\mathbf{r}_1^\beta, \mathbf{r}_2^\beta, \dots\}$. In light of Chapter 5, it is worth noting that the two-point PMF is connected to the radial density function (RDF) [123, p.75]. The PMF in the selectivity filter of the biological KcsA channel is illustrated in the right panel of Fig. 3.6.

Due to its detailed nature, the PMF includes rigorously the effects of dehydration at the entrance and inside the channel, the induced charges on the pore walls, the ion's interactions with other ions in the pore, and the influence of the flexible pore structure. However, a PMF is not an average of the microscopic potential and is non-additive [91, 122, 123]. Strictly speaking, usage of a PMF is restricted to the specific ionic concentrations and type of species in bulks input in its calculation [25]. However, the PMF reveals weak sensitivity to these parameters until concentrations become too high [122]. One can also rigorously decompose the local effects of the protein and the external electrostatic field [122]. These points allow one to use the same PMF under a wider range of parameters, see Chapter.3.

In equilibrium, the PMF can be directly obtained by means of [122]

$$W - W_{offset} = -k_B T \ln P,$$

where the probability density P is measured by sampling the system. In practice, the existence of energy barriers greater than $1k_BT$ will result in some areas being insufficiently sampled, which raises questions about the PMF convergence [125]. To avoid this problem, enhanced methods to compute a PMF exist. These include free energy perturbation [126], umbrella sampling with weighted histogram analysis [127], steered molecular dynamics simulations [128].

2.2.2 Brownian dynamics (BD)

The elimination of the water as molecules leads to Brownian dynamics (BD) [129–133] which can formally be obtained from Eq. (2.1). This simplifies the description further as all water degrees of freedom are integrated out from Eq. (2.2). However, one then has to include an explicit noise term to represent the ion-water collisions [134]

$$m^\alpha \frac{\mathrm{d}\mathbf{v}_k^\alpha}{\mathrm{d}t} = -\gamma^\alpha m^\alpha \mathbf{v}_k^\alpha + \mathbf{F_N}(\mathbf{r_k^\alpha}) + \sqrt{2m^\alpha \gamma^\alpha k_B T}\boldsymbol{\xi}(t). \tag{2.4}$$

Here m^α is the ion's mass, γ^α is its friction coefficient which is coupled to its diffusivity D^α via the Einstein relation $D^\alpha = k_BT/m^\alpha\gamma^\alpha$, $\mathbf{v}_k^\alpha$ is the ion's velocity, $\mathbf{F}_N(\mathbf{r_k^\alpha})$ represents the force acting on an ion located at $\mathbf{r}_k^\alpha$ when N ions are present in the channel, k_B is Boltzmann's constant, T represents the absolute temperature, and ξ is three-dimensional white noise of unit intensity ($\langle\xi\rangle = 0$, $\langle\xi(t+\tau)\xi(t)\rangle = \delta(\tau)$). This is known as the Langevin equation and it can be solved with an appropriate numerical method [110, 111, 134]. The elimination of the solvent's degrees of freedom allows the use of much larger time steps, for instance as large as 2ps in contrast to 2fs (three orders of magnitude) in MD. This makes BD a computationally fast method to predict and analyse ionic currents under the effect

of voltage, or concentration gradients in wild or mutated channels [125].

The Langevin equation assumes times larger than the relaxation time $\tau = 1/\gamma$ of the medium [135] at which velocity correlations vanish. Strictly speaking, the Markovian assumption – requiring the Brownian particles (ions in our case) to be much heavier than the solvent molecules – may not be applicable to ions in water [136,137] and instead suggests invoking the concept of the memory function in a generalized Langevin equation [16]. In the derivation of Eq. (2.4) one assumes constant electric field [138]. The meaning of diffusion should also be clarified when fluctuations of the channel elements are allowed in the BD simulations [117] and permeation over a fluctuating barrier is possible [139].

The 3D simulation domain typically comprises of the channel itself and, attached on either side, two reservoirs containing ions. The channel is typically considered rigid although in reality the atoms forming the channel (e.g. the carbonyl groups) demonstrate femtosecond fluctuations and thus may influence the ionic motion [16, 34, 81]. Geometric boundaries of the simulation domain can be impermeable (reflective with a reflective potential [78]), periodic (analogous to that in MD) or stochastic [140]. From the physics perspective, one can use the Grand canonical Monte-Carlo (GCMC) boundary [141] allowing the consideration of arbitrary concentrations at a relatively low computational cost. We discuss the GCMC algorithm in more detail in Chapter 3. Finally, the boundary properties can be combined to have for example impermeable walls in XY-direction and periodic in Z direction.

An individual ion is subject to three forces resulting in the total force $\mathbf{F}$ [16]. These arise due to the other ions, charges on the protein walls and the presence of the transmembrane potential. The ion-ion interactions are usually approximated via the Coulomb or screened Coulomb law [91,130]. To prevent the overlapping of oppositely-charged ions, e.g. K^+ and Cl^-, one introduces a short-range soft repulsive potential [110,129,142,143]. The ion-channel contribution implies interaction with the charges fixed on the pore's surface, and the induced surface charges arising

at the interface separating the pore from the protein. It can either be taken under some sort of an analytical approximation e.g. [144], or taken from MD [113, 145]. Finally, one has to include the electric potential profile due to the external electrostatic field. That is done by solving the Poisson equation in the reservoir and channel domains [17]. This equation assumes a constant electrostatic field without accounting for the charge density fluctuations [146, 147], inherent to the mean-field methods (see next section), and requires knowledge of the dielectric permittivity [125].

The presence of solvent molecules mediates the hydrodynamic interactions between ions [148]. Therefore, the structure-less solvent in BD simulations lacks that property [149]. Appropriate parametrization of the ion-ion interactions is possible, but it requires careful consideration when both ions are confined in the pore interleaved by aligned water molecules [150]. The latter is of primary importance in the kinetic and dynamic properties [151]. Moreover, the hydration shells surrounding an ion in the narrow pore during permeation undergo structural rearrangements, loosing water molecules and substituting them by the channel's polar groups [77, 86]. This immediately affects the profiles of the diffusivity in the pore, thus making them spatially varying [91].

As stated above, BD simulations allow for the fast calculation of currents but are based on a number of assumptions regarding the interactions in the channel: diffusivity profile, and the interactions between and with other ions and with the channel when inside it. These can be avoided by incorporating MD-generated PMFs where the aforementioned interactions are consistently included. Although a number of BD-simulators exist [113, 132, 133, 152], they do not allow to embed the PMF from MD. Therefore, we develop our system in Chapter 3.

2.2.3 Poisson-Nernst-Planck (PNP) theory

The next level of approximation is to describe the probability to find an ion at a particular point in space. Multiplying this probability by the ion's charge, one

starts dealing with the dynamics of continuous charge density. This description comprises two ingredients: the Nernst-Planck transport equation describing the spatio-temporal evolution of the density ρ,

$$\mathbf{J}_m = -D_m(\mathbf{r})\Big[\nabla c_m + \frac{z_m e c_m(\mathbf{r})}{k_B T}\nabla\phi\Big] \tag{2.5}$$

$$\nabla\mathbf{J}_m = 0 \tag{2.6}$$

Thus, the Nernst-Planck (NP) equation represents a combination of the Fick's and Ohm's laws. and the Poisson equation connecting the potential ϕ of the electric field $\mathbf{E} = -\nabla\phi$ created by the total local charge density:

$$\nabla\Big[\epsilon(\mathbf{r})\nabla\phi(\mathbf{r})\Big] = -e\left[\rho_{fixed} + \sum_m^N z_m c_m(\mathbf{r})\right] \tag{2.7}$$

In the above equations, $\mathbf{J}_m$ is the ionic current, D_m is diffusivity, c_m is concentration, z_m is ion's valence, T is temperature, ϕ is the electrostatic potential, and ρ_{fixed} is the density of fixed charges. The NP and Poisson equations are supposed to be solved simultaneously.

In the PNP theory ions are treated not as discrete entities but as continuous charge densities that represent the space-time average of the microscopic motion of the ions. It is perhaps the simplest nonequilibrium theory accounting for the channel's form, the spatial distribution of charged residues inside the channel protein, the external electrostatic field and the asymmetrical concentrations of ions on both sides of the membrane [16]. An extensive list of the literature on this model of charge transport theory is provided in Ref. [107].

The rigorous derivation of the PNP theory starts from the Langevin equation(2.4) [153]. One then arrives at the hierarchy of PNP-like equations with conditional and unconditional number densities [154] closely related to the Bogolyubov-Born-Green-Kirkwood-Yvon (BBGKY) chain [155]. This hierarchy remains infinite until a closing relation is applied to decouple it [153]. Replacing a two-particle correlation function by a product of two single-particle functions, one arrives at

the mean-field approximation [156]. The consequences of this step require deeper discussion.

First, the mean-field nature of the PNP method suggests an absence of ion-ion correlations. This can only be valid beyond the correlation length of the medium [157, 158]. By omitting these correlations one finds that the concerted ionic motion that is present [16, 17, 54, 159, 160] in multi-ion ion channels is out of scope. In addition, saturation of the current [161, 162] and Ionic Coulomb Blockade [163], are not describable. The lack of structure of the solvent (water) also imposes restrictions on the description of single-file permeation where ions with water molecules permeate collectively in highly-correlated manner [26, 117, 150].

Secondly, PNP lacks the effect on the ion from the dielectric boundary on the pore, and thus the dielectric self-energy (also known as the reaction field) is largely underestimated [164]. For instance, saturation of conductance cannot be described if the self-energy is not involved [16]. The concept of a local dielectric constant describing the electric response of a fluctuating macromolecule faces principal difficulties which limits the theory [91]. Also, PNP is weakly sensitive to the dielectric constants [159] which enter as quantities to experiment or MD simulations [59, 159]. They reveal larger variations from their bulk values in some cases ranging within an order of magnitude [159] for instance between K^+ and Cl^- to suppress the anion current [59]. This suppression is also possible by unrealistically reducing the diffusivity [162] to fit the data. It has been shown that the PNP theory agrees well with BD simulation results only when the pore radius exceeds two Debye lengths [106, 159, 162, 165]

It is also worth mentioning that linear continuum electrostatics in the weak-field limit i.e. when the polarization and electric fields are parallel, does not hold in hydration layers [158]. The averaged nature of the theory also does not allow the fluctuations of the electric field [146, 147] and current [161] that are observed experimentally. The presence of atomic fluctuations also poses the question of where the boundary between the charge and the protein/fluid water is located [158].

Recently, the basic PNP model has been generalised to incorporate a number of crucial interactions under the name EnVarA – Energy Variational Analysis [166], while a number of other papers have emerged to fix particular issues in PNP theory. These include steric effects [167], Fermi PNP [168,169], conditional PNP [153], PNP-DFT [170], PMF-PNP [131], Soft-wall PNP (SIP-PNP) [171], or a combination of the NP equation with Local equilibrium Monte Carlo simulations [132].

Poisson-Boltzmann theory

In equilibrium when the local fluxes (2.5) vanish everywhere [172], one expects that the densities of charged ionic species satisfy

$$C_m = C_m^{\infty} e^{-\beta\phi(r)} \tag{2.8}$$

Plugging it into the Poisson equation (2.7), one obtains the Poisson-Boltzmann equation

$$\nabla^2\phi = \sum_{j=1}^{N} \frac{N_A C_j e_0^2 z_j^2}{\epsilon\epsilon_0 k_B T} e^{-\beta z_m q_m \phi} \tag{2.9}$$

This is a nonlinear equation and it coincides with the PNP under stationary conditions [164]. Its solution yields the spatial distribution of the electric potential and consequently, the distribution of each ionic species. Attempts to solve equation utilize Delphi [173] or APBS [174] solvers.

Stemming from the mean-field PNP theory, the basic PB approach inherits its strengths and weaknesses. These include the lack of the dielectric self-energy [16] especially in a many-body system where one has to compute the effect of the reaction field, caused by one ion, on other ions [16]. Correlations and non-electrostatic interactions (e.g. ionic size) are also missed [175]. Despite these limitations, the PB equation is invoked in the calculations of transmembrane potential [141], protonation states pK_a protein residues, and in the estimations of protein-ligand binding energies [17].

2.2.4 Statistical theory

Another level of description implies operating with the states in which channel can exist. For instance, there may be two ions interleaved by water molecules. Describing the interactions in that system, and deriving the probabilities of each states one gains a powerful tool to quantify the behaviour of the nanoscale systems.

One first has to introduce the state space of the channel. The channel is considered to possess an integer number of states j, each of them having n_j ions. The energy of each individual state of the channel is given by [41]

$$\begin{aligned} E(\{n_j\}, n_f) =& E_0 + (n_w^L - n_w')\mu_w^L + (n_w^R - n_w'') \\ &+ \sum_{i=1}^{m}(n_i^L - n_i')\mu_i^L + \sum_{i=1}^{m}(n_i^R - n_i'')\mu_i^R \\ &+ n_w\mu_w^C \\ &+ \sum_{i=1}^{m} n_i(\bar{\mu}_i^C + q\phi^C) + kT\ln n_w! \prod_{i=1}^{m} n_i! + \epsilon(\{n_j\}, n_f). \end{aligned} \tag{2.10}$$

Here E_0 is the ground state energy, n_w^L and n_w^R are the numbers of molecules in the left and right bulks, respectively, n_w' and n_w'' are the numbers of water molecules that entered from the left and right bulk, μ_w^L and μ_w^R are the chemical potentials of water in the bulks, μ_w^C is the chemical potential of water molecules in the channel, and n_w is the total number of water molecules in the system. Similarly, n_i is the total number of ions in the system, n_i^L and n_i^R represent the number of ions in the right bulk, n_i' and n_i'' are the numbers of ions that entered from the left and right bulks, μ_i^L and μ_i^R are the ionic chemical potentials in both bulks, $\bar{\mu}^C$ is the ionic excess chemical potential in the channel, q is the ionic charge, ϕ^C is the electrostatic field in the channel, and the term $\epsilon(\{n_j\}, n_f)$ represents the electrostatic interaction between the ion and the channel's fixed charge.

From here, one defines the probability in the Grand canonical ensemble of the

selectivity filter [41]

$$P(\{n_j\}, n_f) = \frac{1}{\mathcal{Z}} \prod_{i=1}^{m} \frac{(x_i^s)^{n_i}}{n_i!} e^{\beta(\sum_i n_i \Delta\bar{\mu}_i^S - \epsilon(\{n_j\}, n_f))} \tag{2.11}$$

where $\Delta\bar{\mu}^S = \mu_i^S - \mu_i^{bulk}$ represents the difference between the excess chemical potential in the s-th site and in the bulk for ionic species i, x_i^s is the mole fraction, and K is the maximal occupancy of the channel. The partition function $\mathcal{Z}$ is given by

$$\mathcal{Z} = \sum_{\{n_j\}, \sum n_j \leq K} \prod_{i=1}^{m} \frac{(x_i^s)^{n_i}}{n_i!} e^{\beta(\sum_i n_i \Delta\bar{\mu}_i^S - \epsilon(\{n_j\}, n_F))} \tag{2.12}$$

The current can be obtained by means of linear response theory [41, 176]

$$\sigma_m = q^2 D_m \frac{\partial c_m}{\partial \eta_m} \tag{2.13}$$

as a variance of the channel's occupancy. In the above formula D_m stands for the diffusivity. The theory outlined allows one to account for the distinguishable and indistinguishable binding sites [176], explain the ionic Coulomb blockade (ICB) phenomenon [163, 177], cover the presence of multiple species in solutions [42], and explains the Eisenmann selectivity sequence [32, 176].

The statistical theory is conceptually elegant and analytically tractable. One should, however, bear in mind the simplifications it contains, as consistent description of all the interactions present is the principal requirement for success of the theory. First of all, the introduction of the integer state space requires one to replace the long-range ion-ion interactions by site-site interactions in the mean-field regime [117]. As Coulomb's law is no longer applicable, this requires a mean-field approximation.

Secondly, the interaction between an ion and the channel has to be described. This includes the effect of the pore dielectric charge and the fixed charge, representing the charge of amino acid residues. One often borrows these ion-channel interactions from the PNP model suggesting continuum homogeneous electrostat-

ics (see section 2.2.3). Thus, the issues of the continuum description become inherited.

Thirdly, the electrostatic field due to the externally applied voltage is described under the cylindrical geometry approximation where the field is approximated as one-dimensional [178, 179], instead of being computed [180]. The attenuation of the transmembrane voltage due to the entrance effects, e.g. an electric double layer, is often modelled by means of the Debye-Hückel approximation [176].

2.2.5 Kinetic (rate) theory

Similar to the statistical theory, in the rate model one studies the dynamics of each system's state. In the linear approximation, this dynamics is given by the kinetic equations

$$\dot{P}_m = \sum_n \Gamma_{nm} P_n. \tag{2.14}$$

For a 2 state system, this reads as

$$\begin{pmatrix} \dot{P}_1 \\ \dot{P}_2 \end{pmatrix} = \begin{pmatrix} \Gamma_{11} & \Gamma_{12} \\ \Gamma_{21} & \Gamma_{22} \end{pmatrix} \begin{pmatrix} P_1 \\ P_2 \end{pmatrix} \tag{2.15}$$

The ionic current is thus given by

$$I = q(\Gamma_{mn} P_m - \Gamma_{nm} P_n) \tag{2.16}$$

where q stands for the ionic charge.

The rates are obviously the main ingredient of this method. One can use the mean first passage time (MFPT) [181] or the Kramer's limits [182] to estimate the rates numerically. A more rigorous approach is to compute the rates by means of the statistical theory [41, 176]. Often these are fitted data without a direct coupling to the structural properties of the pore. In this type of modelling, the introduction of the consistent transition rates Γ_{nm}, directly related to the channel structure and experimental conditions, is the main challenge [16, 176].

The rates are often related to the binding affinities according to the energy landscape but not to the structure of the pore [183]. Multi-ion effects are hard to handle [183]. This hinders the connection to the channel's structure [147].

Importantly, the rates have to reflect the experimental conditions: concentrations, chemical composition (e.g. having K^+, Na^+ and Cl^- ions), externally applied voltage, and Debye-Hukkel shielding [146] although these quantities are known to affect the energy landscape [46]. The kinetic theory has also been argued as being unable to satisfy the conservation of electric current [147, 184, 185].

2.3 Summary

Studies of biological ion channels require a thorough investigation of atomic details resulting in the channel's conduction, selectivity, blocking, channel mutations, and the effects of pore fluctuations. In this chapter, we have reviewed the commonest methods used to study the ionic transport through biological and artificial nanochannels. These include molecular dynamics (MD), Brownian dynamics (BD), Poisson-Nernst-Planck (PNP), statistical and kinetic theories. All of these methods have their corresponding strengths and weaknesses. MD allows consideration of the atomistic details of the system, but the force fields and the heavy consumption of computational power prevent them from being the basic method currently. Through classical BD simulations one gets the opportunity to estimate ionic currents, but the atomistic details and the lack of wetting in narrow pores have to be sacrificed. The continuum description provided by PNP yields the currents but lack the ion-ion correlations. Using the machinery of the statistical and linear response theories, one can estimate the currents but the price to pay is further simplification of interactions. Finally, the kinetic theory suffers from the lack of self-consistent transition rates. Overall, all physical interactions cannot be described simultaneously and, depending on the requirements of the given problem, one has to compromise between accuracy of description and the desired experimentally verifiable results.

Our main aim is to describe the permeation of ions in narrow ion channels. This motion is known to be strongly correlated due to the ion-ion interactions. The latter fact does not allow us to use the PNP theory as the interion interaction has to be carefully accounted for.

In order to overcome these issues we shall introduce the concept of a quasiparticle (QP) (see Chapter 4). The QP allows us to describe this correlated motion efficiently. However, one needs to reformulate the ionic motion in terms of the motion of the quasiparticle. This is done in Chapter 4. The concept of a quasiparticle is expected to become an important ingredient in providing consistent parameters for the statistical and rate theories. This unique connection between methods implies establishing consistent relationships between theoretical approaches, as well as begin expected to be helpful in analysing and predicting experimental data. The QP is also believed to improve the statistical and kinetic theories by reflecting the MD structure and generating transition rates consistently.

In order to test our predictions regarding the quasiparticles, we need a simulation system on which to verify our results. Ultimately, one should be able to estimate ionic currents, which still preserving the atomistic accuracy. In that direction, the hybrid between MD and BD has proven useful. Namely, this approach allows one to avoid multiple physical assumptions to describe the in-channel interactions. The tandem between MD and BD has been successfully applied to KcsA [60, 78, 79, 124, 186, 187] and DNA sequencing [113]. With the purpose of gaining atomistic accuracy, we describe a BD system allowing for the incorporation of MD-generated PMFs in the next chapter.

Finally, one more problem residing in the description of the quasiparticles is the PMF. Although it can be estimated in the MD simulations, it would be hugely beneficial to estimate it analytically to get quick estimates of the ionic currents. This requires decomposing the PMF into a number of terms, specifically characterising the ion-water interaction. We have identified a novel simple way to do so by making use of the RDF. For qualitative validation of our estimations, we

consider a nano-sized orifice in a graphene monolayer which turns out to be the simplest analogue of an ion channel pore. The results of this work are presented in Chapter 5.

3. Brownian dynamics simulations

> "...if we were to name the most powerful assumption of all, which leads one on and on in an attempt to understand life, it is that all things are made of atoms, and that everything that living things do can be understood in terms of the jigglings and wigglings of atoms."
>
> *R. P. Feynman*, "The Feynman Lectures on Physics", 1963 [188]

The main target of theoretical investigations into ion channels is the calculation of the ionic current through an open channel. It is a straightforward observable that can be compared directly with available experimental data, and can be further interpreted in terms of the channel's selective properties [21]. As long as molecular dynamics (MD) does not currently provide this, one needs a combination of Brownian dynamics (BD) with MD-generated potentials of the mean force (PMFs). This hybrid allows to account for ion-ion, ion-water, ion-ligands, and ion-pore interactions, and therefore has proven useful in a number of computational studies [60, 78, 79, 113, 145, 186, 187]. However, the common BD solvers (BROWNIES [132], BROMOCEA [133], BRODEA [152], BD in GROMACS [189],

ARBD [190] do not currently allow the user to embed the MD-generated PMFs into a BD simulation. Thus, a separate program had to be created, and is the focus of this chapter.

3.1 Workflow outline

A BD simulation involves the solution of the Langevin equation

$$m^{\alpha}\frac{\mathrm{d}\mathbf{v}_n^{\alpha}}{\mathrm{d}t} = -\gamma^{\alpha}m^{\alpha}\mathbf{v}_n^{\alpha} + \mathbf{F_N}(\mathbf{r_n^{\alpha}}) + \sqrt{2m^{\alpha}\gamma^{\alpha}k_BT}\xi(t) \tag{3.1}$$

in the domain shown in Fig. 3.1 for each individual particle (ion) in the system at

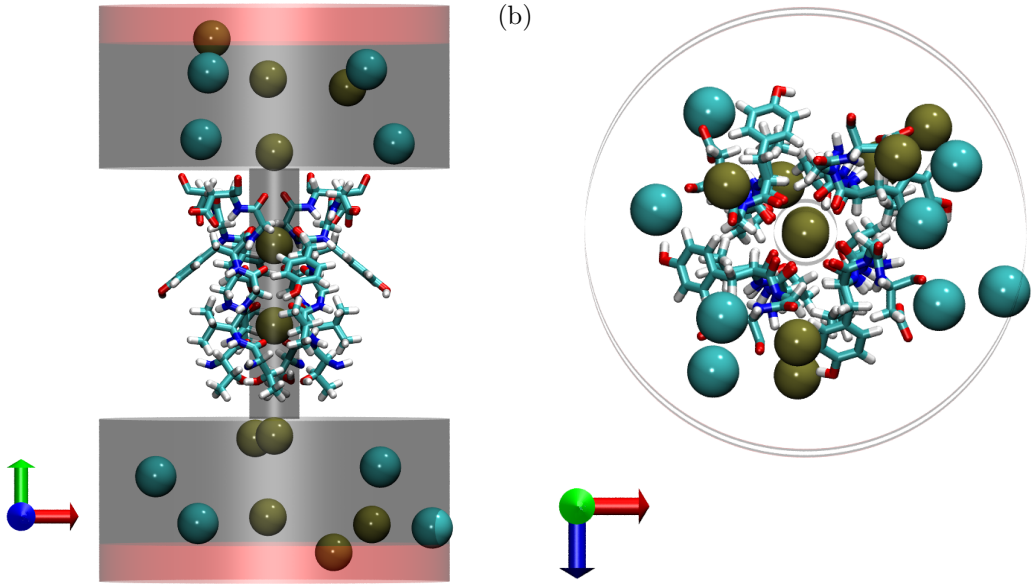

Figure 3.1: BD domain. Channel structure is shown in the licorice representation, long narrow cylinder is the pore, and the large black cylinders are reservoirs with attached GCMC buffers (red cylinders). Cyan and golden spheres illustrate the Cl^- and K^+ ions, respectively. (a) Side view. (b) Axial view. Coordinate X-, Y-, and Z-axes are represented by the red, green and blue arrows, respectively. Images were rendered in VMD [58].

any point in time. Here α is an ionic species (α =K^+, Na^+, Cl^- etc.), $\mathbf{r}_n^{\alpha}$ is the 3D radius-vector of the m^{th} ion of species α, m^{α} stands for the ionic mass (provided in Table 3.1), $\mathbf{v}_n^{\alpha}$ is its velocity, the force $\mathbf{F}(\mathbf{r_n^{\alpha}}) = -\frac{\partial W}{\partial \mathbf{r_n^{\alpha}}}$ is obtained from the multi-ion potential W_N, γ^{α} represents the friction coefficient of the species α, T is temperature, and ξ represents uncorrelated white noise ($\langle\xi\rangle = 0$, $\langle\xi(t-\tau)\xi(t)\rangle =$

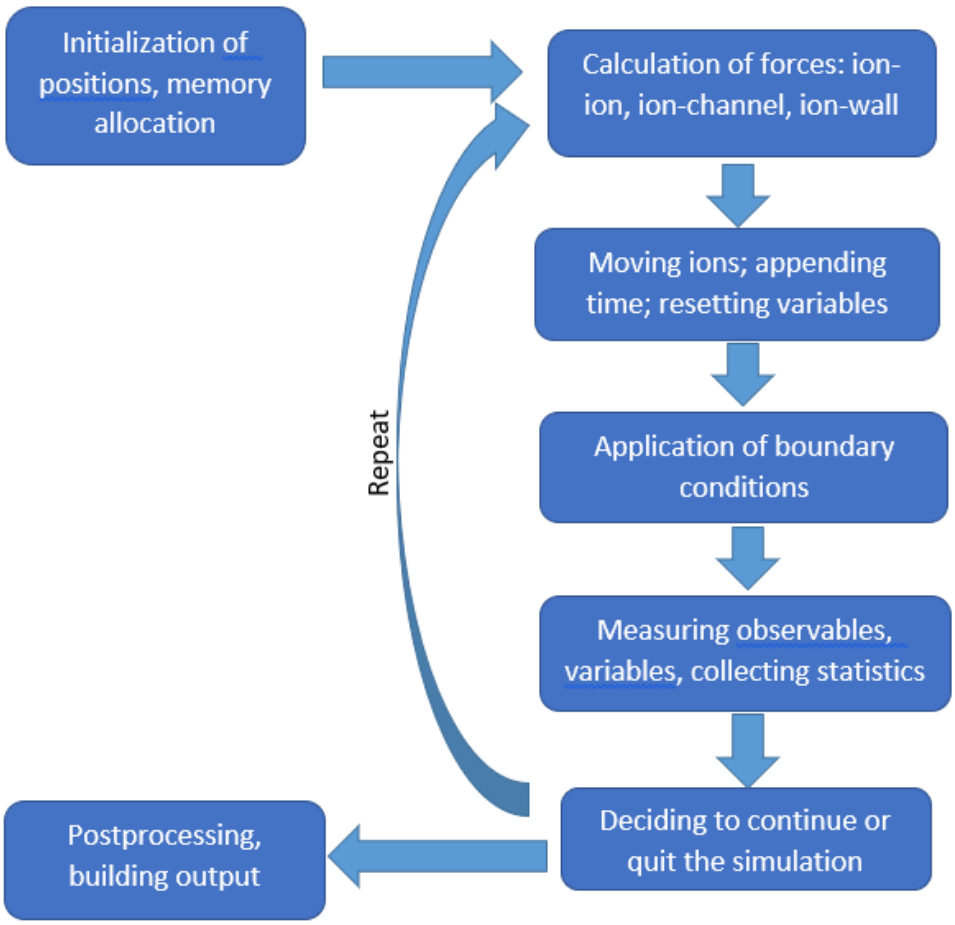

Figure 3.2: Overall workflow of a BD simulation. After setting the required model parameters and allocating variables, one proceeds with the main cycle. The later comprises the calculation of forces, updating coordinates of ions, implementing the effect of particular boundary conditions, and computing observables. When the simulation reaches the prescribed simulation time, the cycle is quit, and the collected observables are transformed into a set of output figures showing the results.

$\delta(\tau)$). The noises acting on different ions are usually assumed to be uncorrelated.

Overall, the workflow of a BD simulation is given in Fig. 3.2. One starts from initialization, where the physical constants, system parameters (domain size, temperature, number and type of chemical species...), interactions, and initial coordinates of the ions are introduced. Next, one calculates the forces acting on each ion, computes the position of each ion at the following time instant, and updates the coordinates. The latter cycle is repeated until the predefined simulation duration is reached. The main output of the BD simulation is the evolution of the ions' coordinates in time which are further used to extract the observable of interest, or

the statistics of a variable.

Ion type	Na^+	K^+	Ca^{2+}	Cl^-
Mass [$\times 10^{-26}$ kg]	3.8	6.5	6.6	5.9
Diffusivity [$\times 10^{-9}$ m^2/s]	1.33	1.96	0.79	2.03
Radius [Å]	0.95	1.33	0.99	1.81

Table 3.1: Characteristics of ions: masses, diffusivities, radii [159, 191, 192].

All coordinates are stored in a $N \times 3$ preallocated double precision array where N is twice the total number of particles in the system. This technique avoids the need to change dynamically the size of coordinate array and thus speeds up the execution of the code. Our code was written in MATLAB and utilises vectorised operations.

BD domain. The BD domain comprises the channel region, represented by a narrow cylinder of radius $R_c = 3$Å in Fig. 3.1. The channel connects two reservoirs (large cylinders of radius $R_s = 20$Å) of ions. Each reservoir is appended with a narrower 4Å buffer, if the GCMC routine is used.

At the start of a simulation, both bulks are filled with ions and the channel is empty. Their numbers in each bulk satisfy the condition of electroneutrality, i.e. if the KCl salt is selected, the amounts of K^+ and Cl^- ions are the same. Initial location of ions suggests a homogeneous spatial distribution of ions.

3.2 Numerical integration scheme

The first step in successfully implementing BD is the discretization of the Langevin equation (3.1), which is continuous in time. Generally, the discretization schemes differ by the way they estimate noise and the forces acting on ions. The simplest update rule would be to use the forward Euler algorithm [193]

$$\mathbf{x}_n^\alpha(t + \Delta t) = \mathbf{x}_n^\alpha(t) + \mathbf{v}_n^\alpha(t)\Delta t \tag{3.2}$$

$$\mathbf{v}_n^\alpha(t + \Delta t) = \mathbf{v}_n^\alpha(t) - \gamma^\alpha \mathbf{v}_n^\alpha \Delta t + \frac{\mathbf{F_N}(t)}{m^\alpha}\Delta t + \sqrt{\frac{2k_B T \gamma^\alpha \Delta t}{m^\alpha}}\zeta_1 \tag{3.3}$$

where Δt is the time step, and ζ_1 is a vector of random Gaussian number of unit variance. In the overdamped limit, when the inertial term is neglected and there is no average acceleration, the above algorithm simplifies to

$$\mathbf{x}_n^\alpha(t+\Delta t) = \mathbf{x}_n^\alpha(t) + \frac{D^\alpha}{k_B T}\mathbf{F_N}(t)\Delta t + \sqrt{2D^\alpha \Delta t}\ \zeta_2 \tag{3.4}$$

where the Einstein relation $D^\alpha = k_B T/(m^\alpha \gamma^\alpha)$ has been used, and ζ_2 is another random Gaussian number of unit variance.

The forward Euler method, although being the simplest, leads to divergences in finite time [194]. This usually happens when evaluating forces. One would choose an implicit scheme but these turn out not to be effective due to the damping effects, stochastic nature of the processes, and costly nonlinear minimization at each time step [20]. Therefore, multiple evaluation of the ion-ion forces using a predictor-corrector approach must be used. It should also be noted that the full Langevin equation with inertial terms must be used when the free-energy landscape is expected to rapidly change on the scale of the ion's mean-free path [117].

In this work, we use the implementation of van Gunsteren and Berendsen [134] (see Appendix C for full description). This algorithm suggests accuracy Δt^2 in the deterministic part and $\Delta t^{1/2}$ in the stochastic part, so the algorithm is not fully second-order [195]. We have also checked that this algorithm does not reveal drift of the system's energy in time (Fig. 3.3).

This algorithm also allows the random force to vary during a time step [136]. It supposes third-order local (second-order global) accuracy and is weakly sensitive to the time step [132] as there is no restriction $\Delta t \ll 1/\gamma$ [134,196]. These features allow us to consider the ionic motion in the bulk solution where the stochastic forces prevail, and inside the channel's mouth and pore itself where strong electrostatic and short-range forces dominate [132]. The method requires one estimation of force per time step and simplifies to a simple formula in the large friction limit [134,195]. This algorithm is unable to represent correctly the mean-square displacements at small times but provides a good estimation of static properties [195].

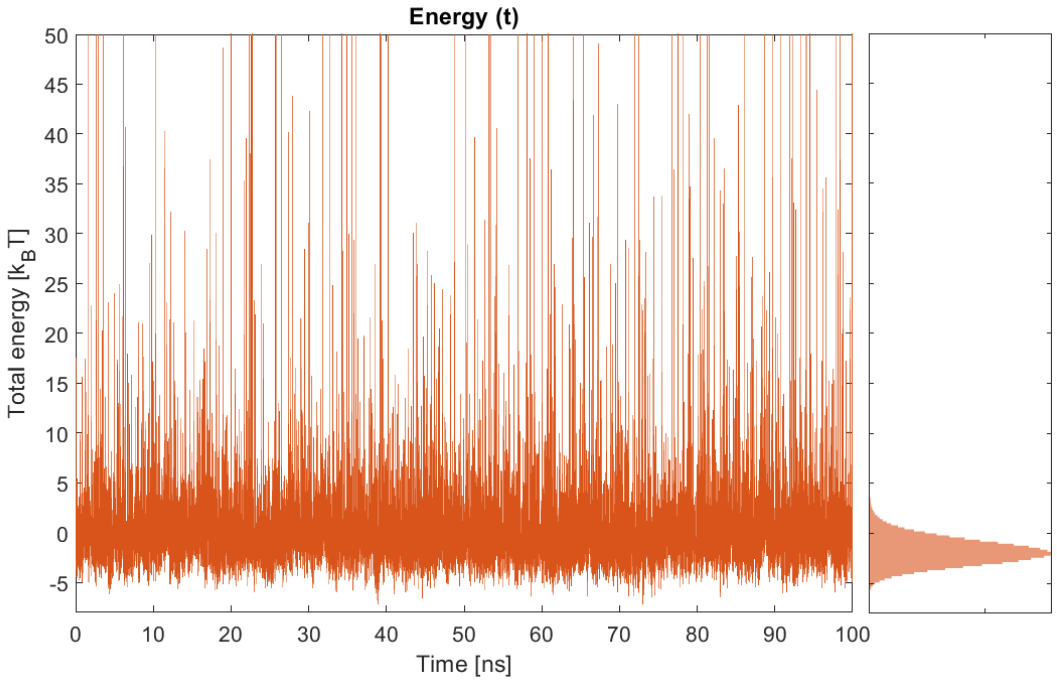

Figure 3.3: Potential energy (3.5) of the BD system in a simulation with a constant number of ions (NVT) demonstrates lack of drift in time. Large deviations occur when ions approach each other too closely.

Random number generator seed Both the Langevin (3.1) and Grand canonical Monte-Carlo (GCMC) boundary conditions described below rely on the generation of random numbers. One should ensure that the sequences of random numbers are generated For instance, one should use `rng('shuffle')` in MATLAB to have independent random sequences in simulations. Otherwise the results in two sessions with identical settings will be identical.

3.3 Calculation of forces

The calculation of all physical forces acting on individual ions is the main ingredient of the Brownian simulation [20]. The force governs the ions' motion and dynamics, which in turn define the observables. Historically, separate ion-ion and ion-channel interactions were combined to yield a compound potential landscape. However, in recent decades the vast improvements in computational resources have enabled static and even time varying multi-ion potential landscapes (PMFs) to be

computed. Below we consider both approaches.

3.3.1 Using a compound potential

In BD simulations the potential landscapes in channels are not known and need to be approximated [106]. Even now they are subjects of multi-voiced debates as to their accuracy and reliability, see Chapter 2 for more detail. The compound potential [78, 106, 197]

$$W_{compound} = \sum_k U^{i-c}(\mathbf{r_n}) + \sum_n q_n \phi(\mathbf{r_n}) + \sum_n \sum_{m>n} u^{i-i}(|\mathbf{r_n} - \mathbf{r_m}|) + \sum_n U^{wall}(\mathbf{r_n}) \tag{3.5}$$

approximates the potential energy W by encompassing the ion-ion u^{i-i}, ion-channel U^{i-c} and ion-wall U^{wall} interactions, the electrostatic field $\phi(\mathbf{r})$ due to the externally applied voltage, and the charges q_n of the ions of all ionic species present.

Specifying analytical expressions for the ion-ion and ion-channel interactions, one can hugely simplify the description of the model and therefore gain a more intuitive understanding of transport within the channel. In this subsection, we describe this approach and assume that the ionic potential can be partitioned into ion-ion and ion channel interactions.

Ion-ion interaction

The simplest choice of ion-ion interaction is a screened 3D Coulomb law

$$u^{i-i}(r) = \frac{1}{4\pi\epsilon\epsilon_0} \frac{c_i c_j e^{-r/\lambda_D}}{r}, \tag{3.6}$$

i.e. a strictly pairwise potential (cf. [136]). Here the ionic charges c_i and c_j are separated by distance r, while the medium is characterised by the dielectric permittivity ϵ. Screening constant λ_D here emerges due to the Debye-Huckel shielding of electric charge by the cloud of counterions. Molecular dynamics simulations demonstrate that the above potential reveals more a complex form [110, 158]. Namely, due to the presence of an integer number of water molecules between

ions, the repulsive potential gains damped oscillations [20, 81, 133, 198]. In this work, we did not include this effect as the ion-ion interactions in the bulk are not expected to affect the ionic dynamics inside the channel [17].

However, this potential on its own encounters a problem when oppositely charged ions attract each other to such an extent that they eventually overlap. This does not happen between real ions due to the overlap of the electronic clouds. To reflect this in a BD simulation, a short-range repulsive soft potential should be added [78, 165, 199] to Eq. (3.6), the simplest choice being [78, 191, 200, 201]

$$u_{rep}^{i-i} = \frac{F_0}{9}\frac{r_0^{10}}{r^9}. \tag{3.7}$$

The presence of co- and counter-ions in electrolytes lead to an important phenomenon – electrostatic screening. In a bulk solution, the ions are expected to be surrounded by a sphere of counterions (Debye sphere) effectively screening the charge, such that the resulting potential is given by the Debye-Hückel theory.In a 100mM biionic solution a charge is almost completely screened at the length $\lambda_D \approx 30$Å [16]. When restricted inside a pore, ions do not have enough counterions surrounding them [159] and the form of the interaction changes given the ionic size and the presence of individual waters in the pore [202]. It is the confined environment that gives rise to the correlated ionic motion and provides the rich complexity of phenomena in transport through nanopores [146].

The presence of pairwise interactions leads to the quadratically growing complexity of the simulation with the number of entities. Our MATLAB code is vectorised and it utilizes 3D matrices to calculate the pairwise differences between ionic 3D coordinates. It allows one to use only one CPU core, or to use several parallel sessions on a multi-core CPU.

Ion-channel interaction

The ion-channel interaction arises from two sources: the electrostatic interaction with charged residues and dipoles in the protein wall, and a repulsion from the

induced polarization charges on the pore-protein boundary [16, 54, 203]. The first is responsible for the formation of the binding sites suggesting that, for instance, Ca^{2+} ions bind to the high-field oxygen ligands [87,204]. Confined freedom of water molecules also strongly affects the interaction between ion and narrow pore [202]. Moreover, the back action of ions on the structure of some K^+ channels, e.g. KcsA, is essential to maintain their conductive conformation [23]. The second interaction leads to one-dimensional ionic motion [20]. It imposes energetic restrictions on ionic motion and is therefore noticeably reflected in the ionic permeation in narrow pores [131, 159, 164].

Here, we used the cation-channel potential from Ref. [144] applied along the pore's Z-axis

$$U^{i-c}(z) = -U_0 e^{-\left(\frac{z}{s}\right)^2},\ U_0 = 10.5 k_B T,\ s = 9\mathring{A}. \tag{3.8}$$

This potential, shown in Fig. 3.8, was obtained by fitting to the overall energy landscape in the KcsA channel. To prevent anions entering the channel, one should sum the repulsive Coulomb term with screening and the dehydration barrier

$$\begin{aligned} U_{Cl}^{i-c}(r) = &- \frac{1}{4\pi\epsilon\epsilon_0}\frac{e_0 Q_f e^{-r/\lambda_D}}{r} \\ &- \frac{a_U}{2}\left(\tanh\left(\frac{z-R}{b_{Cl}}\right) + \tanh\left(\frac{-z+L}{b_{Cl}}\right)\right). \end{aligned} \tag{3.9}$$

Here e_0 is a positive unit electric charge, Q_f represents the negative fixed charge (e.g. $Q_f = -1e_0$) embedded into the protein, $a_U = 25 k_B T$ is the dielectric barrier, z is the axial coordinate, R and L are respectively the locations of the right and left edges of the channel, and $b_{Cl} = 0.5$Å is the parameter controlling the steepness of the potential barrier. Also, to induce the one-dimensional motion of ions in the pore, a harmonic restraining potential

$$U^{wall}(r) = k_{harm} r^2,\ k_{harm} = 10 k_B T/(1\mathring{A})^2 \tag{3.10}$$

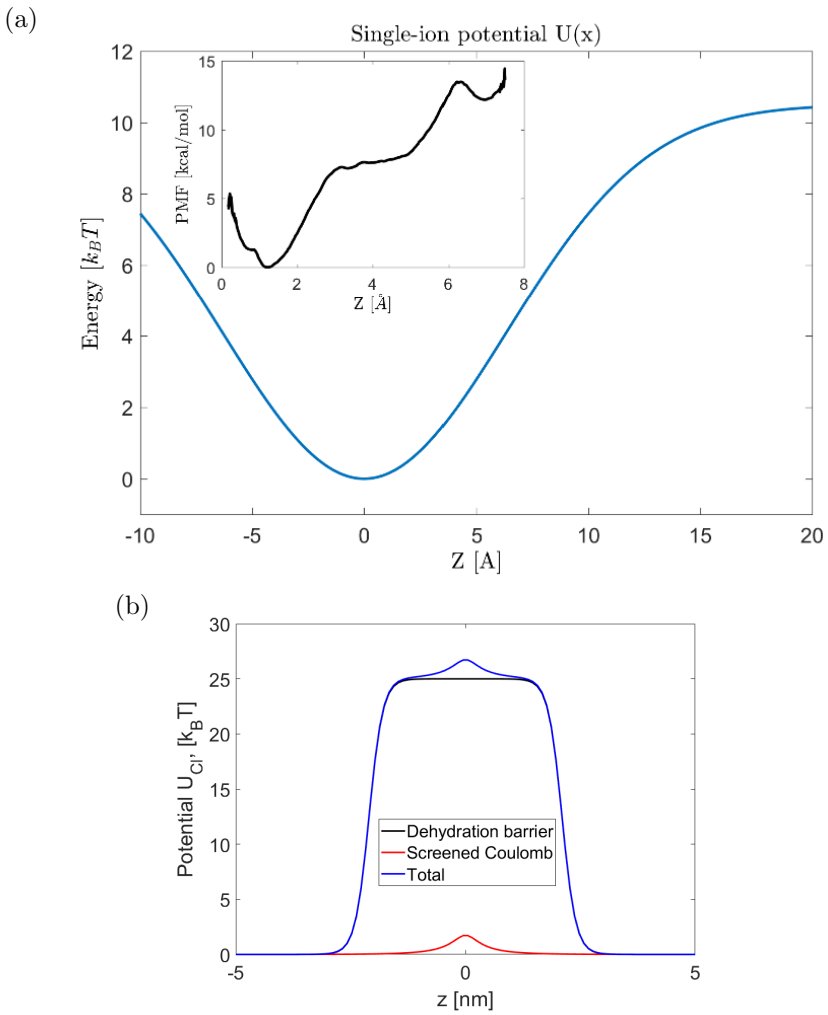

Figure 3.4: (a) Single-ion ion-channel potential [144] mimicking the single-ion PMF in the biological ion channel. Inset: single-ion PMF in KcsA (data adapted from Ref. [205] by permission from Springer Nature Customer Service Centre GmbH). (b) Compound single-ion potential barrier (blue) for Cl^- ions, consisting of the dielectric barrier (black) and electrostatic repulsion from the fixed charge (red).

was applied in the radial direction. This potential also mimics the effect of protein-pore wall. The same potential was used to mimic soft reflecting domain boundaries. Its effect was restricted to 5Å towards the inner volume of the simulation domain.

Stitching channel to reservoirs A typical case implies that the pairwise interaction between ions is characterised by a common parameter (for instance, dielectric permittivity) X_1 in the bulk and X_2 the channel. In this case one needs to specify how two ions – one in the bulk and one in the channel – interact. To do that, we first introduce a switching function that equals 0 in the bulk and 1 in

the channel. We choose a piecewise implementation

$$f(z) = \begin{cases} 0, \ z < -L_{tr}, \\ z, \ z \in [-L_{tr}, L_{tr}]. \\ 1, \ z > L_{tr}, \end{cases} \tag{3.11}$$

with $L_{tr} = 1$Å standing for the length of the transition zone within which the switch of the parameter occurs. L_{tr} should not exceed few angström so that stitching occurs at the range of one atom size and thus large spatial artefacts cannot develop. Other choices of the transition function $f(z)$ are also possible, e.g. using the `tanh` function. Thus, each ion is labelled according to its Z coordinate. The common parameter for the pair of ions then can be given by a convex combination

$$\begin{aligned} X^* =& \frac{1}{2}\Big[\Big(X_1(1 - f(z_1)) + X_2 f(z_1)\Big) + \Big(X_1(1 - f(z_2)) + X_2 f(z_2)\Big)\Big] \\ =& X_1 + \Big(X_2 - X_1\Big)\frac{f(z_1) + f(z_2)}{2} \end{aligned} \tag{3.12}$$

For instance, the ions in the same domain, e.g. in the same bulk, share the same parameters everywhere in the bulk. The same applies when both ions are in the channel. If the ions reside in different domains, the average value $(X_1 + X_2)/2$ is common. This interpolating approach satisfies the 3$^{\text{rd}}$ Newton's law. Fig. 3.5 demonstrates how the screening constant λ is chosen between $\lambda_{Debye} = 0.425nm$ and $\lambda_{in\ channel} = 0.28nm$, depending on the location of the two ions. The particular values of these parameters a chosen to describe the Debye screening in the bulk and to lead to the barrier-less conduction in the toy model of the KcsA ion channel [144].

3.3.2 Incorporating a multi-ion PMF

The use of the multi-ion PMF W_N is the best estimation of the system's energy W, as it already encompasses the ion-ion, ion-channel and ion-water interactions in the channel. Thus there is no need to speculate on how to approximate these. In

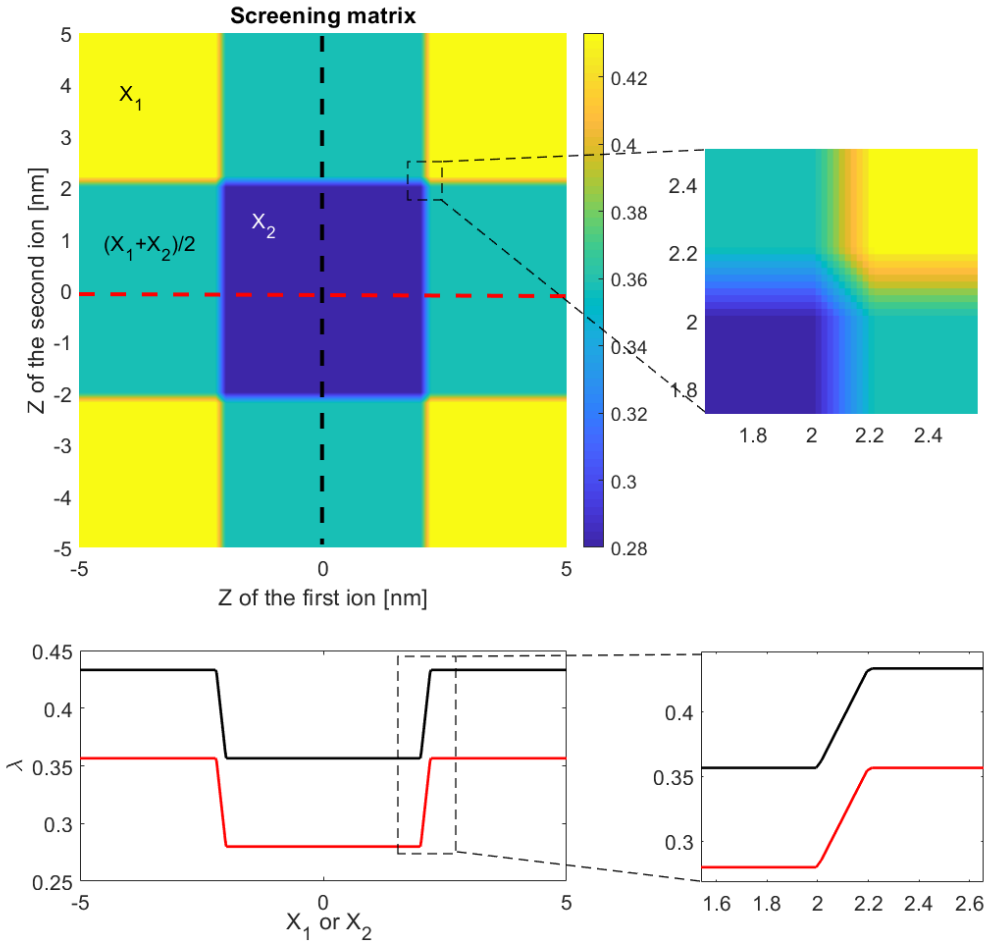

Figure 3.5: The top scheme demonstrates how the parameters of interaction of two ions are calculated depending on their positions. Bottom plots demonstrate the values of the parameter (in this particular example, the screening constant) along each the dashed cross-section of the colored picture (colors match on both images). This diagram is primarily required to describe a situation when one of the ions is located in the pore and another is in the reservoir.

addition one does not have to assume the dielectric constants of the proteins and dielectric self-energies on the protein-pore walls. Therefore, the implementation of PMFs into BD represents a hybrid model that benefits from both atomistic details – e.g. hydration effects – and BD's long-time trajectories [60, 113, 206]. Such a hybrid represents a sequential fixed-resolution multi-scale approach [13].

If one was interested in an artificial nanopore such as a hole in a graphene sheet (see Fig. 1.5) then the 1D single-ion PMF giving rise to the force in the Z-dimension can be deduced. However in more complex pores such as the KcsA biological channel, several ions may inhabit the channel and therefore a multi-

ion PMF should be considered. In this work we use the MD-generated single-ion PMFs for a graphene nanopore and the multi ion PMFs for the biological KcsA ion channel. These PMFs are shown in panels (a) and (b) of Fig. 3.6, respectively. Importantly, the PMF W_N depends on the number of ions N inside the channel. Thus, entering and leaving of ions from the pore result in switching between PMFs, what in turn provides essential information for the statistical and kinetic theories.

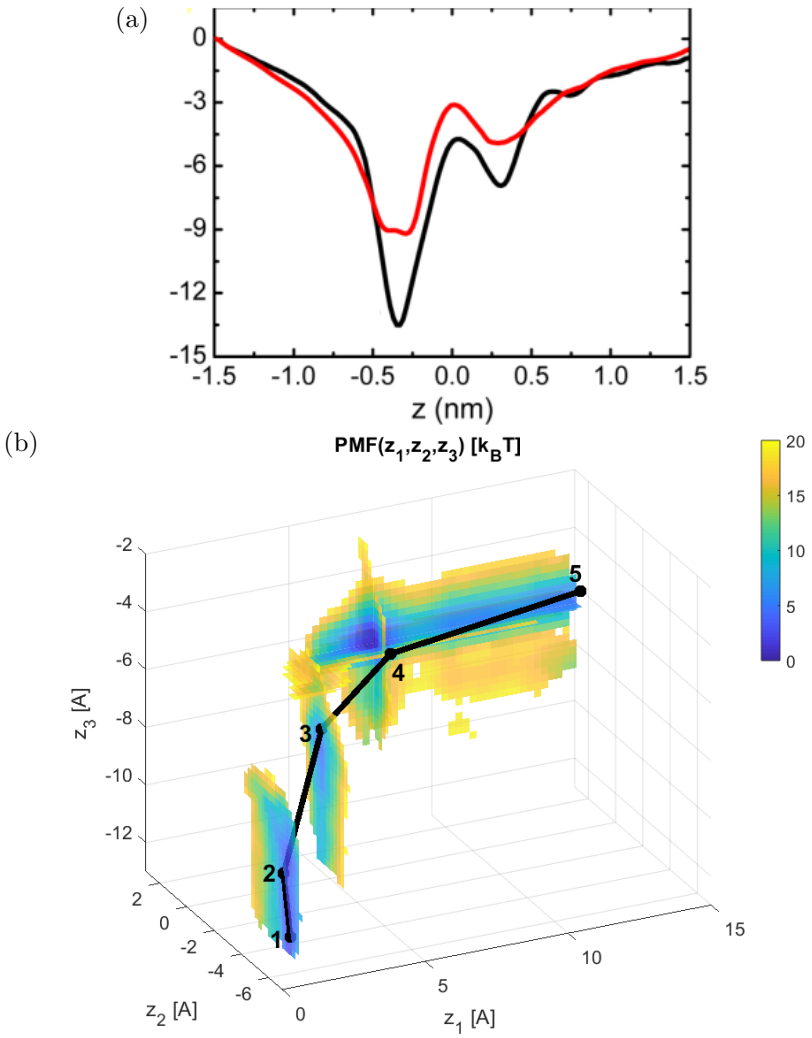

Figure 3.6: Examples of PMFs. (a) Single-ion PMF for K^+ (red) and Na^+ (blue) ions traversing a graphene pore. Adapted with permission from Ref. [87]. Copyright (2013) American Chemical Society. (b) Multi-ion K^+ PMF in the biological KcsA channel. Coordinates $z_1 - z_3$ are the ionic Z coordinates when counting from the channel's outer mouth. Numbers 1–5 represent the permeation milestones as described in Ref. [31]. Image taken from [207]. Courtesy to Dr. D. Medovoy and Prof. B. Roux for providing the original data.

Strictly speaking, one has to provide PMFs for all ions in the system to fully

describe the ion-channel interactions for each species. For instance, if KCl is used to study the KcsA channel, both the K^+ and Cl^- PMFs should be incorporated into the simulation. However, Cl^- never enters or travels through this channel due to repulsive and dehydration barriers. A more reasonable step in this circumstances is not to derive a computationally costly Cl^- PMF, but instead to use an analytical expression. Eq. (3.9), approximating the Cl^--channel interaction, can serve such an expression.

Stitching PMF to the domain When using a PMF in the channel and still having explicit ion-ion interaction in the bulk, one has to ensure that the ions in the channel are not subject to the explicit ion-ion interaction. So these explicit ion-ion interactions have to be "switched off" in the pore.

Finally, usually the multi-ion PMF is computed as a function of the ionic coordinate along the channel. This is done to save the memory allocated to save this data. In doing so, the transverse motions of ions are averaged over and not present explicitly. Although this omission is not expected to affect the physical results, one still needs to mimic this effect in a 3D BD simulation. A possible solution is to use a harmonic restraining potential (3.10) in the transverse directions. Thus the ions will be always kept on the channel's axis while their longitudinal motion is governed by the MD PMF.

3.4 Transmembrane potential

In the patch-clamp experiments, a typical setup involves applying voltage across the channel or the whole membrane. In a theoretical treatment, this is reflected by a potential difference via Dirichlet conditions at the opposite Z-edges of the domain [208].

Electrostatics can be treated in a number of ways [140]. First, the application of the constant electric field across the simulation domain (von Neumann conditions) [78] causes polarisation of the membrane protein developing its counter field.

The resulting potential profile drops/increases fastest in the pore while weakly decreasing from constant in the bulks [140, 209]. The second method is to set the potentials on either edge of the membrane (Dirichlet conditions) and to solve the Poisson equation (2.7). This can be done by means of finite volume solvers [177]. Lastly, one can consider dual-bilayer [112, 210] or air slab methods to mimic the creation of the potential difference from the charge imbalance [211].

In this work, we add the external electrostatic profile to the PMF. This can be done when the channel's structure does not vary to a large extent in the external field [17,122]. Two options to include the external voltage in a BD simulation have been tried: (a) by means of a linear voltage drop, and (b) by means of the `tanh(z)` function in the z-direction. The first option implies switching the electric field only when an ion enters the channel. This method provides a technically quick inclusion of the voltage drop, but does not account properly for the dielectric properties of the pore and the bulk. The second analytical approximation has been made to resemble the axial potential profile obtained in a finite-element solver. Fig. 3.7 demonstrates the two approaches and their comparison with the 3D solution.

Dielectric permittivity The description of the ion-ion interactions and applied external potential in the pore requires the specification of the profile of the dielectric constant. From the physical point of view, dielectric permittivity stems from the ability of water dipoles to reorient in response to an electric field. In bulk, where thousands of water molecules surround an ion, this process is allowed in all 3 dimensions. Thus, one can talk about the dielectric permittivity of the medium [212], being $\epsilon = 80$ for pure water. In contrast, in the confined environment such as a nanopore, the water molecules possess less rotational freedom and thus the dielectric permittivity is significantly smaller [213, 214]. In turn, this changes the dielectric response of an aqueous pore to an external electric field as well as the ionic interactions with neighbouring ions and the channel [202].

Here we use a constant dielectric permittivity of pure bulk water $\epsilon_w = 80$ in the pore and $\epsilon_p = 2$ for the channel protein. Although this common choice [16]

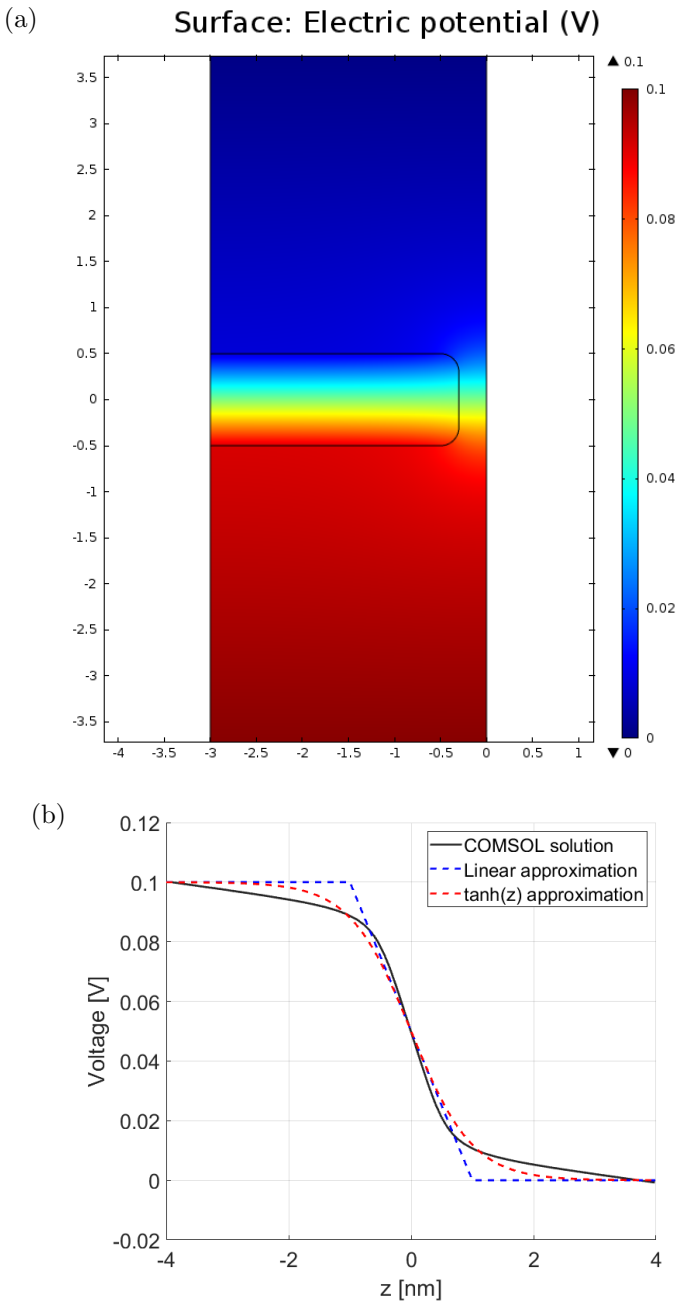

Figure 3.7: Electrostatic potential profiles. (a) Electrostatic potential in a pore model with radial symmetry. The left edge of the smaller rectangle corresponds to the pore axis. The potential difference (voltage) between the top and the bottom edges of the domain is 0.1V. (b) Electrostatic potential along the axis of the pore. Once can see that the voltage drops mainly across the pore and stays approximately constant in the bulks. This serves as a justification of the linear r `tanh`(z) approximation .

overestimates the dielectric properties of the pore, it has been shown viable in comparing BD simulations and experimental data [91]. For a more sophisticated analysis, spatially-dependent dielectric permittivity profiles should be estimated

in MD simulations [91].

3.5 Diffusivity

An important ingredient quantifying the mobility of ions in BD and PNP is the diffusivity of the ions. In free solution, ions undergo collisions with water molecules in 3D. In contrast, in a confined environment such as a nanopore, there are fewer water molecules and so fewer collisions. The ions also interact with the pore (its charged amino-acids) and each other [215], and therefore, overall the diffusivity in a channel is usually smaller than that in bulk [216, 217].

In the literature there is no commonly accepted model describing the single-ion diffusivity profile in a narrow channel and its mouths [197]. One method of extracting this profile is by considering an all-atom MD simulation using the velocity autocorrelation function [218]. The hydrodynamic approximation can also be used [219]. One can also use analytical approximations such as the diffusivity scaling factor $k(z) = D_{pore}/D_{bulk}$ [197]. It is also worth noting that, strictly speaking, different X-, Y-, and Z- diffusivities should be used in different spatial directions [117].

In the toy model, we use simple bulk diffusivity constants given in Table 3.1. It is known that under physiological conditions the ionic current is proportional to the diffusivity [20], therefore this approximation should yield good agreement for qualitative comparison with experimental data. However, for exact quantitative predictions one should rely on spatially-dependent diffusivity profiles computed in MD.

3.6 Time step

3.6.1 Choice of the time step

The duration of BD simulations exceed the Debye time τ_D ($\tau_D \approx 100$ps in a 1:1 solution of few molar) by several orders of magnitude, as required for the relaxation of the configuration of the ionic atmosphere [220]. However, to ensure computational efficiency the time step cannot be too small. It should be bigger than the inverse of the velocity autocorrelation function [221] to satisfy the Markovian assumption of the Langevin equation. At the same time, the time step Δt must be less than the time between two ballistic collisions. One can estimate the average thermal velocity as 130 m/s and inter-ion distance 1nm at concentration ~ 100mM, so that the time interval between collisions is ≈ 8ps.

The accuracy of a simulation can be compromised when large too time steps are used [16]. As a result the ions may not investigate all landscape features or may even fly through the channel [77]. This also suggests that large spatial displacements of ions and time derivatives of forces should not develop [222]. One more restriction may come from the integrator used, as often $\Delta t \ll 1/\gamma$ is expected to hold, making the simulation too long [130]. However, thanks to the use of the algorithm from Ref. [134] large time steps can be considered.

3.6.2 Step adaptation

During a simulation, ions can approach each other to within distances of $r \approx 2.7$Å [78]. This leads to the development of large forces due to the repulsive term (3.7) which, being included into the digitized scheme (C.1), leads to non-physically large displacements of both ions. This phenomena is known as long jump exceptions [132, 133] or steric clash [223]. As a result the continuation of a simulation may produce unphysical results or errors. Possible ways to avoid this problem are back retracing [132], reverse tracking [78] and so-called Metropolized algorithm to reject unrealistic steps [224]. Here we describe an adaptive time step

method to cope with long jump exceptions widely used in systems with hard-wall potentials.

The method reads as follows. When ions approach each other closer than the threshold value $r_0 = 2.8\mathring{A}$, the algorithm switches to the Euler scheme (3.4) and the time step is changed according to the rule

$$\Delta t^* = \Delta t \ (r/r_0)^\kappa, \tag{3.13}$$

as it is natural to decrease the step when $r \to 0$ [225]. Parameter κ has to be chosen carefully. It must satisfy the condition $\kappa > 10$ because forces develop as $\sim 1/r^{10}$. On the other hand, it cannot be too large because a too small time step Δt^* will require larger number of stages to cover the unaltered time interval Δt. Therefore, in our simulations we used $\kappa = 14$ as a trade-off between accuracy and computational efficiency, although other choices are possible. It should be also noted that only a few time step alternations are required per exception event.

In our case, at a relatively high KCl solution concentration of 0.5M, the ratio between the number of dynamically adjusted steps and the total amount of steps was typically $230/500001 = 4.5 \cdot 10^{-4} < 0.1\%$. To prevent the development of large forces in a deterministic manner, the time step is decreased by a factor of 10 every 500 steps and by a factor of 100 every 1000 steps, and thus can be seen as a double comb in Fig. 3.8.

When the adaptive time step is used, computation of the statistical averages should be adjusted correspondingly. Suppose a variable X is sampled at consecutive moments of time t_m, such that the sampled values are X_m. In case of the non-variable time step $\Delta t_m = \Delta t_0$, the time average is found according to the standard average formula

$$\langle X \rangle = \frac{\sum_{m=1}^{M} \Delta t \ X_m}{\sum_{m=1}^{M} \Delta t} = \frac{\Delta t \ \sum_{m=1}^{M} X_m}{M \Delta t} = \frac{\sum_{m=1}^{M} X_m}{M},$$

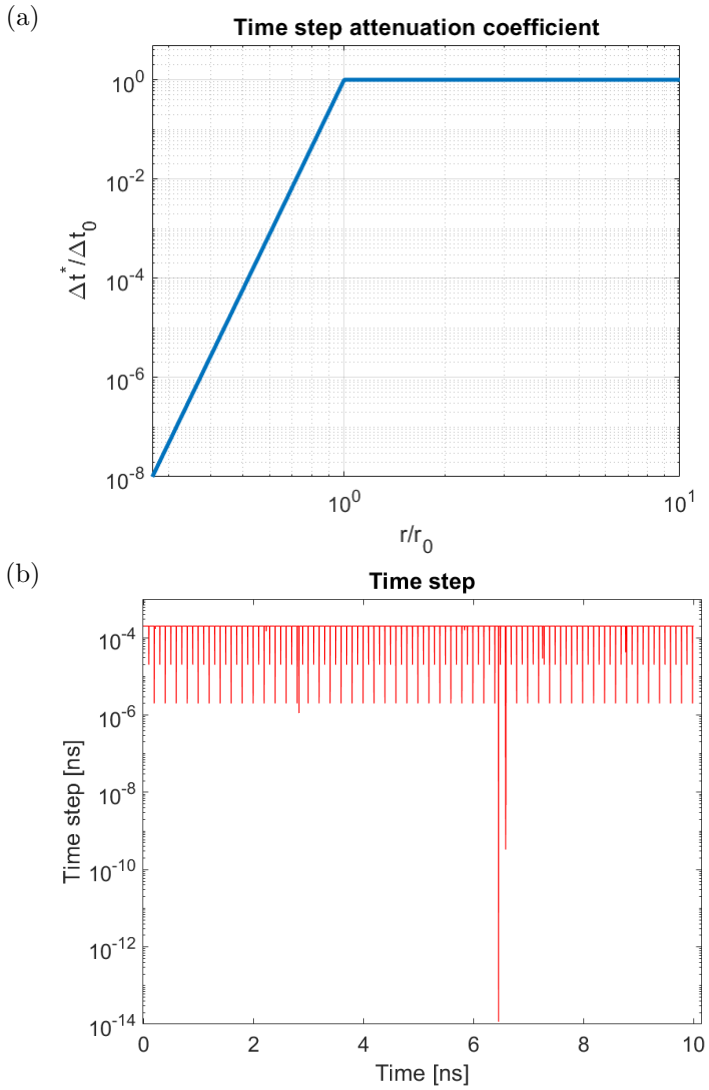

Figure 3.8: Showing the adaptation of the time step. (a) Attenuation coefficient for the time step depending on the inter-ion distance. (b) Variations of the time step in time. The regular "comb" is produced by planned step attenuations. Three dynamic step alterations can be seen near $t \approx 3, 6.5,$ and 7 ns.

In contrast, using the adaptive time step Δt_m requires one to use

$$\langle X \rangle = \frac{\sum_{m=1}^{M} X_m \, \Delta t_m}{\sum_{m=1}^{M} \Delta t_m} = \frac{\sum_{m=1}^{M} X_m \, \Delta t_m}{T} \tag{3.14}$$

in order to attribute the statistical weights adequately to each sample contribution.

In the formula above T stands for the whole time of the simulation.

3.7 Boundary conditions and injection schemes

As a BD simulates a finite 3D domain, one has to describe the physical properties of the geometrical constraints that determine this domain [16]. One therefore comes to the question of boundary conditions. The properties of the domain walls are rarely described, as rectangular simulation domains with periodic boundary conditions are typically used. However, this is not true for cylindrical and spherical geometry of the reservoirs, as well as the external walls of the GCMC buffers. When a domain boundary is set to be impermeable, this should be reflected in the program code.

We divide the algorithms into those that either maintain or vary the number of particles in the system. There are several subtypes of domains and corresponding implementation.

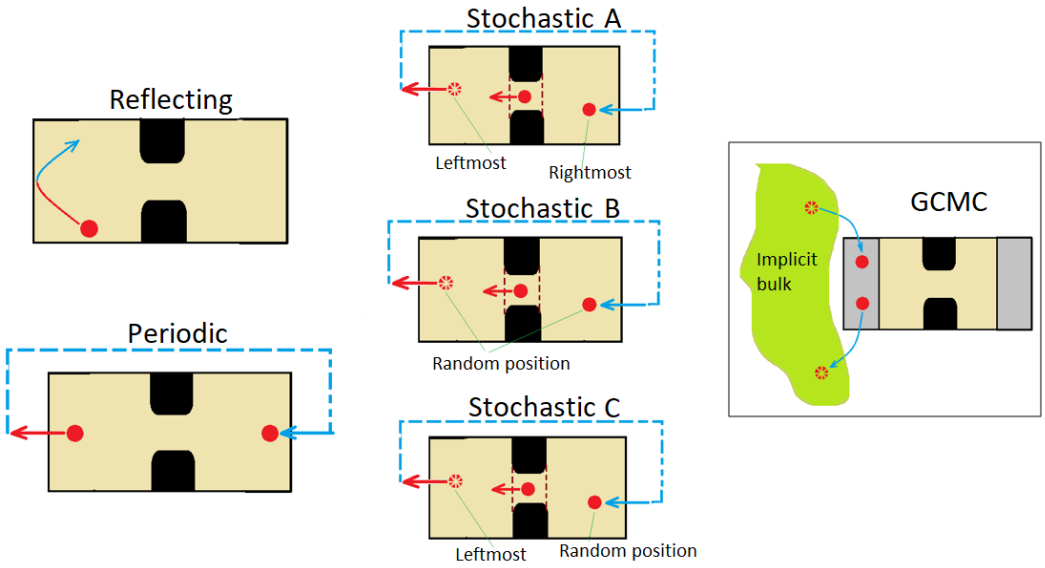

Figure 3.9: Schematic representations of how various boundary conditions work. The cellular membrane is illustrated by two black rectangles, the area between which represents the channel. The red part of the line represents the incident part of the trajectory and the blue part illustrates the effect of the particular boundary type. The reflecting condition prevents an ion from leaving the domain by reverting it back inside the domain. The periodic condition reinject the ion on the other side of the domain. The stochastic A-C boundaries describe what happens when an ion enter a reservoir. The GCMC boundary assumes that buffers (grey rectangles) are maintained according to the infinite bulk which is included implicitly.

3.7.1 Impermeable boundary (default)

The simplest type of boundary is an impermeable one (Fig. 3.9). It implies that an ion attempting to leave the domain is scattered back. Thus, if all boundaries are impermeable, the number of ions in the systems is preserved during the simulation. This occurs on the inner domain boundary between bulk and the lipid bilayer. The physical meaning suggests the implementation: one has to impose a repulsive potential perpendicular to the surface at the point of crossing. In simple geometries – planar, cylindrical or spherical, – it is trivial, while in a more complicated environment one has to be sophisticated. This implementation suggests "smooth" reflection regardless of the proximity to the wall. We applied these type of boundaries at the outer domain boundaries. This is because the number of particles between GCMC cycles has to be maintained constant. The reflective wall potential has to be included into the GCMC energy $W(n^\alpha)$. The presence of a soft repulsive wall may alter the density fluctuations in the system [154]. Therefore we have ensured that this potential develops only within 0.4Å near a wall, which is much smaller than the size of reservoirs ($\sim$ 3nm).

One can also implement a "hard" wall by detecting crossings, and just reversing the sign of the particle's velocity. The simplest way is just to leave the particle untouched until the next step, where due to the stochastic nature of the noise the force is likely to change its sign and thus point inwards. In this case, the particle's position is simply copied unchanged to the next moment of time, and the particle loses its initial velocity. If it happened due to a random force pointing outwards, its sign is likely to change to the opposite in the next step. However, if two ions came too close to each other near a wall and thus a long jump exception emerged, a mandatory regular shake-up would unravel them. Both these methods create a $\sigma = \sqrt{(2D\Delta t)}$ depletion zone with an `erfc(z)` profile in the immediate vicinity of the membrane [135]. For a reservoir of several nanometers extent in all dimensions, this depletion zone is negligible.

Impermeable boundaries can be applied to a system to speed up a simulation.

We used those conditions in the X- and Y-dimensions, as well as on the outermost boundaries along Z axis when the GCMC conditions were applied.

3.7.2 Periodic boundary conditions (at the outer domain boundary)

Another method of keeping the number of particles constant is to apply the periodic conditions at the outer domain boundaries. This method suggests that, when a particle leaves the domain through a plane wall, it re-appears at the opposite wall (Fig.3.9). This is done by adding/deducting the inter-wall distance from the new coordinate of the particle. This algorithm suggests using a rectangular box, therefore for a cylindrical wall or other curved surface there is no such a simple re-injection rule.

This boundary condition is the default in MD. Spurious near-wall depletion is absent, and the underlying torus topology (opposite domain walls are identified) forces us to consider only equal concentrations in both bulks. To move beyond this constraint one can introduce a two-membrane domain [112, 210] but at increased computational cost due to the increased number of particles involved. Also, one should ensure at least 1nm in each dimension of the simulation box to suppress the unphysical effect of ions interacting with their own images when the minimal image convention is used.

3.7.3 Stochastic boundary

This is one of the classical methods. It implies that when a particles leaves the channel and enters say reservoir A, another leftmost particle of the same species in reservoir A is selected and added to reservoir B at the rightmost position. This effectively closes the electric circuit formed by two bulks and the channel [16].

A possible simplification of the above method is that when a particle crosses e.g. the left edge of the channel and enters reservoir A, another outermost particle of the same species in reservoir B is selected and is *randomly* positioned in reservoir

A. When no voltage is applied that is satisfactory, while if voltage is applied this method creates an inhomogeneous spatial distribution of ions.

3.7.4 Injection into a 1D domain

Considering 1D BD, one may want to inject/remove ions from the domain. Such a necessity emerges e.g. when the reservoirs have to be modelled at two different concentrations. To do so, one first uses the formula

$$j = 2\pi DRC \tag{3.15}$$

to estimate the injection rate of non-interacting particles. Here, D is diffusivity, R is the radius of the channel's mouth and C is ionic concentration. Then, one generates a set of exponentially distributed times with the time constant $\tau = 1/j$. These will be the times when an ion has to be added to the simulation. The latter is done simply by finding a numerical cumulative sum of the set of times.

In a 1D BD simulation, one then adds a particle according to the injection moments. To avoid depletion zones in the vicinity of the channel edges, particles should be added not exactly at the edge but in the adjacent zones with probability `erfc(z)` [135]. This is a consequence of the method of images [142, 226] . One should also ensure that the injection sources are time-step-dependent to avoid the dependence of the particle profiles on the time step [135]. The problem of this injection type is that it was designed for non-interacting particles, while these in a solution do interact and this interaction affects the entry dynamics.

3.7.5 Grand Canonical Monte Carlo

In Ref. [141] the authors introduced a method to generate a source of ions at a predefined concentration level. It combines the Grand Canonical μVT ensemble with the Monte-Carlo trials thus allowing the number of particles to fluctuate [141, 218]. The method suggests having a buffer ~ 5Å thick [140, 141] attached to each

reservoir, and adding/removing particles to it. An adding attempt starts from the random generation of a coordinate within the buffer. One then attempts computes the acceptance probability [141]

$$P^{\alpha}_{creat} = \frac{\dfrac{\bar{n}^{\alpha}}{n^{\alpha}+1} e^{-(\Delta W^{\alpha} - \bar{\mu}^{\alpha})/k_B T}}{1 + \dfrac{\bar{n}^{\alpha}}{n^{\alpha}+1} e^{-(\Delta W^{\alpha} - \bar{\mu}^{\alpha})/k_B T}}. \tag{3.16}$$

Here $\bar{n^{\alpha}}$ is the expected number of ions of species α in the buffer, n^{α} is the current number of ions α in the buffer (integer), $\Delta W^{\alpha} = W(n^{\alpha}+1)^{\alpha} - W(n^{\alpha})$ is the free energy difference of *adding* an α ion to the buffer, and $\bar{\mu}^{\alpha}$ is the excess chemical potential for species α. The acceptance criterion means that if a newly generated random number $\xi \in [0,1]$ satisfies $\xi < P^{\alpha}_{creat}$, this particle is added to the set of particles in the buffer ("acceptance"). Otherwise, the trial is rejected. The input excess chemical potentials $\bar{\mu}^{\alpha}$ for each ionic species can be calculated from the microscopic model of ion-ion interactions by combining the hypernetted chain (HNC) equation [227] and the Ornstein-Zernike equation [218], or with the help of the separate iterative GCMC simulation [228, 229]. The consideration of electrostatics requires the solution of the Poisson equation to span into the buffers [140, 141]

Similarly, a removal step is implemented. First, one has to ensure that the buffer is not empty. After that, a particle in the buffer is selected randomly. The removal probability level in this case reads as

$$P^{\alpha}_{remove} = \frac{1}{1 + \bar{n}^{\alpha}/n^{\alpha} e^{-(\Delta W^{\alpha} - \bar{\mu}^{\alpha})/k_B T}} \tag{3.17}$$

where $\Delta W^{\alpha} = W(n^{\alpha}) - W(n^{\alpha}-1)$ is the free energy difference to remove one ion from the buffer. If another random number is accepted, the coordinates of the selected particle are removed from the set of current coordinates ("removal" by assigning `NaN` values in place of the 3D coordinates). Otherwise, the coordinates are left untouched [227, p.44]. The physical meaning behind the formulas is to

allow a step that leads to a lower system's energy [230].

For microscopic reversibility (the principle of detailed balance), one has to ensure that addition and removal steps are attempted with equal probability [110, p.128]. This suggests equiprobable random switching between addition and removal steps. If neither was selected, the system is left unchanged. In our simulations, the ratio between addition, removal, and BD is respectively 1/4 : 1/4 : 1/2 [141], although other ratios exist, for instance 1/3 : 1/3 : 1/3 [231] or 2/5 : 2/5 : 1/5 [132]. The choice is made as a trade-off between the simulation speed (GCMC is a time-consuming procedure) and the accuracy of reproducing bulk concentrations. This implies that having many GCMC attempts (as much as 1000 in [132]) allows one to sample the buffer configuration perfectly. However, that many attempts significantly slow down the simulation, because the remainder of the system (ions in reservoirs and, importantly, inside the channel) do not move.

Each GCMC cycle – addition, removal, and BD step – is applied to each ionic species sequentially, and the whole loop is repeated 10 times. The number of GCMC attempts should be at least equal to the expected number of ions in the buffer. Otherwise the buffer will become insufficiently sampled what in turn will cause incorrect ionic densities in reservoirs and affect ionic currents through the channel.

The Metropolis algorithm [230] allows us to generate new statistically relevant configurations [232]. The application of Grand Canonical insertions/deletions allows for less system-size dependence as compared to the Widom's insertion methods in the Canonical Ensemble due to the breach of electroneutrality [229]. However, at high particle densities the GCMC method loses its attractiveness: attempted additions are massively rejected as there is little room to insert a particle [233, 234].

A GCMC bunch (10 trials) maintains the prescribed concentrations within a time interval. If the bunch is applied at each time step, this means the bulk is provided continuously. However, if this procedure is applied once per several steps

(as e.g. in [132]) this would result in two concentrations – buffer and reservoir – being mixed. This in turn supposes that the concentration takes the mean (weighted) value between buffer and reservoir values, and is different from the prescribed value. The less frequently the GCMC bunch is applied, i.e. the less frequently the buffer concentrations are updated, and the more uncontrolled the reservoir concentrations become. For instance, applying a GCMC bunch (10 trials) only once per 1000 time steps resulted in the buffers being positively charged.

One of the main advantages of the GCMC method is its ability to consider the left and right bulks independently. For instance, one can set up a 0.1mM KCl solution in the left bulk and a 0.5mM in the right bulk. Another example is to have KCl on the left and NaCl on the right – this configuration mimics the standard patch-clamp environment aimed at exploring selectivity in the KcsA channel [45]. Also, asymmetrical bulks are required to study the blockage of KcsA by the intracellular Na^+ [73]. Finally, one can consider ionic concentrations in the micromolar range using standard sizes of the simulation domain. Otherwise, one would need to introduce enormous reservoirs, what in turn incurs high computational costs [140, 141]. Thus, the simulation of arbitrary experimental conditions becomes feasible.

Figures 3.10 and 3.11 show the numbers of ions in both buffers and reservoirs over time. The preset values, set in the GCMC cycle, are shown by circles, confirming good operation of the algorithm. The number of ions in a buffer varies when ions are added or removed or enter from the reservoir. Similarly, the reservoir occupancies change when ions appear from either buffer or enter / leave the reservoir through the ion channel. The overall time-averaged number density along the domain axis is shown in Fig. 3.12.

3.8 Measurements of current

Once the simulation is set up, it can be run to yield the required observable quantities. Typically the initial stage of the simulation, about 0.2 μs is considered

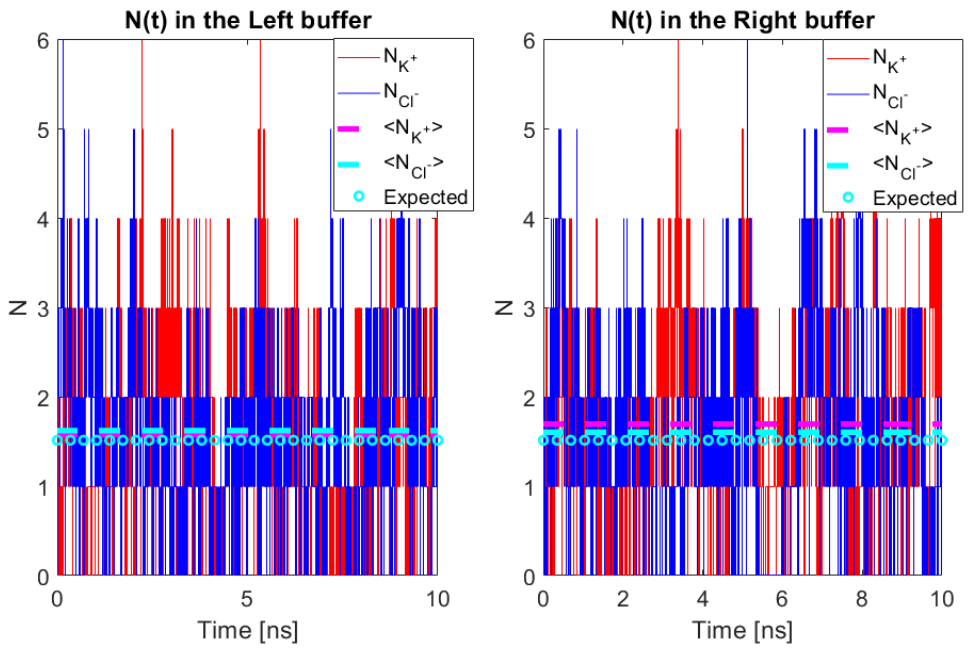

Figure 3.10: Control of buffers in time. The solid lines show the present amount of K^+ (red) and Cl^- (blue) ions. Corresponding time-averaged values are given in pink and cyan, respectively. Preset expected values are illustrated by cyan circles for both ionic species.

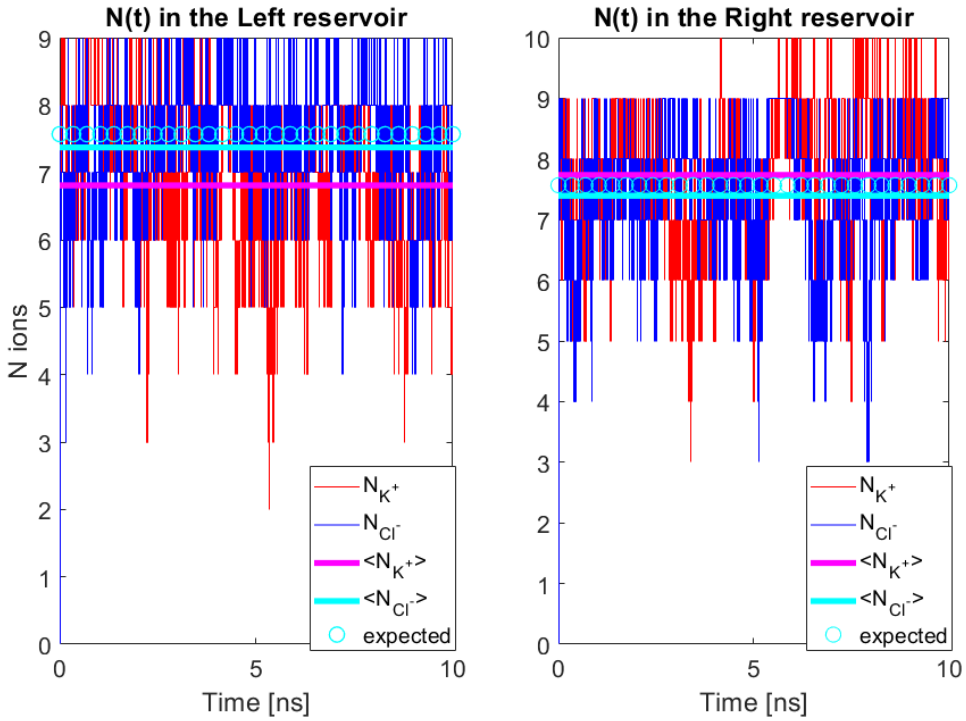

Figure 3.11: Occupancy of both reservoirs in time. Red and blue step curves show the amount of K^+ and Cl^- ions, respectively. Corresponding pink and cyan lines represent the time-averaged values. Cyan stars provide the preset expected number of ions in the reservoir.

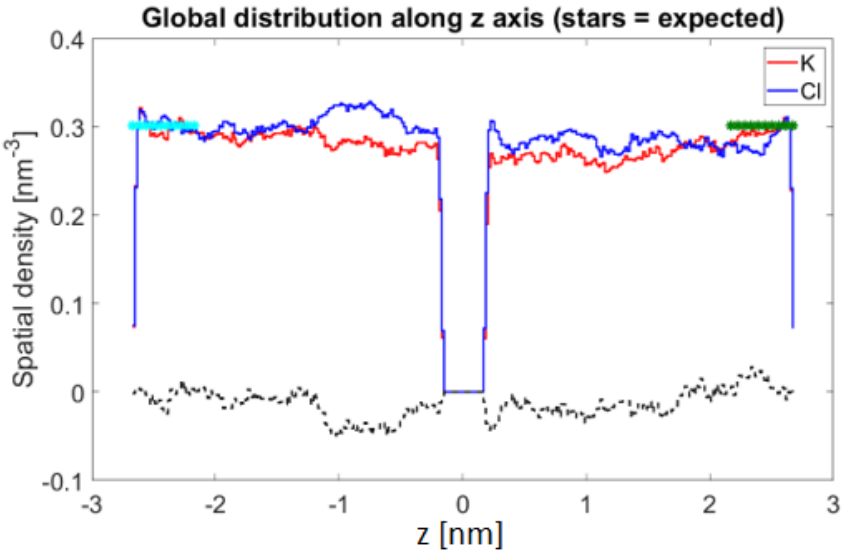

Figure 3.12: Axial distributions of K^+ and Cl^- in the reservoirs show good agreement with predefined values in the buffers (cyan and green stars). The dashed black line indicates the imbalance of the spatial charge density.

as an equilibration interval and therefore not included in the analysis [165].

To measure the main observable – the electric current – one typically counts the cumulative number of ion crossings through an imaginary surface. Under steady conditions it may be any cross section of the system [235]. One measures the number of transitions in one direction $N_{L\to R}$, that in the other direction $N_{R\to L}$, and finds the net number of crossing $N = N_{L\to R} - N_{R\to L}$. Given that there are N crossing events of ions with valence z_m during the time interval T, the current is calculated according to the textbook definition

$$I = \frac{N z_m q}{T}. \tag{3.18}$$

This formula, implemented in the current thesis, clearly indicates the necessity to have longer simulations as the number of crossings N is proportional to the simulation time. The statistical error of the current correspondingly decreases as $\sim \frac{1}{\sqrt{N}}$. One can alternatively measure the electric current via the displacement current using *all* atoms as is implemented in MD simulations [209, 236], or by means of Ramo-Shockley theorem [237].

Equation (3.18) implies that only transitions through the pore are counted, so

the the geometrical boundaries of the pore are involved. The MD method appears as more straightforward [209] as it only requires the spatial displacements of all ions within the domain and "unwrapping" of the coordinates when the periodic boundary conditions are applied. Both these methods rely on the variation of the 3D coordinates of ions. The Ramo-Shockley approach in addition requires the calculation of the electric field in the absence of all mobile charges in the system, including the ions in the bulk solution, in the pore, and the mobile charges embedded in the protein [237].

3.8.1 Ionic currents through a graphene nanopore

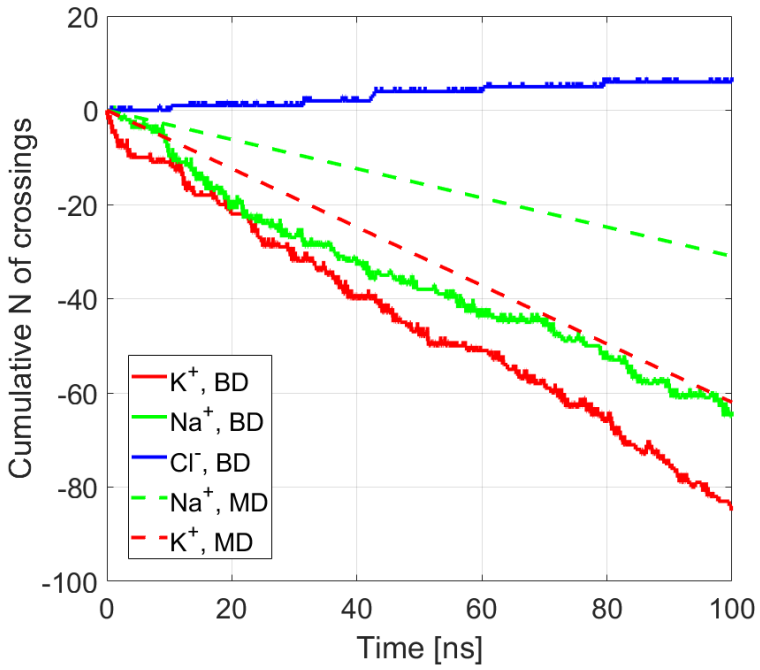

Figure 3.13: Smooth lines: cumulative crossings of the K^+ (red), Na^+ (green) and Cl^- (blue) through a graphene nanopore, calculated in a BD simulation via the single-ion PMF 3.6(a). Dashed lines show the traces of 50pA and 100pA currents corresponding to Na^+ (dashed green) and K^+ (dashed red) currents found in MD simulations [87]. Solutions comprise 0.5mM KCl and 100mV voltage is applied.

As an example, we run a simulation with 1-ion PMF, Fig. 3.6, and ion-ion interaction according to Eq. (3.6). Symmetrical solutions comprise of 0.5mM KCl and 100mV voltage is applied from the left. In Fig. 3.13, the cumulative number of pore crossings in time is shown. One can see that K^+ ions permeate faster than

Na^+. This is expected as the single-ion potential for K^+ is shallower that that of Na^+, so it is easier for the K^+ ion to escape the well after e.g. a collision with another K^+ ion. This is a manifestation of the K^+/Na^+ selectivity, also found in MD simulations [87]. The discrepancy of a factor of ~ 2 between BD and MD currents is expected to stem from the smaller value of the pore's radius used is BD.

A PMF for the chloride ions was not available in Ref. [87], and we therefore modelled it via Eq. (3.9). Due to repulsion from the negative fixed charge of the COO^- and the dehydration barrier, chloride ions permeate less frequently. This provides an example of the cation/anion selectivity.

3.8.2 Toy model of the KcsA channel

Further, we simulated the ionic currents in a toy model of the KcsA channel. Two typical experimental configurations are considered: current-voltage curves at fixed bulk concentrations and current-concentration curves at fixed voltage. The first type suggested 200mM KCl solutions in both bulks, and application of voltage in the `tanh` approximation. The second type of settings supposed KCl solutions in bulks, the right one being fixed at 200mM and the left one variable. The external voltage drop in this case was set to zero. Each simulation covered 0.1-1 μs of the ion's dynamics.

The results are shown in Fig. 3.14. The top figure demonstrates that current increases with voltage as expected. Each data point and the corresponding error bars resulted from 5 BD simulations each 1-μ long. The bottom figure demonstrates the reversal of current when the ratio of left and right concentrations crosses the unit value. This is expected as the concentration gradient correspondingly reverses.

The simulation also agrees qualitatively with the published data on ionic currents through the KcsA [70, 75]. Regarding the quantitative values, the simulated currents lie close to the experimental data points. The reason for existing quantitative discrepancies is selection of parameters and the simplified character of the

model. These parameters include the pore radius R_c, and the length of the channel L_{ch}. The latter is $L_{ch} = 4$nm while the selectivity filter of the KcsA channel is 1.2nm long. The form of ion-ion interactions inside the channel was parameterized to mimic 2-3-2 conduction, while in the simulation we also detected occupancy states with a single K^+ ion. It is also worth noting that the diffusivity D and dielectric permittivity ϵ inside the channel were considered constant, while MD studies report attenuation and spatial dependence of these parameters. Finally, the toy character of the model suggests a simplified ion energy landscape inside the channel and therefore its the particular features are overlooked. To conclude, good qualitative agreement is found, but a preliminary calibration of the simulations by comparison with published data is typically required.

3.9 Summary

In this Chapter, a Brownian dynamics (BD) system has been described. This BD simulation program has been extensively described with specific focus on the physical effects and reasoning of the choice of parameters. It has encompassed the choice of integrators, computation of the transmembrane potential, diffusivity profile, adaptive time step, and boundary conditions. Each of these components has been analysed carefully to optimize the performance. Importantly, this BD system allows to account for the potentials of the mean force (PMF), generated in a separate molecular dynamics (MD) study. Thus, one gains the opportunity to account self-consistently for the channel's atomic structure, ion-ion, ion-water, ion-ligands and ion-pore interactions with atomic resolution, thus abandoning the need to approximate these parameters.

Essential properties of the channel arise from the way in which ions interact with each other and with the channel inside the pore. In that way, one can use either compound potential or a multi-ion potential of the mean force (PMF). The former assumes splitting interactions into the ion-channel and ion-ion components. The main difficulty here arises from the way these are calculated and approximated,

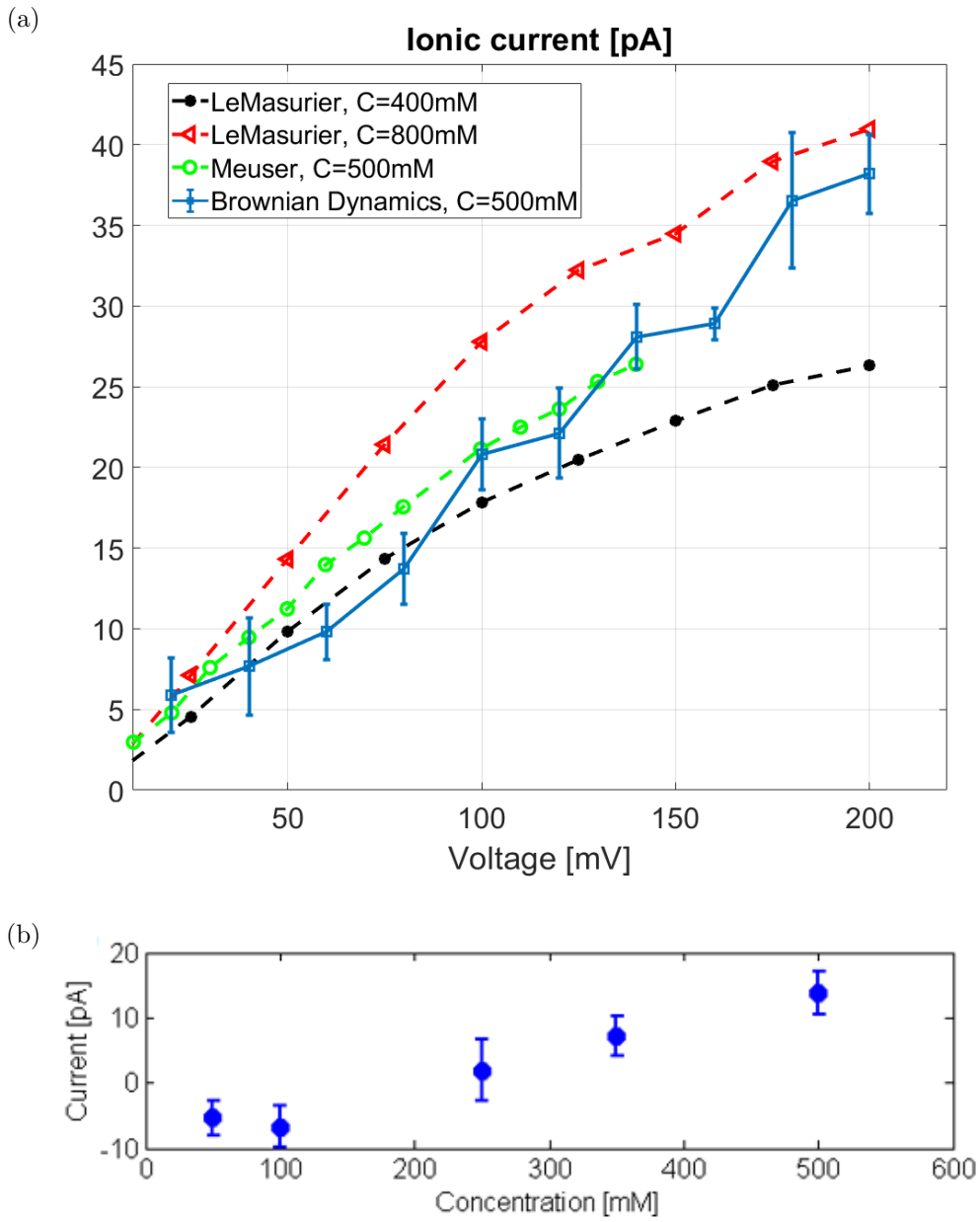

Figure 3.14: BD simulation results of currents through a toy model of the KcsA channel. (a) Current-voltage curves represent the increase of current in response to voltage. Symmetrical bulks are considered, each carrying 500mM KCl solutions. Results from a BD simulation (blue squares) with errorbars are shown. Dashed lines represent the experimental data from Refs. [70, 75] for 400mM (black dots), 500mM (green circles) and 800mM (red triangles) in symmetrical solutions. Connecting lines provide a guide for the eye. (b) Current-concentration curves at zero voltage. The concentration of the right bulk is maintained at 200mM while that of the left bulk varies. When crossing the point of equal concentrations, the current reverses its sign, which is an expected outcome of reversing the concentration gradient.

because interactions differ in free bulk and in the confined environment of an ion channel. This problem can be circumvented by use of a multi-ion PMF which

encompasses all the aforementioned interactions. Thus, separate ion-ion or ion-protein interaction need not be assumed. As long as the dimensions perpendicular to the pore do not contribute to the ionic current, these can be described by means of an analytical approximation. Thus, only the Z-components of PMFs in MD need to be saved.

Analysing the boundary conditions, we find that one has to take into account the experiment to be mimicked, and computational power required to implement them. Approaches maintaining the number of ions in the system, such as periodic or stochastic, impose little burden on the simulation and are easy to implement. However, these conditions do not allow for the consideration of asymmetrical bulks. In that regard, the Grand canonical Monte Carlo (GCMC) approach is the most flexible as it appropriately grasps the variety of the electrophysiological experimental conditions. The GCMC method, however, requires more sophisticated implementation and is more time consuming. It was shown that the implementation of both types of boundary – preserving and not preserving the number of ions, – may be necessary for efficient BD simulation.

In order to confirm that each section of the BD code works properly, a number of tests has been undertaken. We checked that the system's energy does not drift in time and that the numbers of ions correspond to the chosen values. The numbers of ions in the reservoirs have been demonstrated to agree with the corresponding preset quantities which validates the functioning of the domain boundaries. Number density profiles were shown to agree with the preset values in the GCMC buffers. A number of other auxiliary tests, listed in Appendix A, has taken place as well during construction.

Finally, we have applied our BD simulator to study ionic translocation in two systems. The first one is a graphene nanopore with a charged rim due to the carboxylate COO^- group for which the PMFs have been evaluated in MD [87]. The BD simulation reveals not only the conduction of the pore, but also its selectivity. The pore's ability to conduct K^+ preferentially over Na^+ is related to the difference

between PMFs, while the large rejection of Cl^- ions occurs due to the electrostatic repulsion exerted by the carboxylate oxygen atom.

The second system mimicked the biological KcsA ion channel. The interactions of an ion with other ions and the channel were approximated as discussed in section 3.3.1. The simulation reproduced the increase of current in response to external voltage, and the dependence of ionic current on the ratio of bulk ionic concentrations. Overall, good qualitative agreement with experimental findings [70, 75] was found, the quantitative discrepancy being attributed to the toy nature of the model and the choice of the pore parameters.

Future work to improve the scope of the model might be to introduce multiple scales of adaptive time step. For instance inside the channel a smaller time step can be chosen to allow ions to study thoroughly all peculiarities of the potential landscape in the channel [77]. Profiles of diffusivity and dielectric permittivity, measured in MD, should provide further atomistic accuracy and improve the quantitative agreement with experimental data. The program can also be improved by incorporation of the electrostatic field computed by a 3D FEM Poisson solver. This suggests tabulating the electrostatic field and using it further as a look-up table. For simple pore geometries one can use COMSOL Multiphysics [238] or the finite-volume Poisson solver [177]. More realistic inclusion of electrostatics can be implemented via Delphi [173], APBS [174] and induced charge computation methods [239].

To conclude, a BD simulation system incorporating the MD PMFs, has been built. It allows one to account for a channel's structure with atomic resolution of the potential energy landscape, and to compute ionic currents through the nanochannel. These currents can be further validated by comparison with experiments or with MD simulation data.

4. Quasiparticles in narrow ion channels

> "Every great and deep difficulty bears in itself its own solution. It forces us to change our thinking in order to find it."
>
> *N. Bohr*

4.1 Introduction

As discussed in the Introduction and Methods (chapters 1 and 2, respectively), the highly-correlated motion of ions in the narrow selectivity filters of ion channels cannot be described by a mean-field theory. The method capable of grasping this problem – molecular dynamics – does not allow one to compare single-channel currents routinely with experimental data. To connect the atomistic structural features with the continuous description, one needs to account for the ion-ion correlations. This can be done by virtue of the concept of a quasiparticle.

The notion of a quasiparticle can be used to describe collective ionic motion in narrow channels [144, 240]. This concept reduces the complexity of many-body motion to the one-dimensional motion of a single quasiparticle in an effective potential, providing a very clear physical interpretation of permeation [144, 241]. The idea was introduced in relation to a simple toy model, and the quasiparticle

concept still needs to be connected to the structures of real channels.

Here, we extend this concept and derive an explicit relationship between the effective potential of a quasiparticle and the multi-ion PMFs related to the structure of the channel. Thus, the channel's atomic structure, ion-ion, ion-water, ion-ligands and ion-pore interactions become automatically incorporated. The formula is validated on the toy model of ion-ion and ion-channel interactions from Refs. [144, 240] to simplify the comparison between the theoretical and BD simulation results. We also investigate the correlation between an entering/leaving ion and the quasiparticle, which provides physical insight into the dynamics of the transition process.

The results of this Chapter have been published in Refs. [207, 242].

4.2 Methods

4.2.1 The motion of individual ions

As discussed in the Chapter 1, the selectivity filter (SF) of the biological KcsA ion channel, shown in Fig. 3.1, is only a few angström wide [19]. Due to this narrowness, the permeating ions cannot pass each other and therefore move effectively in one dimension. This allows us to simplify ionic motion in the SF to dynamics along the channel's longitudinal axis z. The Langevin equation of motion for the k^{th} ion of species α is given by Eq.(3.1), the force begin given by

$$\mathbf{F_N}(\mathbf{r}^{\alpha}_{\mathbf{m}}) = -\frac{\partial W_N(\mathbf{r}^{\alpha}_m)}{\partial \mathbf{r}^{\alpha}_m} \tag{4.1}$$

where an N-particle PMF is given by Eq. (2.3). The PMF in the selectivity filter of the KcsA channel is illustrated in the right panel of Fig. 3.6b.

As indicated above, the use of MD-generated PMFs in studies of nanoscale systems yields several benefits. For instance, it self-consistently includes the ion's interactions with other ions in the pore, the effects of dehydration at the entrance

and inside the channel, the induced charges on the pore walls, and the influence of the flexible pore structure. Using state-dependent PMFs, we take a step towards using the dynamical potential landscape [113].

4.2.2 Motion of quasiparticles

Importantly, the one-dimensional motion and strong ion-ion interactions allow one to describe ionic collective [19] behaviour as the motion of a "quasiparticle" (QP) [144], represented by the centre of mass q^α and relative distances p_m^α between neighbouring ions of a given species

$$q_N^\alpha = \frac{\sum_{k=1}^{N^\alpha} z_k^\alpha}{N^\alpha}, \quad \alpha = \mathrm{K}^+, \mathrm{Cl}^-, \ldots \tag{4.2}$$

$$p_k^\alpha = z_{k+1}^\alpha - z_k^\alpha \tag{4.3}$$

with respective velocities $v^\alpha = \dot{z^\alpha}$ and $\dot{p}_k^\alpha$. Here ions are numbered from outside to inside as in [31] and N^α represents the total amount of ions in the channel. The inverse coordinate transformation $z_k^\alpha = z_k^\alpha(q_N, \mathbf{p})$ is given by Cramer's rule where, for clarity of notation, the set of relative distances is written as a vector [144] $\mathbf{p} = \{p_1, p_2, \ldots, p_{N-1}\}$. Generalization for multiple species is straightforward, and unless explicitly stated we omit species' indices in specifying the ion's and QP's coordinates, for clarity. It is worth noting that the QP defined above [144, 240], also known as a "quasi-ion" or a "super-ion" [241], represents the centre of mass of the ions, whereas a "quasi-ion" ("permion") [153, 243] includes the ion, water molecules and the protein channel.

The potential energy of the system of ions located at $\mathbf{Z} = (z_1, z_2, \ldots, z_N)$ is given by the PMF $W_N(z_1, z_2, \ldots, z_N)$. By expressing the coordinates of individual ions $z_k = z_k(q, \mathbf{p})$ via their centre-of-mass and relative distances $\{q, \mathbf{p}\}$, one can express the energy of the system via the parameters of the QP: $W_N = W_N(q, \mathbf{p})$.

In the spirit of Ref. [144], we use the full Langevin equation (3.1) to describe

the evolution of the QP's position q^α in time

$$\ddot{q}_N = -\frac{k_B T}{m D_N^*}\dot{q} - \frac{1}{mN}\sum_{k=1}^{N}\frac{\partial W_N(z_k(q,\mathbf{p}))}{\partial z_k} + \sqrt{\frac{2(k_B T)^2}{D_N^*}}\xi(t) \tag{4.4}$$

$$\ddot{p}_k = -\frac{k_B T}{m D_N^*}\dot{p}_k - \frac{1}{m}\left[\frac{\partial W_N(z_{k+1}(q,\mathbf{p}))}{\partial z_{k+1}} - \frac{\partial W_N(z_k(q,\mathbf{p}))}{\partial z_k}\right] + \sqrt{\frac{2(k_B T)^2}{D_N^*}}\xi(t) \tag{4.5}$$

The coefficient D_N^* represents the transport diffusivity [244]. For interacting particles, this coefficient differs from a simple product ND between the number of ions N and diffusivity D given in Ref. [144].

Applying the chain rule and making use of the definitions (4.2)-(4.3), one arrives at

$$\begin{aligned}
\ddot{q}_N &= -\frac{k_B T}{m D_N^*}\dot{q}_N - \frac{1}{m}\frac{\partial W_N}{\partial q_N} + \sqrt{\frac{2(k_B T)^2}{D_N^*}}\xi(t) \\
\ddot{p}_k &= -\frac{k_B T}{m D_N^*}\dot{p}_k - \frac{1}{m}\left[2\frac{\partial W_N}{\partial p_k} - \frac{\partial W_N}{\partial p_{k-1}} - \frac{\partial W_N}{\partial p_{k+1}}\right] + \sqrt{\frac{2(k_B T)^2}{D_N^*}}\xi(t)
\end{aligned} \tag{4.6}$$

The above equations apply to the diffusion of a QP consisting of a fixed number of ions. However, during permeation this number varies. For instance, the knock-on mechanism, when an incoming ion causes the furthermost one to leave the channel, appears to be inherent to the KcsA potassium channel [19]. The non-constant N has two important consequences. First, it implies that the set of energy landscapes W_N for a QP is discrete, as we demonstrate explicitly in section 4.3. Secondly, the discrete changes of pore occupancy lead to spatial jumps of the QP (Fig.4.1(a)). The positions of a QP before and after a jump are coupled [144]. For instance, for an N-ion QP located at q_N, the entry (exit) of an ion from side S relocates it to q_{N+1} (to q_{N-1}) according to [144]

$$\text{ion enters: } q_{N+1} = \frac{N q_N + S}{N+1}, \qquad \text{ion exits: } q_{N-1} = \frac{N q_N - S}{N-1} \tag{4.7}$$

as shown in Fig. 4.1(b). Thirdly, the diffusivity, charge, mass, and effective poten-

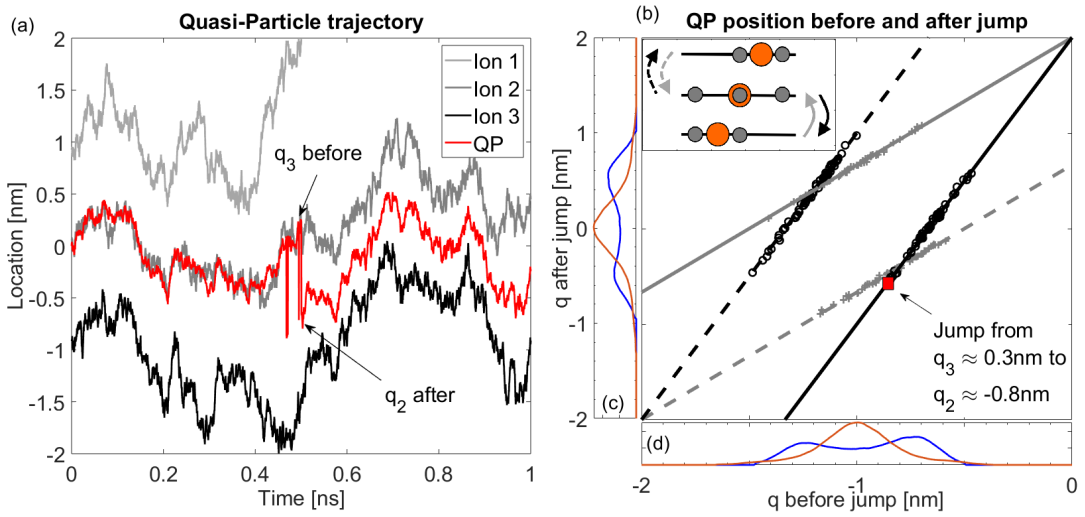

Figure 4.1: **(a)** Example of QP motion in Brownian dynamics simulations, illustrating a 3-ion QP that evolves into a 2-ion QP. Individual ionic trajectories (black and grey traces) result in the motion of their corresponding QP (red). At time $t \sim 0.5$ns the rightmost ion leaves the channel; two ions remain, and the QP consequently jumps from q_3 to a new position q_2. **(b)** The connection between the QP coordinates before (plotted on the abscissa) and after (on the ordinate) a jump. Each BD data point describes a single jump q_3 to q_2 (a circle) or q_2 to q_3 (a cross). The set of q_3 to q_2 points fall on the steeper pair of parallel lines, each point corresponding to an individual ion's entry/exit through either the left (dashed lines) or the right (solid lines) edge of the channel, as illustrated in the inset where individual ions are grey and the larger orange circle represents the QP. The set of q_2 to q_3 points fall on the similar but shallower pair of lines as described. In each case, the lines represent the theoretical predictions of Eq. (4.7). The red square indicates the q_3 to q_2 jump shown in panel (a), when the rightmost ion exits the channel (pale grey trajectory). **(c)** and **(d)** show the equilibrium distributions for 2-ion (orange) and 3-ion (blue) QPs. Figures have been taken from Ref. [207].

tial of the quasiparticle simultaneously change their values in a jump-like manner as well.

Fig. 4.1(a) visualizes motion during a typical simulation. Corresponding to the trajectories of single ions in the channel (black and grey traces), one observes the centre-of-mass dynamics according to Eq. (4.6) (red). Ionic diffusion results in the corresponding diffusion of the quasiparticle. At approximately 0.5ns after the initial time, one of three ions escapes from the channel which results in the QP abruptly jumping to a new position. Diffusion of the ion at the boundary back and forth for some time gives rise to a series of jumps of the QP. These jumps cease once the ion finally leaves the neighbourhood of the channel and travels further

into one of reservoirs.

The correlation coefficients between coordinates are found to be within $[0.75, 0, 85]$. These high values confirm that the strong ion-ion interaction results in high correlation between the individual ions and their centre of mass, the quasiparticle.

Fig. 4.1(b) represents Eq. (4.7) for the QP's coordinates immediately before and after a jump. Depending on the side of the entry/exit, the positions of the QP before and after form two parallel lines. The non-uniform distribution of original and final positions is due to the presence of interactions, and their centroids define which transition occurs. For instance, a 3-ion quasiparticle resides in two more probable positions (maxima of distributions in (c-d)). This means that the three ions are located closer to the inner side of the channel, and one would expect the innermost ion to leave the channel. This does happen (transition $3 \to 2$, red square), with the QP relocating to the centre.

We also note that in the KcsA selectivity filter K^+ ions reside at the binding sites formed by carbonyl oxygen atoms [19]. Strong interactions with the latter define the localization of individual ions very precisely [31, 124, 245]. The exact localization of individual ions results in a much sharper, almost discrete, distribution of quasiparticles during permeation.

4.2.3 Coupling PMF $W_N(\mathbf{r}_1, \mathbf{r}_2, \dots)$ to the effective potential U^{eff}

Equation (4.6) describes the dynamics of the position q of the quasiparticle, but still contains ion-ion distances $\mathbf{p}$. To simplify Eqs. (4.6) further, the underlying properties of interactions in the channel must be discussed. Due to the strong interaction between ions, the relative distances p_m reach their equilibrium values rapidly, while the centre of mass moves adiabatically [144]. This allows one to introduce the equilibrium distribution of mutual distances $\mathbf{p}$, in terms of the position

q_N of the QP,

$$\bar{f}(q_N, \{p_k\}) = \frac{e^{-W_N(q_N,\mathbf{p})/k_BT}}{\int\cdots\int e^{-W_N(q_N,\mathbf{p})/k_BT} \prod_{m=1}^{N-1} \mathrm{d}p_m}. \tag{4.8}$$

Utilizing the equilibrium property (4.8), we multiply both sides of Eq. (4.6) by the distribution function (4.8) and integrate over all $\{p_k\}$. We also rewrite Eq. (4.4) in overdamped form. This yields the Langevin equation for the expected position of the quasiparticle $\langle q \rangle$

$$\langle \dot{q}_N \rangle = \frac{D_N^*}{k_BT} F_N^{eff} + \sqrt{2D_N^*}\xi(t) \tag{4.9}$$

with

$$F_N^{eff} = -\frac{\mathrm{d}U_N^{eff}}{\mathrm{d}q} = -\int \frac{\partial W_N(q_N, \mathbf{p})}{\partial q_N}\ \bar{f}_N(q_N, \mathbf{p}) \prod_{m=1}^{N-1} \mathrm{d}p_m. \tag{4.10}$$

In the integral above one has to ensure that the coordinates of individual ions $x_k(q, \mathbf{p})$ lie inside the channel.

Equation (4.10) is the main result of this Chapter. It explicitly couples the PMF W_N and the effective potential U_N^{eff} for a quasiparticle whose dynamics evolves according to Eq. (4.9). Thus, the notion of quasiparticles reduces the many-body problem (3.1) to effective one-body motion. Moreover, the coupling with MD by means of a PMF allows one to introduce atomistic details of the channel structure. The corresponding probabilistic description, given by the coupled differential Chapman-Kolmogorov equations, is a matter for future study.

4.2.4 Simplifying assumptions for BD modelling

In order to verify the applicability of Eq. (4.10), we run Brownian dynamics simulations in the toy model of ion-ion and ion-channel interactions proposed in Ref. [144]. This model envisages N ions interacting with each other and with the channel,

the energy PMF of the system being given by

$$W_N = \sum_{m=1}^{N} \Big[U(z_m) + \sum_{k>m}^{N} V(|\mathbf{r}_m - \mathbf{r}_k|) \Big]. \tag{4.11}$$

The energy comprises the ion-channel interaction

$$U(z) = -U_0 \; e^{-(z/a)^2} \tag{4.12}$$

and the ion-ion potential

$$V(r) = \frac{c_1 c_2 e^{-r/d}}{4\pi\epsilon_0 \epsilon r} + \frac{F_0 r_0}{9} \Big(\frac{r_0}{r} \Big)^9, \tag{4.13}$$

where the first term represents the screened Coulomb interaction [144] with shielding constant d and dielectric permittivity ϵ, and ionic charge c, while last term includes short-range repulsion between ions at small distance [78]. The parameters take the following values: $a = 9$Å, $d = 2.8$Å, $U_0 = 10.5 k_B T$, $F_0 = 2 \times 10^{-10}$N, $r_0 = 2.8$Å, $\epsilon = 1$ inside the channel and $\epsilon = 80$ in the bulk, $D = 2 \times 10^{-9}\mathrm{m}^2/\mathrm{s}$. We consider the case of zero applied electrostatic field.

The force Eq. (4.10) acting on the QP reduces to

$$F_N^{eff}(q_N) = -\int \frac{\partial U(z_m(q_N, \mathbf{p}))}{\partial q_N} \; \bar{f}(q_N, \mathbf{p}) \; \mathrm{d}\mathbf{p}. \tag{4.14}$$

The toy model (4.11) simplifies the comparison of the analytical calculations Eq. (4.14) with the PMF W_N computed [121] in simulations from the equilibrium distributions P_N via

$$W_N = -k_B T \log P_N + W_{off} \tag{4.15}$$

up to an arbitrary offsetting constant W_{off}. We consider explicitly the two distinct PMFs corresponding to when there are either 2 or 3 individual K^+ ions in the channel.

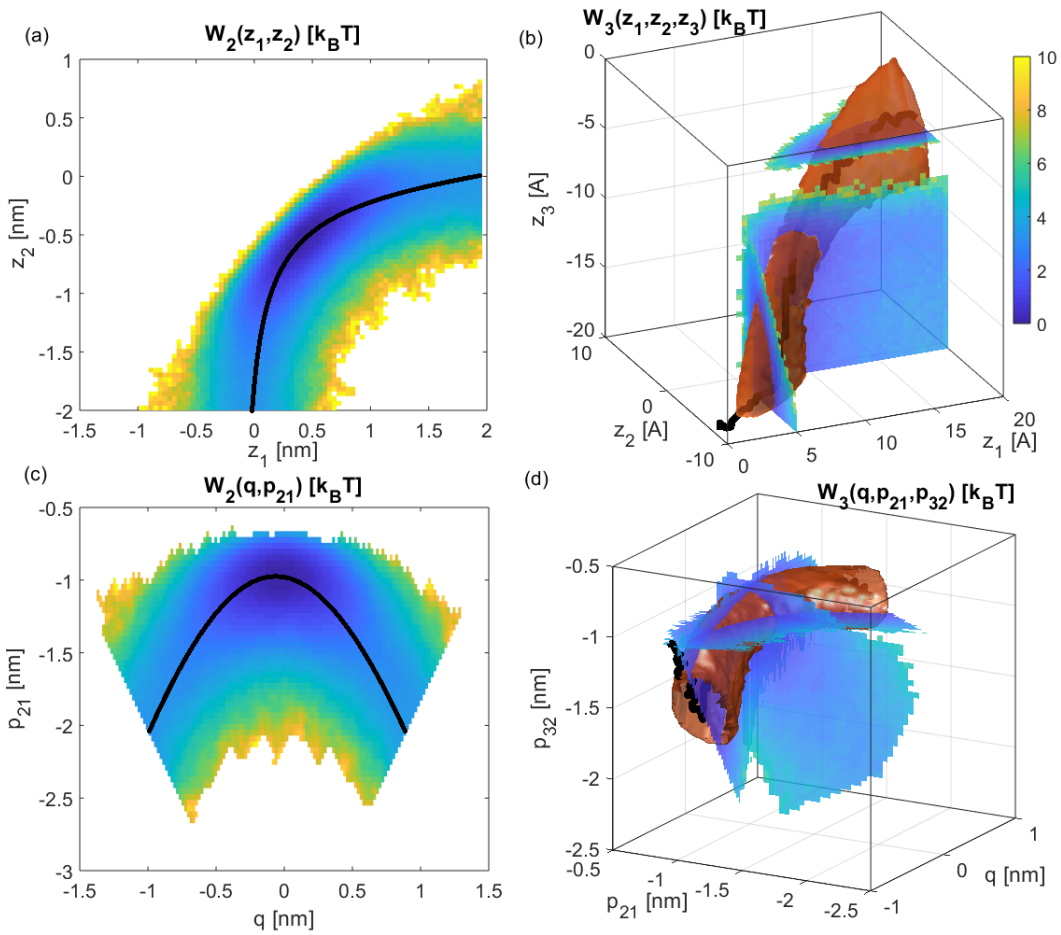

Figure 4.2: Two-dimensional (left column) and three-dimensional (right column) PMFs W_N, derived from BD simulations, represented in terms of the coordinates of individual ions (top row) and quasiparticles (bottom row), the significance of the colours being indicated by the colorbar. Slices of 3D PMFs are shown. Orange sleeves trace the surface of constant potential energy $1k_BT$. The permeation paths are indicated by black lines. Figures have been taken from Ref. [207].

4.3 Simulation results

In order to calculate the effective potential from Eq. 4.10, one has to transform the coordinates $\{z_m\} \to \{q_N, \mathbf{p}\}$ and thus derive $W_N(q_N, \mathbf{p})$. This method becomes attractive in the light of modern front-end studies of nanodevices which rely heavily on MD. Thus, PMF maps for many nanoscale systems have already been built.

On the top row of Fig. 4.2 we illustrate the PMFs of Eq.(4.11), obtained from BD simulations for two (a,b) and three (c,d) ions. Between jumps, ions move along the permeation pathway (shown by a solid black line). For instance, considering a two-ion case, an entering ion pushes its neighbour, so that the latter eventually

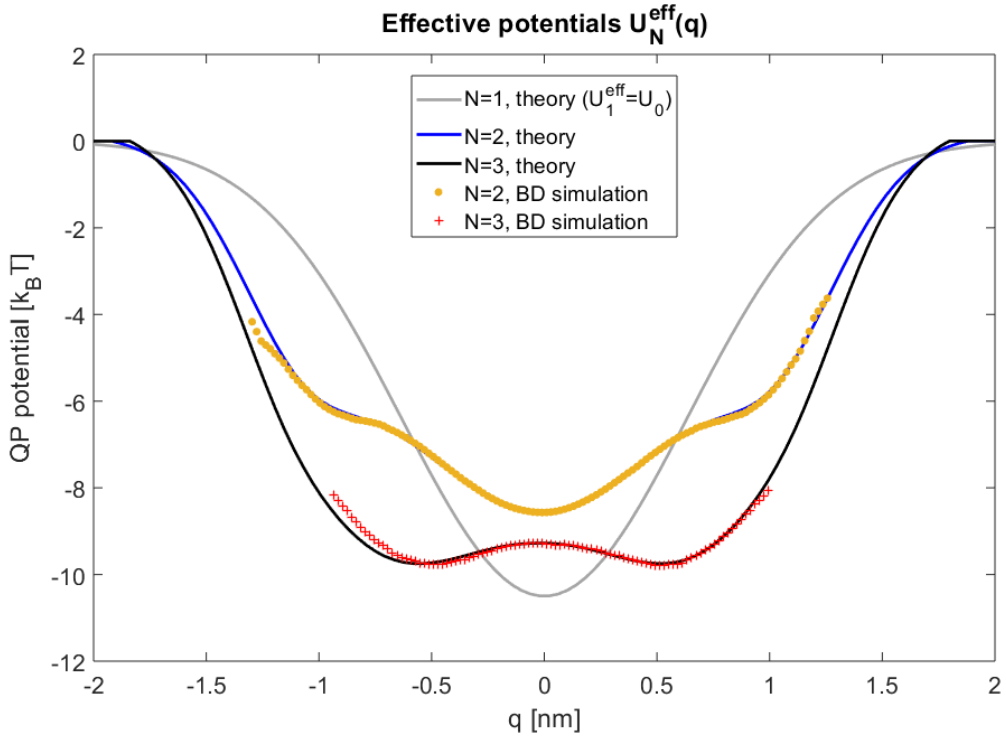

Figure 4.3: The effective potential U_N^{eff} calculated from the BD simulations using Eq. (4.10) (dots and crosses), and theoretically via Eq. (4.14) (solid lines), for the quasiparticles consisting of 1, 2, and 3 individual ions. U_1^{eff} (solid grey line) coincides with U_0 in Eq. (4.12). This diagram demonstrates how the multi-ion PMFs W_N, shown in Fig. 4.2, produce the 1D effective potential of the quasiparticle using formula (4.10). Figure has been taken from Ref. [207].

leaves the channel. Theoretical and simulation predictions match well (not shown), as they do in Figs. 1-2 of Ref. [241].

Under the coordinate transformation Eq. (4.2), the PMFs from the top row in Fig. 4.2 are transformed into the PMFs of a quasiparticle, bottom row. The two-ion permeation process outlined above can now be reinterpreted in terms of permeation by a quasiparticle. Following the path on Fig. 4.2(c), one finds that the distance between ions decreases, passes through a minimum and then increases again, being accompanied by the overall displacement of the QP to the right. The spatial displacement of the QP eventually leads to charge translocation through the filter, i.e. to the electric current.

Finally, we compute the effective potentials U_N^{eff}. As shown in Fig. 4.3, the implementation of formula (4.10) shows very good agreement between BD simulations and the theoretical predictions Eq. (4.14). One can see that the 2-ion

effective potential (solid blue line) inherits the minimum from the 1-ion potential well U_0 (solid grey line), but becomes shallower and wider. This occurs due to the repulsive interactions which increase the ion-ion distances. Furthermore, the 3-ion effective potential (solid black line) become even wider and gains two local minima located around ±0.7nm. The increased width of the effective potential and its flatness imply that the QP is less localized. This energy landscape thus defines the spatial range over which the charge is transferred during a permeation event.

4.4 Correlations between ion and the QP

The transformation of one QP into another, and consequently ionic transport through the channel, is associated with an outermost ion leaving or entering the channel [22]. With this in mind, we first discuss the distributions of single ions in the channel, and then elucidate their transition dynamics depending on the position of the QP.

Figure 4.4 shows the distribution of 1, 2, and 3 ions inside the pore. For 1 ion, this is given by the Boltzmann distribution $P \sim e^{-U(q)/k_BT}$ as in this case the ion and quasiparticle coincide. When two ions occupy the pore the ion-ion repulsion creates a two-headed distribution at approximately ±0.5nm. With three occupying ions, the outermost ion gains the freedom to reach the edge of the pore and eventually leaves it.

The probabilities of each occupancy state are shown by the inset. The pore primarily accommodates 1 - 3 ions, with a negligible chance of a 4-th ion entering. This occupancy distribution in fact represents the probability to find each individual QP inside the pore. Switching from one QP to another suggests an ion leaving or entering the channel, and thus produces ionic current – the main experimental observable. For a better understanding let us consider the individual ions' trajectories and these of the QPs.

The transition processes describing either an ion entering the pore from the

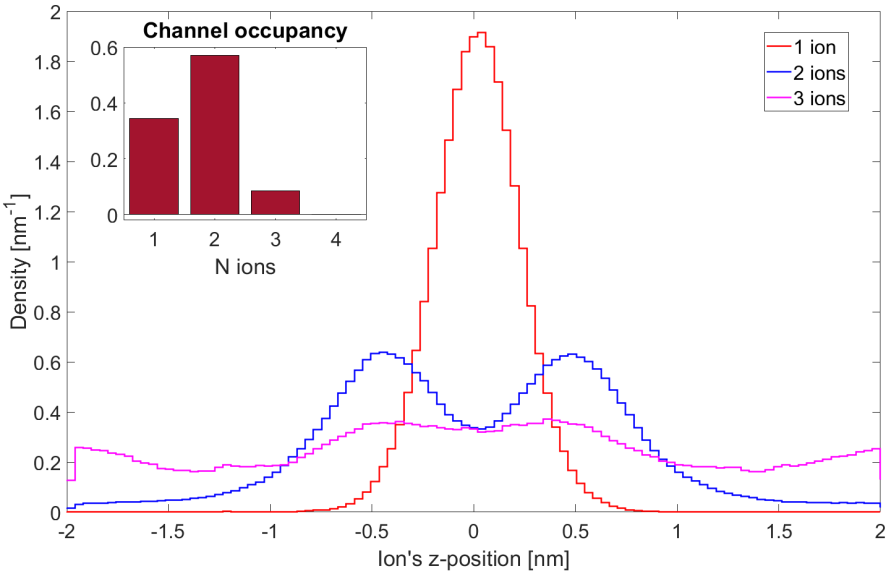

Figure 4.4: Distribution of 1, 2, and 3 ions inside the pore. The inset displays the probability of each occupancy state. Figure has been taken from Ref. [242].

bulk, or exiting from the pore, need further clarification. With that in mind, we introduce a cylinder of radius and height 5-Å at each end of the channel, representing the channel's mouths. Thus the dynamics of the entering and leaving processes can be monitored. The inset of Fig. 4.5 shows the distribution of residence times (identically, of the *cis* trajectories [161]), showing how long on average an ion stays in the mouth. Here, the *trans* trajectory corresponds to an ions crossing the channel, and the *cis* trajectory describes the ion approaching and leaving the channel from the same side without crossing the channel.

However, these times should also depend on the location of the QP. To provide some preliminary insight into this question, we fix a pair of ions at a 2nm separation inside the channel and analyse the corresponding changes in the distribution near the pore's edges. This mimics the ionic configuration at a specific position of the QP analogous to Fig. 4.4. For clarity, we consider three values of $q_2 = \{-0.5,\ 0,\ 0.5\}$nm. Eventually, the number density of K^+ ions in the mouths and the channel is measured.

One can see that once the QP is localised closer to the left (right) edge of the channel, ions do not enter the channel from that side, but penetrate from the "free" right (left) mouths of the channel. If the QP is at the centre of the pore

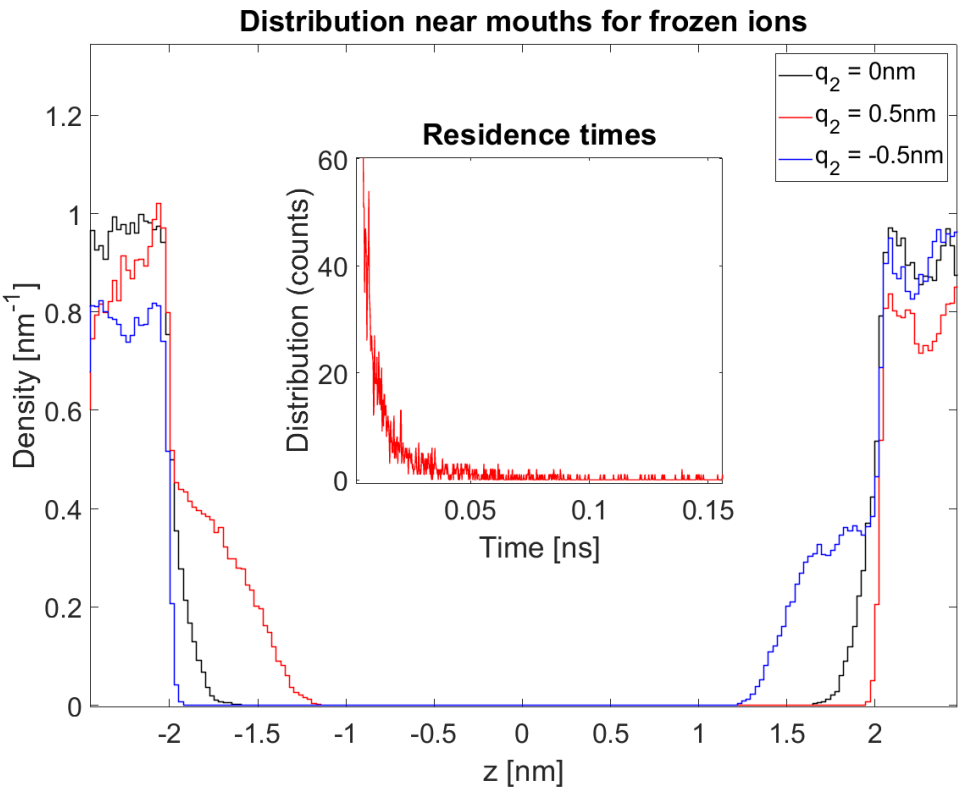

Figure 4.5: Distribution of the mobile ions in the channel and the mouths when a pair of ions in the pore is kept immobile. Thus the QP's location q_2 is fixed. Inset: distribution of the residence times in the mouth. Figure has been taken from Ref. [242].

then it provides an equal probability of entrance by an ion from either mouth. The increased distribution in the channel or near the mouths suggests an increased probability of entry, and therefore higher probability of permeation.

These findings can be understood in light of the screened Coulomb interaction Eq. (4.13) between the ions. Thus, the bulk ions can be influenced by ions in the channel at a finite distance ($\sim d$ in our simulations).

This interactions between bulk and channel ions define which transition occurs. If the QP approaches the edge of the pore it prevents an ion entering from the bulk on this side but allows an ion to enter on the opposite side. When an ion enters, it pushes the remaining ions such that the outermost ion leaves the channel (knock-on conduction). This is an example of a *trans* trajectory [161, 246].

These transitions are vital to understanding the channel's permeation mechanism. One often assumes non-interacting ions moving in a mean field [138,154,182],

based on the unconditional probability densities [153,246]. However, this approach evidently ignores the correlations between ions emerging from their interaction. A more sophisticated analysis requires the use of conditional probability densities [153] that are closely related to the pair-distribution functions [153]. This improved description of the transition process under arbitrary experimental conditions – voltage, concentrations, and chemical composition [15] – can thus pave the way to a more adequate definition of the transition rates in the kinetic [42,176,182] theories.

4.5 Summary

We have derived the effective potential of a quasiparticle [144] from the potential of the mean force [91]. The notion of quasiparticles allows one to reduce the collective motion of strongly interacting ions to the motion of a single particle in this effective potential. The inclusion of the PMF couples the effective potential with the energy landscape created by all ions, water molecules, ligands and the X-ray structure of the channel. Application of the derived relation, demonstrated to an analytical toy model of interactions in the KcsA channel, enabled comparison of separate 2- and 3-ion analytical PMFs with those obtained from Brownian dynamics simulations, and thus simplified the comparison between theory and simulations. The method has direct application to modern molecular dynamics studies of nanoscale systems, in which PMFs are the primary targets for study of permeation mechanisms.

It was shown that during permeation a quasiparticle undergoes both diffusion and discrete jumps in space, motion leading to the electric current – the major experimental observable. We show that the motion of the bulk ions in the mouths and the transitions between different QPs are correlated. Namely, the presence of the QP near one of the channel's edges suggests a higher exit probability from that edge and a higher entry probability on the opposite side. This appears important to kinetic and rate theories where the transition process is the key to successive description of conduction and selectivity.

Thus, the notion of the quasiparticle couples the molecular dynamical calculations with the experimentally measured current-voltage and current-concentration characteristics of the channel. It connects the atomic structure, the multi-scale theoretical methods and eventually leads to experimentally verifiable predictions.

Further work may include BD simulations incorporating MD-generated PMFs in e.g. the real KcsA channel [31,124]. It will be important to see how the K^+/Na^+ selectivity is reflected in the properties of the quasiparticle. Another direction of possible development is the establishment of connection with continuous methods. This suggests writing a set of coupled differential Chapman-Kolmogorov (DCK) equations for each separate occupancy state, describing diffusion and transitions of particles between states. Integration of the set of coupled DCK equations along the channel axis would provide a further link to the kinetic rate theory [176].

5. Using RDFs to quantify hydration

"The aim of science is to make difficult things understandable in a simpler way..."

P.A.M. Dirac

As discussed in the Introduction chapter 1, the ionic potential during permeation affects the conduction and selectivity of a biological ion channel. The potentials of the mean force (PMFs), representing these potentials, contain a large energy contribution arising from the ion's solvation by individual water molecules. In this Chapter, we consider a graphene pore as a simple analogue of a biological ion channel, in an attempt to decompose the PMF into a series of analytically tractable terms. In doing so, we propose a novel method of calculating the dehydration energy by means of the concept of a radial density function (RDF). This method introduces the atomic-level information of the ion-solvent interactions, and hence goes beyond the recent modification of the Born formula [158, 247].

5.1 Introduction

Several models exist to describe ionic hydration. The basic estimation is given by the Born formula which calculates the difference in the energy of the electrostatic

fields, created by a single ion of radius R, in two dielectrics (see Appendix B for the detailed derivation). This model assumes continuous isotropic dielectric solvent. Considering a dielectric and vacuum, the Born formula reads as

$$\Delta G_{dehydr} = \Big(\frac{1}{\epsilon} - 1\Big)\frac{(Ze)^2}{4\pi\epsilon_0 R} \tag{5.1}$$

The more advanced models generalize the Born formula by accounting for the size of each ionic species present [248–250].

Recently, Zwolak and co-workers [1,158,247,251] introduced a shell model based on the Born formula. The authors first assume the hydration cloud to consist of a number of spherical layers according to the minima of the ion-water RDF. Each of these layers is assumed to carry a specific amount of energy estimated by means of the Born's idea [158, 247]

$$\Delta G^i_{dehydr} = \Big(\frac{1}{\epsilon} - 1\Big)\frac{(Ze)^2}{4\pi\epsilon_0}\Big(\frac{1}{R^O} - \frac{1}{R^I}\Big) \tag{5.2}$$

where R^I and R^O stand for the inner and outer shell radii, respectively.

The second assumption states that when an ion enters a nanopore, the dehydration barrier is given by the spherical surface area removed during dehydration from each layer. Using geometrical estimations, Zwolak *et al.* estimate the fraction of the removed area as [158, 247]

$$1 - f_i = \sqrt{1 - \Big(\frac{R_p}{R_i}\Big)^2} \tag{5.3}$$

Here R_p is the pore's radius and R_i is the radius of each spherical layer. Thus, the total dehydration barrier suggests the summation of the contributions from all layers [158, 247]

$$\Delta G = \sum_i \Delta G^i_{dehydr}(1 - f_i). \tag{5.4}$$

One of the difficulties of the Born approximation in general, and consequently Zwolak's model, is the choice of the ion's radius. On the nanoscale, this quantity

is poorly defined [121] and can change in different solutions [252, 253]. Another difficulty is the treatment of water as a structureless continuum. These models approximate the solvent as a homogeneous isotropic dielectric. However, it is known that the solvent molecules near an ion are distributed unevenly [110] as governed by the radial density function (RDF) (see Fig. 5.2). The latter can be measured in X-ray and neutron scattering experiments, as well as Monte-Carlo and molecular dynamics simulations [110, 218]. Water distributions are routinely measured in artificial nanopores and nanotubes [254–256].

Here, we utilize the RDF to describe, at least qualitatively, the water distribution near a graphene pore and an ion near the pore entrance. We also provide an approximation for the solvation contribution to a single-ion PMF when the ion traverses the graphene pore, and provide preliminary results for K^+ and Na^+ ions.

5.2 Theory

The system comprises fixed graphene atoms in a hexagonal lattice, an ion (for definiteness we assume K^+ although this is equally applicable to other ions), and a water box (Fig. 5.1). A hole in the lattice was created by removing one hexagon of carbon atoms in the centre.

Assuming additivity of pairwise interactions, the energy of a water molecule in the field created by the graphene atoms and the ion is given by

$$W(\mathbf{r}) = W_{I-W}(\mathbf{r} - \mathbf{r^{ion}}) + \sum_{n}^{N_C} W_{C-W}(\mathbf{r} - \mathbf{r_n^C}) + \sum_{m}^{N_w-1} W_{W-W}(\mathbf{r} - \mathbf{r_m^W}). \quad (5.5)$$

Here W_{I-W} stands for the ion-water, W_{C-W} represents the carbon-water, and W_{W-W} introduces the water-water interactions. N_C and N_w are the numbers of carbon atoms and water molecules, respectively. It is worth noting that the interactions of a water molecule with an ion or a carbon atom depend on the water model [257], and ultimately should include the distance to and the orientation of the water molecule. For simplicity these contributions are implied in W_{I-W} and

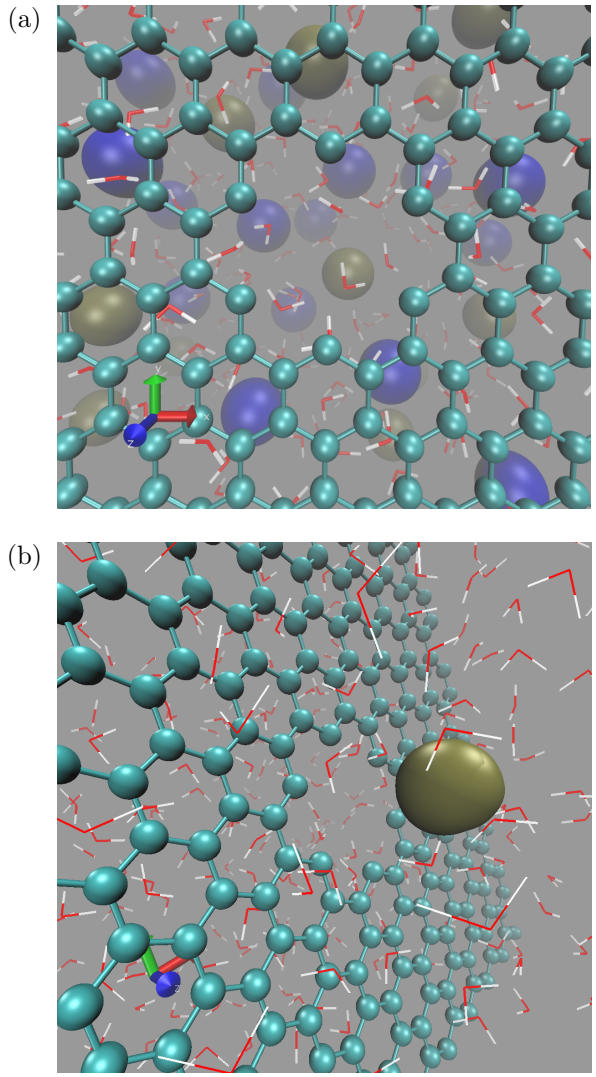

Figure 5.1: MD setup to study the spatial distribution of water molecules. (a) The hole in the graphene layer. Graphene lattice is shown in cyan, water molecules are represented by red-and-white triangles, K^+ and Cl^- are shown by golden and blue spheres, respectively. (b) A K^+ ion at the entrance to the pore.

W_{C-W}.

Direct application of the above analytic formula does not appear feasible due to the large number of degrees of freedom. Instead, we construct an approximation using the concept of the radial density function (RDF). It is known that the potential of the mean force (PMF) $\mathcal{W}$ is rigorously related to the RDF $g(r)$ via [110, 218, 258]

$$\mathcal{W}(\mathbf{r}) = -k_B T \ln\left(g(\mathbf{r})\right). \tag{5.6}$$

This allows one to approximate the potential (5.5) via

$$W(\mathbf{r}) = \mathcal{W}_{I-W}(\mathbf{r} - \mathbf{r^{ion}}) + \sum_{n}^{N_C} \mathcal{W}_{C-W}(\mathbf{r} - \mathbf{r_n^C}). \tag{5.7}$$

Note that when using the PMF the interactions with water are already implicitly included.

Formula (5.7) assumes that the water spatial density $\rho(\mathbf{r})$ satisfies

$$\begin{aligned} \rho(\mathbf{r}) &= \rho\ g(\mathbf{r}) = \rho\ e^{-\mathcal{W}(\mathbf{r})/k_BT} \\ &= \rho\ e^{-\frac{1}{k_BT}\left[\mathcal{W}_{I-W}(\mathbf{r}-\mathbf{r^{ion}}) + \sum_n^{N_C} \mathcal{W}_{C-W}(\mathbf{r}-\mathbf{r_n^C})\right]} \\ &= \rho\ e^{-\mathcal{W}_{I-W}(\mathbf{r}-\mathbf{r^{ion}})/k_BT} \cdot \prod_{n}^{N_C} e^{-\mathcal{W}_{C-W}(\mathbf{r}-\mathbf{r_n^C})/k_BT}. \end{aligned} \tag{5.8}$$

Using the relations

$$g_{I-W}(\mathbf{r}) = e^{-\mathcal{W}_{I-W}/k_BT} \tag{5.9}$$

$$g_{C-W}(\mathbf{r}) = e^{-\mathcal{W}_{C-W}/k_BT} \tag{5.10}$$

between RDFs and PMFs, we rewrite expression (5.8) as

$$\frac{\rho(\mathbf{r})}{\rho} = g_{I-W}(\mathbf{r} - \mathbf{r^{ion}}) \cdot \prod_{n}^{N_C} g_{C-W}(\mathbf{r} - \mathbf{r_n^C}) \tag{5.11}$$

which is the first main result of this Chapter. It allows us to compute the density of water wetting a given set of atoms in terms of RDFs. This formula corresponds to the well-known Kirkwood superposition approximation [120]. It has also been generalized to describe the ice-water interface [259] or to include the 4-th order correlations [260]. Here, we for the first time apply this relation to describe the ion's solvation structure in artificial nanopores. The next step is to evaluate the solvation energy of an ion arbitrarily located in that system. It can be done as follows.

First, given the RDF, one can calculate the interaction energy of the ion with a

water molecule via Eq. (5.9). Collecting these interactions with all water molecules from the entire system, one arrives at

$$G = \rho \int_V u(\mathbf{r}) g(\mathbf{r}) \mathrm{d}\mathbf{r}. \tag{5.12}$$

This integral runs over the volume V occupied by water. In conjunction with Eq. (5.11), formula (5.12) represents the second important result of this Chapter. It provides a method to evaluate the ionic solvation energy at an arbitrary spatial point.

5.2.1 Decomposition of the PMF

Eq. (5.12) provides an analytical tool to calculate the PMF of a given ion for a pore of specified chemical composition. Indeed, the single-ion PMF in the pairwise limit can be decomposed according to [259]

$$W = \sum_{all\ FCs} \mathcal{W}_{I-FC} + \sum_{lattice} \mathcal{W}_{I-L} + \sum_{all\ waters} \mathcal{W}_{I-W}. \tag{5.13}$$

The energy contributions in this formula include the interactions of the ion with fixed charges $\mathcal{W}_{I-FC}$, lattice atoms $\mathcal{W}_{I-L}$, and water molecules $\mathcal{W}_{I-W}$ (hydration); spatial coordinates are omitted for clarity. The interaction with the fixed charge can be approximated via e.g. the screened Coulomb law (3.6). The form of the interaction with the lattice can be taken directly from a molecular dynamics force field [110].

Formula (5.12) can be adapted to any lattice and any ion type. The RDFs can be measured experimentally in X-Ray studies, evaluated via the RISM theory or Kirkwood-Buff theory, or measured in MD simulation [110, 261, 262]. Thus, one can consider the difference in the sieving ability without running a heavy-duty MD simulation. Equation (5.13) can be applied to study the selectivity by e.g. MoS_2 or graphene nanopores for the same ionic species, or to consider how well does the graphene pore selects between different ionic species. We have made preliminary

analyses of K^+/Na^+ selectivity by an uncharged nanopore in the Results section.

5.3 Simulation results

The MD simulation details can be summarized as follows. We used VMD [58] to build the system, and NAMD [263] with a CHARMM27 force field for molecular dynamics simulations at $T = 300$K with the time step 0.5fs and the velocity Verlet algorithm. The TIP3P [264] water model was used. All carbon atoms were fixed by setting the `beta` parameter to 1. The system first undergoes equilibration during the initial 1000 steps in the Nosé-Hoover thermostat at pressure $p = 1$ atm, with the remaining simulation running under the NVT conditions. No electric field is applied. The production runs took 5 ns to yield statistically significant numbers.

Trajectories are further read by an `MDTools` script in MATLAB [265], and further analysed by a home made script to generate the distributions. RDFs were measured for a free atom (C or K^+) in water surroundings. When the K^+ RDF was measured, another free Cl^- ion was added to neutralize the system. Finally, RDFs were measured using the VMD plugin `gofr`.

5.3.1 Water density

The first step towards predicting the water structure is to describe the water distribution near the pore (Fig. 5.1a). First, we run a separate MD simulation to measure the RDFs for water-ion and water-carbon pairs. The results are shown in Fig. 5.2(a) and (b) with the corresponding PMFs (5.9) given in (c) and (d). Due to the electric interaction between the ion and the negative oxygen of a water molecule, one observes a highly pronounced peak at $r \approx 2.7\mathring{A}$. The water-carbon interaction does not involve electric interactions and is therefore not so emphasised. Both distributions tend to 1 as $r \to \infty$ as expected from theory [110]. These RDFs agree well with published data [266].

Next, we added a honeycomb lattice of fixed carbon atoms in the XY plane of

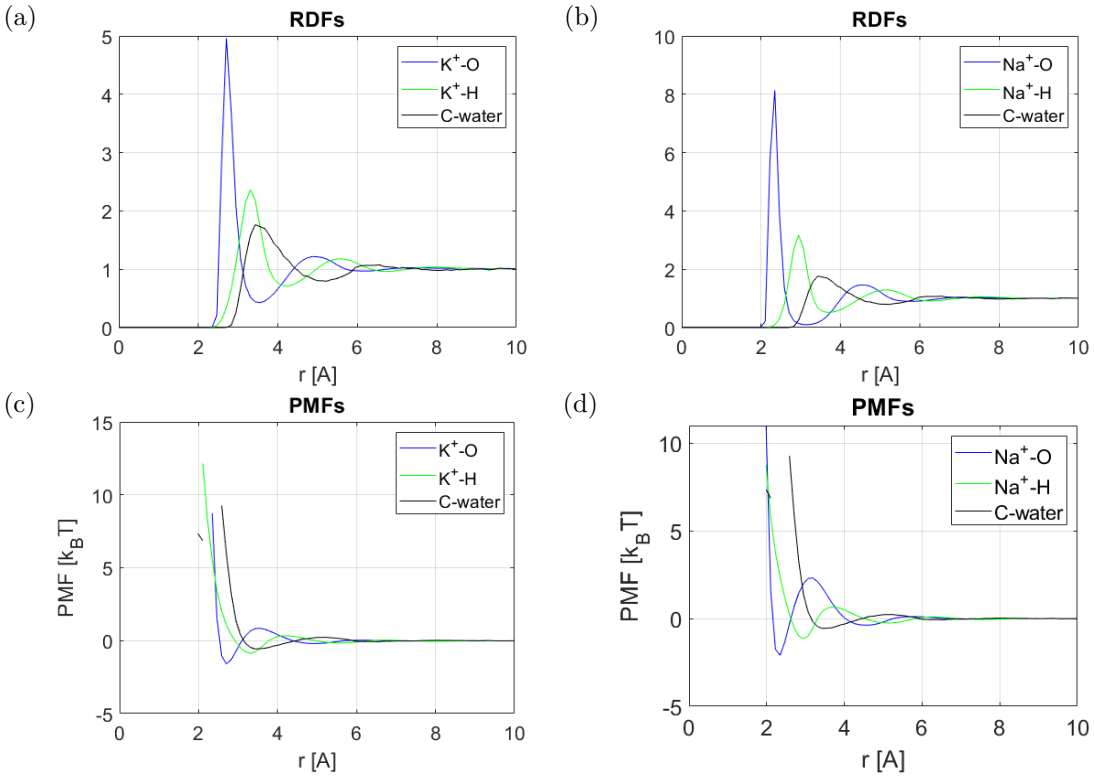

Figure 5.2: Radial density functions (RDFs) for (a) K^+ and (b) Na^+. RDFs for ion–O^- (blue), ion–H^+ (cyan), and C–O^- (black), measured for unrestrained atoms in water. Potentials of the mean force (PMFs) corresponding to the ion–O^- (blue), ion–H^+ (cyan), and C–O^- (black) interactions. The PMFs for (c) K^+ and (d) Na^+ are calculated from the corresponding RDFs via Eq. (5.9).

the simulation box. A pore was made by cutting out a hexagon of carbon atoms near the centre of the graphene sheet (Fig. 5.1). MD density profiles are shown in Fig. 5.3(a). One can see the water structure near the graphene wall and the pore. Water molecules form layers in the axial direction. This pattern is reproduced by means of Eq. (5.11) on Fig. 5.3. This inhomogeneous distribution represents one of the limitations of the Born formula (5.1).

After averaging over angles, the water density profile is shown by the blue distribution in Fig. 5.4. Although the dips and peaks of the two curves match, their amplitudes are actually different. This is expected as the RDF represents the density in a 3D sphere while the axial density implies cylindrical geometry. In the latter, for instance, each water molecule interacts with more carbon atoms compared to a free bulk.

The second test suggested adding an ion to the system. Two configurations

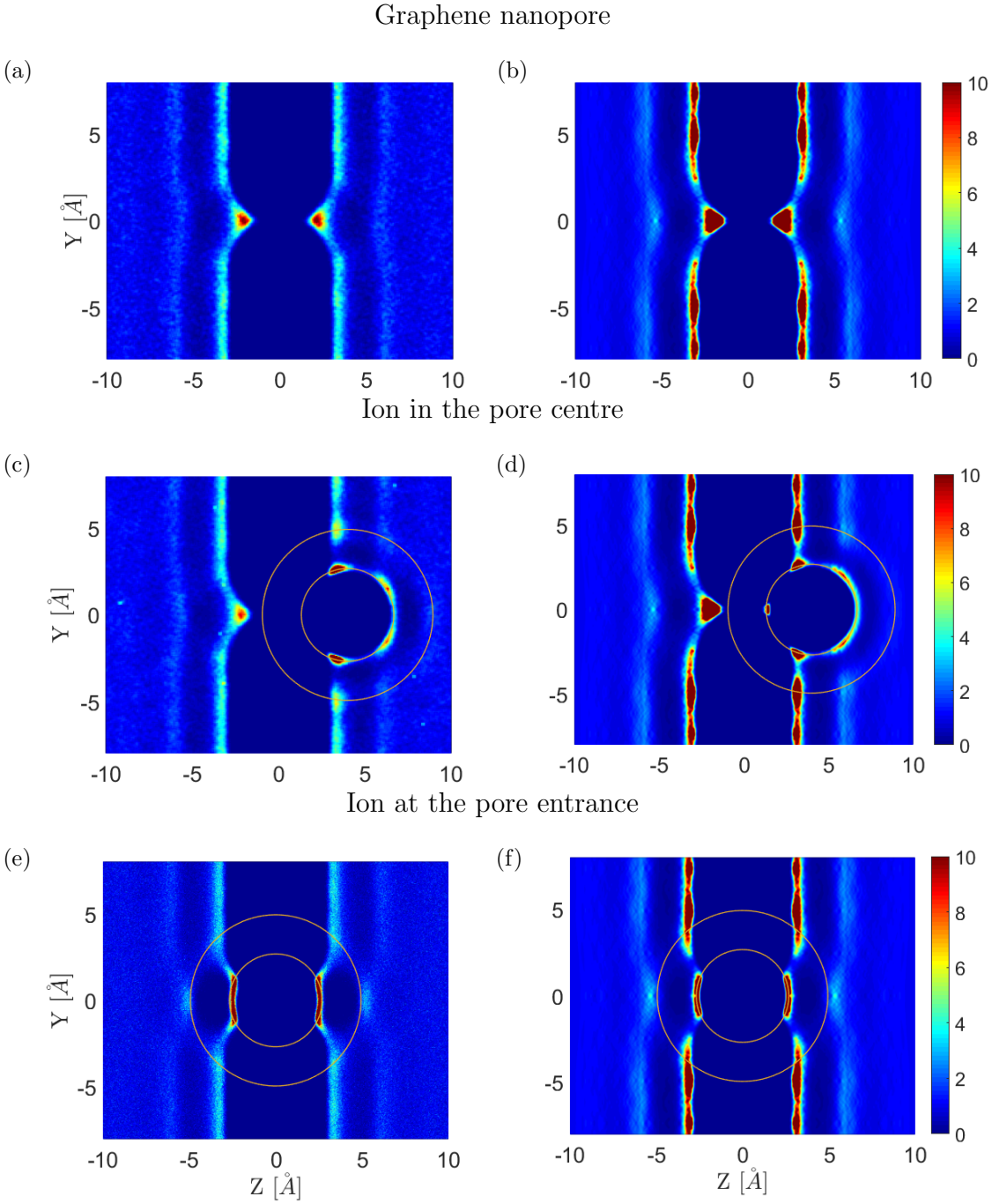

Figure 5.3: Water distribution near a graphene wall for (a, b) the bare pore, (c, d) a K^+ ion in the pore centre, and (e, f) a K^+ ion away from the pore. (a, c, e) Water distribution, all-atom MD simulation. (b, d, f) Superposition of RDFs, analytic Eq. (5.11). One can see that the qualitative structure of the water distribution (ridges and valleys, islands of high and low density) is reproduced well. At the same time, there is a numerical difference between the simulation results and the theoretical predictions. The orange concentric circles represent the maxima the intact hydration shells, corresponding to the RDFs in Fig. 5.2a, and are given as a guide for the eye.

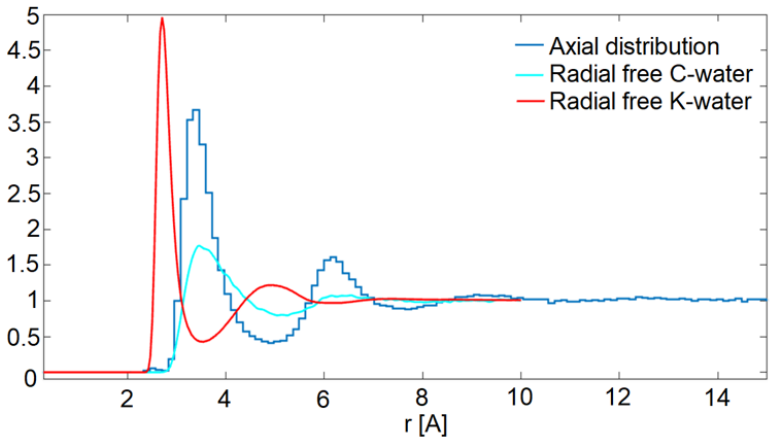

Figure 5.4: Axial distribution of water molecules in an MD simulation (blue) matches the peaks and lows of the carbon-water RDF (cyan), although it reveals different numerical values. This discrepancy is expected to emerge from the difference in geometries: cylindrical in the first case *vs.* spherical in the latter. The potassium-water RDF (red) is given for comparison.

were considered: the ion located exactly in the middle of the pore, and 4Å away from the pore centre. For simplicity, ions were frozen at their respective locations, i.e. the ionic coordinates did not change in time. The results of measured distributions are shown in Fig. 5.3(c-f). The change of water structure is obvious. The attraction between positive K^+ ion and negative water oxygens leads to highly populated areas at the pore entrances. Interestingly, these areas are separated by "islands" very seldom visited by water molecules. Finally, when an ion is dislocated at the pore entrance, the water distribution clearly represents a superposition of two contributions: planar density oscillations from the wall and circular oscillations from the ions [267]. All the above effects are readily reproduced by our method (Fig. 5.3(d)).

It is expected these structural effects can manifest themselves indirectly in experimental studies. The properties of the water structure near the pore and in free bulk differ, and this difference should be revealed in the terahertz spectrum [268]. Water dipoles also have a preferred orientation near the pore and the ion, which significantly reduces the dielectric constant and thus can be verified via scanning dielectric microscopy [214]; although, this task at the sub-nanometer scale involves significant experimental challenges. The alteration of the vibrational properties of

water molecules near the pore and/or the ion should produce noticeable fingerprints in two-dimensional infrared spectra, similar to the ones reported for two alternative permeation mechanisms in the biological KcsA channel [67].

5.3.2 Profile of the solvation energy

We have also undertaken preliminary estimations of the PMF using our approach by means of formula (5.12). Only the ion-water interactions were considered in order to focus on the hydration contributions. Figure 5.5(a) shows the hydration

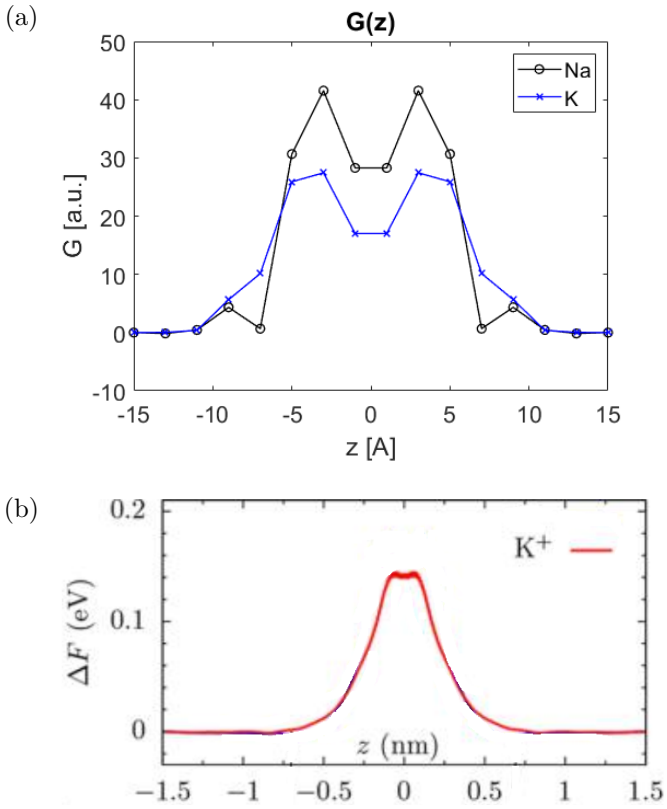

Figure 5.5: (a) Preliminary estimations of the desolvation profiles by means of Eq. (5.12). The difference between K^+ and Na^+ profiles gives rise to the K^+ over Na^+ selectivity. (b) K^+ PMFs obtained in a MD simulation [1] for a slightly different geometry of the graphene nanopore. Adapted with permission from Ref. [1]. Copyright (2017) American Chemical Society.

profiles (in arbitrary units), computed via Eq. (5.12). According to the difference in RDFs, and consequently PMFs, of K^+ and Na^+ ions as shown in Fig. 5.5, smaller Na^+ ions interact more strongly with the surrounding water molecules. This gives rise to a higher desolvation barrier seen in panel (a). In other words,

this graphene pore is K^+-selective, which agrees with literature [85]. For comparison, we show the PMF from an uncharged graphene pore Fig. 5.5(b) [1] which is contains a $\sim 5k_BT$ energy barrier. The barrier for Na^+, according to *ab initio* MD [269], is higher and may vary within 8-54 k_BT. Both profiles reveal a qualitatively similar shape, the quantitative differences being attributed to the structural difference between the pores' geometries and the preliminary nature of the calculations. Nevertheless, the profile, obtained via Eq. (5.12), can be rescaled by the peak value for the dehydration barrier, Fig. 5.5(b), and be further included into the Nernst-Planck equation (2.5) to analytically evaluate the ionic current through the given nanopore.

5.4 Discussion

In contrast to the Born approximation and its amended versions [247, 248], our method does not require the inclusion of the ionic radii – a parameter which is vaguely defined on the nanoscale [122] and may vary in different solvents [252,253]. We have illustrated, both by an MD simulation and by calculation, that the water density is inhomogeneous near the nanopore thus breaching one of the assumptions behind the Born approximation. The RDFs can be obtained experimentally in X-ray or neutron scattering studies [110], RISM [261], or in a separate MD simulation, and thus the interaction between arbitrary ionic species (e.g. K^+ or Na^+), solvent (e.g. H_2O or D_2O) and lattice configuration (MoS_2, graphene etc.) can be incorporated.

The method can be improved in a number of ways. First, the currently static lattice of atoms and the ion should instead undergo thermal fluctuations around their corresponding locations according to the molecular forces. A Taylor expansion of the potential energy up to the quadratic term should provide for the analytically tractable approximation. Secondly, the orientation of water molecules, especially in the vicinity of the nanopore, should be considered. It has recently been demonstrated that the orientation of water molecules affects the forces ex-

erted on the entering ion, which in turn affects the pore's transport properties [270]. Doing so suggests the inclusion of the water-water interactions, in contrast to the current coarse-grained treatment of the water molecule implied by the RDF. The orientation and motility of solvent molecules is known to contribute to dielectric permittivity [271], which is a vital input to calculate the electrostatic field inside the pore [161]. Finally, it is reasonable to generalize our method to account for the 3D cloud of solvent or ligand molecules [44] instead of using the spherically symmetrical approximation. This can be done with the help of spherical harmonics, and appears essential to quantify the ion-ligand interaction inside the nanopore. As already discussed (see Chapter 1), the later interaction is the key to the nanopore's selectivity.

5.5 Summary

The properties of biological nanopores are most comprehensively given by a potential of the mean force (PMF), which quantifies how an ion interacts with other ions, the pore and surrounding water. The interplay between the two latter components defines the selectivity of a pore. Efficient quantitative description, self-consistently accounting for the pore structure, atomic composition and ions in the pore, is hence vital for the prediction of ionic currents through mutated biological channels and the design of functionalized artificial nanopores.

In this Chapter, an analytical theory to describe water density Eq. (5.11) and a method to evaluate the solvation energy (5.12) of an ion in a water environment is presented. For the first time, that approach is applied to artificial graphene nanopores. The proposed method relies on the use of the 1D bulk radial density function (RDF) in estimating the water density near the nanopore, as well as it automatically accounts for the pore shape, type of atoms the lattice consists of, type of solvent, and the ion's location near the pore entrance. Thus, one becomes capable of describing water density and evaluating the solvation energy of an arbitrary ion in a nanopore made of arbitrary material, which appears of primary

importance in molecular modelling [262, p.38]. This method does not require heavy-duty MD simulations, and thus is expected to provide an efficient analytical tool predicting the conductive and selective properties of artificial nanopores from their atomic structure.

6. Concluding remarks

6.1 Summary

In brief, this thesis has presented:

- A review of the physiological properties of ion channels and artificial nanopores (see Chapter 1). This included a discussion of conductive and selective properties of the biological KcsA K^+ channel and artificial nanopores.

- A description and discussion of the experimental, computational and theoretical techniques to describe ion channels' properties (chapter 2), including detailed analysis of their strengths and weaknesses. It was concluded that the most promising combination is BD with a multi-ion MD-generated PMFs, because this allows one to combine the atomistic details and computational speed.

- A detailed description of the Brownian dynamics simulation technique (see Chapter 3), with specific focus on the selection of settings to reflect the key physical effects. A large number of tests was performed to validate the BD simulation. A "stitching" procedure, required when using a multi-ion PMF in a BD simulation, was proposed.

- A comparison of the computational efficiency, physical contribution and accompanying side effects of treating the domain boundaries in atomistic simulations. For simulations with a fixed number of particles, periodic, cyclic

or stochastic boundaries are the optimal choice. However, to simulate a system with a chemical gradient, the more computationally demanding GCMC routine should be used. The GCMC algorithm is most suitable in light of comparison with multi-variable electrophysiological experiments. The effect of the channel's walls still has to be considered to complement MD-generated PMFs inside the channel.

- A study of the quasiparticle's motion in a toy model of the KcsA channel (see Chapter 4). This included derivation of the equation of motion of the QP, the connection between the QP's effective potential and a multi-ion PMF, and the correlation between the QP and an entering/leaving ion.

- A method to describe the distribution of water surrounding an ion at the nanopore entrance in terms of the radial density function (RDF) (see Chapter 5). Using this distribution, one can evaluate the dehydration barrier and further provide an analytical decomposition of a single-ion PMF. Comparison between our method and MD simulations revealed good qualitative agreement for the water density and the PMF profiles.

6.2 Conclusions

Narrow biological ion channels demonstrate a wide range of phenomena — conduction, selectivity, blocking — due to the presence and interplay between the ion-ion, ion-water, ion-pore, and other interactions. A consistent and accurate description of this multi-faceted picture has become a long-lasting topic of theoretical and computational research. The ultimate aim of our research is to correctly predict a channel's properties starting from its atomically-resolved crystal structure.

The primary focus of the thesis was to describe the correlated motion of the ions adequately accounting for the atomic interactions, including the effect of the channel and other ions. The approach connected the genuine multi-ion potential of the mean force (PMFs) and the concept of quasiparticle, with further valida-

tion by virtue of Brownian dynamics simulations. In addition, we have proposed a method to analytically evaluate the dehydration barrier – one of the main components of the PMF determining ionic selectivity – thus improving the existing approach. It is believed the results will find application to other narrow channels and functionalised artificial nanotubes, where single-file conduction and ion-water interactions play key roles.

The main results of the thesis are listed and detailed below:

1. A significant development of the BD simulation procedure. It allows for arbitrary chemical composition of bulk solutions, arbitrary concentrations in bulks, transmembrane electrostatic potential and the inclusion of the MD-generated multi-ion PMFs. The latter allows one to maintain the speed of BD and exploit the atomistic accuracy of MD via an implicit inclusion of the channel's X-ray structure. We estimated the current-voltage and current concentration curves for a graphene nanopore and a toy model of the biological KcsA ion channel. We also undertook a comparison with the available experimental data for the KcsA channel, and found good qualitative agreement. The BD system can be further adapted to investigate selectivity, blocking, channel mutations, and the effect of pore fluctuations. Thus, this BD system allows one to connect the atomistic structure and the biophysical experiments with ion channels in natural environment under a wide range of experimental conditions.

2. We have derived a formula (4.10) connecting the multi-ion PMF and the effective potential for the QP. Using a toy model of the ion-channel and ion-ion interaction in the biological KcsA ion channel, excellent agreement between the BD simulation and the predictions of the formula has been demonstrated. The multi-ion PMF allows one to account self-consistently for the ion-ion, ion-water, ion-ligands and ion-pore interactions with atomic resolution. Thus, the concept of QP represents the fundamental importance for narrow ion channels with single-file conduction mechanism, as it connects

an arbitrary multi-ion atomic PMF with measurements in real biological ion channels.

3. A demonstration for the first time of the correlation between an ion, entering/leaving the channel, and the QP. It has been shown that when the QP is closer to the channel edge, ions are unlikely to enter. Conversely, the entrance probability increases when the QP is located far from the edge. These results provide an important insight into the dynamics of the ion's transition what proves an essential ingredient in the statistical and kinetic theories.

4. An analytical theory of ion dehydration in narrow pores was introduced based on approximation of the radial distribution functions. This approach allows one to evaluate the distribution of water molecules near an ion entering a graphene pore, and to evaluate the energy barrier cause by desolvation. Our method goes beyond the recently-proposed layered Born model with geometrical constraints [247]. Namely, our method automatically accounts for the pore shape, type of atoms the lattice consists of, type of solvent, and the ion's location near the pore entrance. Analytically tractable decomposition of a PMF and in particular efficient analytical estimation of dehydration barriers is essential for designing selective artificial nanopores in order to construct high-throughput water desalination membranes.

6.3 Future work

Future work may develop along the following lines.

Extensive BD simulations with MD PMFs. An obvious application of the BD system described in Chapter 3 is to use the multi-ion PMFs to study both alike and valence selectivity in KcsA. Some of these PMFs have already been derived in MD studies of the KcsA ion channel [21, 272]. One should be able to compare these results with experimental data.

Another closely related direction is to computationally study the effect of point mutations. To do so, one will need to transform one of the amino acids lining the pore into another. For instance, it has been shown experimentally that changing serine (S) to aspartate (D) in the NaChBac biological ion channel switches its selectivity from Na^+ to Ca^{2+} [18, 273]. The BD simulation can predict the *I-V* and *I-C* relations for the mutants that has not yet been studies experimentally.

Differential Chapman-Kolmogorov (DCK) theory. Another essential step towards building a multi-scale theory of conduction and selectivity in narrow ion channels is to describe the motion of the quasiparticle probabilistically. Using the Langevin equation (4.9) in the effective potential, one can immediately write the corresponding Fokker-Planck equation

$$\begin{aligned}\frac{\partial \rho_m}{\partial t} = -D_m \frac{\partial}{\partial q}\left[\frac{\partial U_m^{eff}(q)}{\partial q}\rho_m + \frac{\partial \rho_m}{\partial q}\right] \\ + W^{m+1\to m}\rho_{m+1} + W^{m-1\to m}\rho_{m-1} \\ - W^{m\to m+1}\rho_m - W^{m\to m-1}\rho_m\end{aligned} \tag{6.1}$$

This equation accounts for the QP's diffusion (first line), and transitions between states (remaining lines). The key point here is to quantify the QP's diffusivity D_m and the rate $W_{m\to n}$ between states. It is important to note that these parameters change in different states of the QP, as do the charge and mass of the QP. In Chapter 4 we have already demonstrated that the potential U_N^{eff} changes with the number of ions in the channel, and obtained some preliminary results on the distribution of transition rates in Chapter 4. Combining all parameters to together in Eq. (6.1), one can estimate the electric current and compare it with available experimental data.

Using the multi-ion PMFs, one should also be able to explain selectivity using the language of quasiparticles. In doing so, the definition of the QP has to be rewritten to incorporate multiple species. The difference in the effective potentials for these QPs should reveal a difference that results in the selectivity of this ion

channel.

Using quasiparticles to quantify gating. It is known that the opening of an ion channel is associated with the motion of the S4 helix [52, 274]. Each S4 helix carries 4 positive charges, usually arginines, that are tied to the helix. Such a system represents an ideal candidate for a quasiparticle, as the charges move in a concerted manner [52]. Thus, it is proposed to derive the effective potentials in which this S4 quasiparticle moves, using Eq. (4.10), and to describe the translocation of the gating charge with atomic accuracy. These theoretical predictions can be further compared with experimental gating currents [275].

A. List of BD tests

A BD simulation can be validated against the following checks:

1. *Setting:* 1D motion, no external potentials, no ion-ion interactions, no boundaries.

   Expected outcome: One should recover the Einstein relation $\langle x^2 \rangle = 2Dt$.

2. *Setting:* 1D domain with a potential $U(z)$, non-interacting particles, reflecting boundaries.

   Expected outcome: Distribution must coincide with $\rho \sim \exp(-U(z)/k_B T)$ after an appropriate normalization.

3. *Setting:* 1D domain, open boundaries, non-interacting particles, asymmetrical bulk concentrations.

   Expected outcome: One should recover the distribution (and compare to an analytical solution or BVP in MATLAB) and the resulting flux.

4. *Setting:* Non-interacting particles, 3D BD domain, no electric field, equal ionic concentrations.

   Expected outcome: No statistically significant current flows.

5. *Setting:* Non-interacting particles, 3D BD domain, no electric field, asymmetrical ionic concentrations.

   Expected outcome: The current should satisfy the analytical solution given by the Fick's law.

6. *Setting:* Non-interacting particles, 3D BD domain, non-zero electric field, equal ionic concentrations.

   Expected outcome: The flux should satisfy the analytical solution given by the Nernst-Planck equation (2.5).

7. *Setting:* 1D domain with a potential $U(z)$, interacting particles [276].

   Expected outcome: Two distribution peaks must appear with their maxima located at the energy minima. The distribution is also analytically/numerically derivable.

8. *Setting:* Field-free domain, interacting particles [276].

   Expected outcome: Maxwellian velocity distributions, the characteristic value of particle velocity is $130\,\mathrm{m/s}$, velocity correlation functions (should be exponential with $\tau = 1/\gamma$). The BD integrator should maintain the temperature constant [110, 222].

9. *Setting:* 3D BD domain with charged particles.

   Expected outcome: Positive particles move along the field (i.e. against the voltage drop), negatively charged particles should move in the opposite direction.

10. Ions do not interact across the membrane.

11. *Setting:* Large fixed charge.

    Expected outcome: all counter-charges pile up at entrance or in the channel, while the alike charges get repelled.

12. *Setting:* Only one ionic species is present in the form of a localised group within an infinite domain.

    Expected outcome: A rapid expansion (burst) of the ionic cloud due to ionic repulsion should occur. Although this sounds obvious, it immediately verifies whether the correct sign in ion-ion forces is being used.

13. When modelling the KcsA channel, negative ions do not pass through the channel.

14. Bulk and buffer concentrations remain constant during a simulation at the prescribed value for each species. In other words, they do not grow in numbers or get depleted.

15. Rule of thumb for the reservoirs: 100mM solution corresponds to 0.06 part / nm^3, $N = 7.3$ particles in $120\mathrm{nm}^3$.

16. Rule of thumb for ionic currents: 1 pA = 1 particle per 160 ns.

17. The ultimate validation: simulation currents corresponds to the experimentally measured values in a channel under various experimental conditions (voltage drop, concentration, species present).

B. Derivation of the Born formula

Assume a continuous isotropic solvent of dielectric permittivity ϵ surrounding a spherical ion of radius R and charge Ze ($e > 0$). The electric induction vector reads as

$$\mathbf{D} = \frac{Ze\mathbf{r}}{4\pi\epsilon_0 r^3}. \tag{B.1}$$

Using the relation

$$\mathbf{D} = \epsilon_0\mathbf{E} + \mathbf{P}$$

connecting $\mathbf{D}$ with the electric field and the polarization vectors, and the constitutive relations in isotropic dielectric

$$\mathbf{P} = \chi\epsilon_0\mathbf{E} = (\epsilon - 1)\epsilon_0\mathbf{E}$$

we arrive at

$$\mathbf{P}(\mathbf{r}) = \Big(1 - \frac{1}{\epsilon}\mathbf{D}\Big).$$

The energy of the ion in the electric field equals the energy of the electrostatic field [277]

$$\begin{aligned} U_\epsilon &= \frac{1}{2}\int_{All\ space} \mathbf{E}\ \mathbf{D}\ \mathrm{d}V = \frac{1}{2}\int_{All\ space} \mathbf{E}\ \mathbf{D}\ r^2\ \mathrm{d}r\ \mathrm{d}\Omega \\ &= 4\pi\frac{\epsilon_0}{2\epsilon}\int_R^\infty \Big(\frac{Ze}{4\pi\epsilon_0 r^2}\Big)^2\ r^2\ \mathrm{d}r = -\frac{(Ze)^2}{4\pi\epsilon\epsilon_0}\frac{1}{R}. \end{aligned}$$

The energy difference of moving the ion from medium with ϵ_1 to a medium with ϵ_2 is

$$\Delta G_{hydr} = U_{\epsilon_2} - U_{\epsilon_1} = -\Big(\frac{1}{\epsilon_2} - \frac{1}{\epsilon_1}\Big)\frac{(Ze)^2}{4\pi\epsilon_0}\frac{1}{R}. \tag{B.2}$$

For $\epsilon_1 = 1$ this formula transforms into the Born formula [277]

$$\Delta G_{hydr} = U_{\epsilon_2} - U_{\epsilon_1} = -\Big(\frac{1}{\epsilon_2} - 1\Big)\frac{(Ze)^2}{4\pi\epsilon_0}\frac{1}{R}. \tag{B.3}$$

C. The van Gunsteren and Berendsen's integrator

Equation (3.1) has to be digitized in order to be processed on a computer. For clarity, we omit the super- and subscripts representing the ionic species or the ion's number. The rule to update ionic coordinates reads as follows [134]

$$\begin{aligned}\mathbf{r}(t_n+\Delta t) =&\mathbf{r}(1+\exp(-\gamma\Delta t)) - \mathbf{r}(t_n-\Delta t)\exp(-\gamma\Delta t)\\ &+\frac{\mathbf{F}(t_n)}{m}\frac{(\Delta t)^2}{\gamma\Delta t}\Big[1-\exp(-\gamma\Delta t)\Big]\\ &+\frac{\dot{\mathbf{F}}(t_n)}{m}\frac{(\Delta t)^2}{(\gamma\Delta t)^2}\Big[\frac{\gamma\Delta t(1+\exp(-\gamma\Delta t))}{2}-(1-\exp(-\gamma\Delta t))\Big]\\ &+\mathbf{\Xi_n}(\Delta t)+\exp(-\gamma\Delta t)\mathbf{\Xi_n}(-\Delta t)+\mathcal{O}[(\Delta t)^4].\end{aligned} \tag{C.1}$$

The essential step is to sample $\mathbf{\Xi_n}(\Delta t)$ and $\mathbf{\Xi_n}(-\Delta t)$ that are correlated. This is do by means of following steps [134].

$$C(\gamma\Delta t) = 2\gamma\Delta t - +4\exp(-\gamma\Delta t) \tag{C.2}$$

$$G(\gamma\Delta t) = \exp(\gamma\Delta t) - 2\gamma\Delta t\exp(-\gamma\Delta t) \tag{C.3}$$

$$\begin{aligned}E(\gamma\Delta t) =&16[\exp(\gamma\Delta t)+\exp(-\gamma\Delta t)] - 4\Big[\exp(2\gamma\Delta t)+\exp(-2\gamma\Delta t)\Big]\\ &-24-4\gamma\Delta t\Big[\exp(\gamma\Delta t)-\exp(-\gamma\Delta t)\Big]\\ &+2\gamma\Delta t\Big[\exp(2\gamma\Delta t)-\exp(-2\gamma\Delta t)\Big]\end{aligned} \tag{C.4}$$

Care should be taken with numerically rounding-off small numbers when computing coefficients C, G, and E in MATLAB. Otherwise the output becomes complex with small imaginary values. The minimal accuracy in MATLAB (call `eps` function) is 2.2204×10^{-16}, and so one should add 1×10^{-16} to any denominators that are likely to be small.

To simplify further formulas, it is convenient to introduce

$$\sigma_2^2[1-r^2] = \sqrt{\frac{D}{\gamma}\frac{E(\gamma\Delta t)}{C(\gamma\Delta t)}} \tag{C.5}$$

$$r\frac{\sigma_2}{\sigma_1} = \frac{G(\gamma\Delta t)}{C(\gamma\Delta t)} \tag{C.6}$$

so that

$$\mathbf{\Xi_n}(-\Delta t) = r\frac{\sigma_2}{\sigma_1}\mathbf{\Xi_{n-1}}(\Delta t) + \sigma_2^2[1-r^2]\mathbf{\Xi} \tag{C.7}$$

where $\mathbf{\Xi}$ is a newly generated $N \times 3$ array of random Gaussian numbers of unit variance.

The velocity of the particles can be evaluated by means of

$$\begin{aligned}\mathbf{v} = \frac{H(\gamma\Delta t)}{\Delta t}\Bigg\{ &\Big[\mathbf{r}(t_n+\Delta t) - \mathbf{r}(t_n-\Delta t)\Big] \\ &+ \left[\frac{\mathbf{F}(t_n)}{m}\frac{(\gamma\Delta t)^2}{(\gamma\Delta t)^2} - \frac{\dot{\mathbf{F}}(t_n)}{m}\frac{(\Delta t)^3}{(\gamma\Delta t)^3}\right]G(\gamma\Delta t) \\ &+ \Big[\mathbf{\Xi_n}(-\Delta t) - \mathbf{\Xi_n}(\Delta t)\Big]\Bigg\}\end{aligned} \tag{C.8}$$

with

$$H(\gamma\Delta t) = \frac{\gamma\Delta t}{\exp(\gamma\Delta t) - \exp(-\gamma\Delta t)}. \tag{C.9}$$

In the limit or large time steps, the algorithm (C.1) simplifies to

$$\mathbf{r}(t_n+\Delta t) = \mathbf{r}(t_n) + \frac{\mathbf{F}(t_n)\Delta t + \frac{1}{2}\dot{\mathbf{F}}(\Delta t)^2}{m\gamma} + \mathbf{\Xi_n}(\Delta t) \tag{C.10}$$

where $\mathbf{\Xi_n}(\Delta t)$ is the appropriately sized set of Gaussian random numbers with

zero mean and variance

$$\left\langle {\boldsymbol{\Xi}_{\mathbf{n}}}^2(\Delta t)\right\rangle = \frac{2k_BT}{m\gamma}\Delta t. \tag{C.11}$$

Glossary

Activation	A transition from a non-conductive to a conductive conformation of an ion channel.
AMFE	Anomalous mole-fraction effect (AMFE) implies that the dependence of the conduction on the mole fraction of the present ionic species has a minimum. In other words, the channel reveals smaller currents when exposed to bi-ionic same-sign ionic solutions than if exposed to a pure solution of either electrolyte.
Binding site	A site in the pore of a biological ion channel where ions predominantly reside (bind) during permeation.
Bjerrum length	The characteristic separation between two charges at which the magnitude of the electrostatic energy becomes equal to the thermal energy.
Born energy	The solvation energy of an ion, calculated as the energy of the electrostatic field in the dielectric surrounding the ion.
Carbonyl group	The $-CO^-$ functional group of atoms, which carries a negative charge.
Carboxyl group	The $-COO^-$ functional group of atoms, which carries a negative charge.

Current saturation	A sublinear dependence of ionic current on the concentration of ions in an electrolyte as a consequence of single-file conduction in narrow channels. This phenomenon is often referred to as Michaelis-Menten saturation due to the analogy with enzyme kinetics.
Debye-Hückel theory	A simplified model describing the properties of electrolytes. It uses the Poisson and Boltzmann equations to describe the equilibrium electric field around a single ion and consequent properties of the electrolyte solution.
Debye length	The characteristic length in the linearized Debye-Hückel theory at which the electrostatic field around an ion weakens by a factor of e.
Electrical double layer	A structure forming at the surface of an object exposed to a solution of electrolyte.
Excess chemical potential	The difference between the chemical potential of a given species and that of an ideal gas under the same conditions (in particular, at the same pressure, temperature, and composition)
Functionalization	In the context of artificial nanopores, the modification of the original pore structure for a given application, by adding functional groups, fixed charges, or embedding atoms of a different species.
Gate	The domain of an ion channel mechanically controlling the openness of the pore.
Gating charge	The charge of the positive amino acid residues on the S4 helix of the voltage sensor domain of a voltage-gated ion channel
Ion channel	A pore-forming protein enabling the permeation of ions across the cellular membrane.

Ionic Coulomb blockade (ICB)	An oscillating dependence of the ionic current through a nanopore in response to increasing the charge embedded in the pore. This phenomenon occurs due to the discreteness of the electric charge and is therefore fundamentally analogous to the electronic Coulomb blockade.
Knock-on conduction	A type of ion permeation in narrow nanopores, in which the ion entering from one side interacts with ions within the pore and thus eventually expels the outermost ion on the far side.
Ligand	An ion or molecule (functional group) that binds to a central metal atom to form a coordination complex.
Patch-clamp technique	An electrophysiological method allowing one to study the conductive properties of the cellular membranes and individual ion channels of biological cells.
Potential of mean force (PMF)	The statistically averaged potential energy of a subsystem, thermodynamically averaged over the irrelevant degrees of freedom.
Radial density function (RDF)	A function proportional to the probability of finding a particle at a specified distance from the reference particle.
Selectivity	The property of an ion channel to conduct preferably one ion species while hampering that for the others.
Selectivity filter	A (usually narrow) part of the pore responsible for conferring the channel's selective properties.
Self-energy barrier	An electrostatic barrier emerging at the interface of two media with different dielectric permittivity due to repulsion exerted by image charges.

Bibliography

[1] Subin Sahu, Massimiliano Di Ventra, and Michael Zwolak. Dehydration as a universal mechanism for ion selectivity in graphene and other atomically thin pores. *Nano Letters*, 17(8):4719–4724, 2017. PMID: 28678508.

[2] Bertil Hille. *Ion Channels of Excitable Membranes*. Sinauer Associates Inc 2001-07, 3rd edition, July 2001.

[3] Stefan Feske, Edward Y. Skolnik, and Murali Prakriya. Ion channels and transporters in lymphocyte function and immunity. *Nat Rev Immunol*, 12(7):532–547, Jun 2012.

[4] David C. Gadsby. Ion channels versus ion pumps: the principal difference, in principle. *Nat. Rev. Mol. Cell Bio.*, 10:344–352, May 2009.

[5] Online guide to pharmacology. `http://www.guidetopharmacology.org/`.

[6] Frances M. Ashcroft. From molecule to malady. *Nature*, 440:440–447, 2006.

[7] Frances M. Ashcroft. *Ion Channels and Disease*. Academic Press, 1999.

[8] Maria L. Garcia and Gregory J. Kaczorowski. Ion channels find a pathway for therapeutic success. *Proceedings of the National Academy of Sciences*, 113(20):5472–5474, 2016.

[9] UN. International Decade for Action "WATER FOR LIFE" 2005-2015. `http://www.un.org/waterforlifedecade/background.shtml`. [Online].

[10] Michael Thomas and Ben Corry. A computational assessment of the permeability and salt rejection of carbon nanotube membranes and their application to water desalination. *Phil. Trans. R. Soc. A*, 374(2060):20150020, 2016.

[11] Anna Lee, Jeffrey W. Elam, and Seth B. Darling. Membrane materials for water purification: design, development, and application. *Environ. Sci.: Water Res. Technol.*, 2:17–42, 2016.

[12] Morten Ø. Jensen, Vishwanath Jogini, Michael P. Eastwood, and David E. Shaw. Atomic-level simulation of current–voltage relationships in single-file ion channels. *J. Gen. Physiol.*, 141(5):619–632, 2013.

[13] Matías R. Machado, Ari Zeida, Leonardo Darré, and Sergio Pantano. From quantum to subcellular scales: multi-scale simulation approaches and the SIRAH force field. *Interface Focus*, 9(3):20180085, 2019.

[14] Hirotaka Ode, Masaaki Nakashima, Shingo Kitamura, Wataru Sugiura, and Hironori Sato. Molecular dynamics simulation in virus research. *Front. Microbiol.*, 3:258, 2012.

[15] Bob Eisenberg. Multiple scales in the simulation of ion channels and proteins. *J. Phys. Chem. C*, 114(48):20719–20733, 2010.

[16] S.H. Chung and D.P. Tieleman. *Computational and Theoretical Approaches to Unraveling the Permeation Dynamics in Biological Nanotubes*, volume 6, pages 567–618. American Scientific Publishers, 2006.

[17] Carmen Domene, editor. *Computational Biophysics of Membrane Proteins*. The Royal Society of Chemistry, 2017.

[18] Carlo Guardiani, Olena A. Fedorenko, Igor A. Khovanov, and Stephen K. Roberts. Different roles for aspartates and glutamates for cation permeation in bacterial sodium channels. *Biochimica et Biophysica Acta (BBA) - Biomembranes*, 1861(2):495 – 503, 2019.

[19] Declan A. Doyle et al. The structure of the potassium channel: molecular basis of K^+ conduction and selectivity. *Science*, 280(5360):69–77, 1998.

[20] Shin-Ho Chung, Olaf S. Anderson, and Vikram V. Krishnamurthy, editors. *Biological Membrane Ion Channels*. Springer, 2007.

[21] Simone Furini and Carmen Domene. Atypical mechanism of conduction in potassium channels. *Proc. Nat. Acad. Sci. (USA)*, 106(38):16074–16077, 2009.

[22] Jie Zheng, Erin M. Lennon, Heng-Kwong Tsao, Yu-Jane Sheng, and Shaoyi Jiang. Transport of a liquid water and methanol mixture through carbon nanotubes under a chemical potential gradient. *J. Chem. Phys.*, 122(21):214702, 2005.

[23] Benoît Roux. Ion channels and ion selectivity. *Essays In Biochemistry*, 61(2):201–209, 2017.

[24] Ben Corry. Mechanisms of selective ion transport and salt rejection in carbon nanostructures. *MRS Bulletin*, 42(4):306–310, 2017.

[25] João H. Morais-Cabral, Yufeng Zhou, and Roderick MacKinnon. Energetic optimization of ion conduction rate by the K^+ selectivity filter. *Nature*, 414:37–42, Nov 2001.

[26] Gerhard Hummer. Potassium ions line up. *Science*, 346(6207):303–303, 2014.

[27] Benoît Roux. Ion conduction and selectivity in K^+ channels. *Ann. Rev. Biophys. Biomol. Struct.*, 34(1):153–171, 2005. PMID: 15869387.

[28] by E.M. Lifshitz, L.P. Pitaevskii, Kosevich. A.M., J.B. Sykes, and R.N. Franklin. *Physical kinetics*. Butterworth-Heinemann, 1981.

[29] Kenneth A. Johnson and Roger S. Goody. The original Michaelis constant: Translation of the 1913 Michaelis–Menten paper. *Biochemistry.*, 50(39):8264–8269, 2011.

[30] Turgut Baştuğ and Serdar Kuyucak. Molecular dynamics simulations of membrane proteins. *Biophys. Rev.*, 4(3):271–282, Sep 2012.

[31] David Medovoy, Eduardo Perozo, and Benoît Roux. Multi-ion free energy landscapes underscore the microscopic mechanism of ion selectivity in the KcsA channel. *Biochim. Biophys. Acta, Biomembr.*, 1858(7, Part B):1722 – 1732, 2016.

[32] George Eisenman. Cation selective glass electrodes and their mode of operation. *Biophys. J.*, 2(2, Part 2):259 – 323, 1962.

[33] George Eisenman and Richard Horn. Ionic selectivity revisited: The role of kinetic and equilibrium processes in ion permeation through channels. *The Journal of Membrane Biology*, 76(3):197–225, Oct 1983.

[34] Sergei Yu. Noskov, Simon Bernèche, and Benoît Roux. Control of ion selectivity in potassium channels by electrostatic and dynamic properties of carbonyl ligands. *Nature*, 431:830–834, 2004.

[35] Shijun Zhao, Jianming Xue, and Wei Kang. Ion selection of charge-modified large nanopores in a graphene sheet. *J. Chem. Phys.*, 139(11):114702, 2013.

[36] Hasti Amiri, Kenneth L. Shepard, Colin Nuckolls, and Raúl Hernández Sánchez. Single-walled carbon nanotubes: Mimics of biological ion channels. *Nano Lett.*, 17(2):1204–1211, 2017. PMID: 28103039.

[37] Juan J. Nogueira and Ben Corry. *The Oxford Handbook of Neuronal Ion Channels*, chapter Ion Channel Permeation and Selectivity. Oxford Handbooks Online, 2019. published online, URL: https://www.oxfordhandbooks.com/view/10.1093/oxfordhb/9780190669164.001.0001/oxfordhb-9780190669164-e-22.

[38] Ben Corry. Na^+/Ca^{2+} selectivity in the bacterial voltage-gated sodium channel NavAb. *PeerJ*, 1:e16, 2013.

[39] Sergei Yu. Noskov and Benoît Roux. Ion selectivity in potassium channels. *Biophys. Chem.*, 124(3):279 – 291, 2006. Ion Hydration Special Issue.

[40] Sameer Varma, David M. Rogers, Lawrence R. Pratt, and Susan B. Rempe. Design principles for K^+ selectivity in membrane transport. *J. Gen. Physiol.*, 137(6):479–488, 2011.

[41] Dmitry G Luchinsky, Wiliam A. T. Gibby, Igor Kh. Kaufman, D.A. Timucin, and P.V.E. McClintock. Statistical theory of selectivity and conductivity in biological channels. *ArXiv e-prints*, April 2016.

[42] W. A. T. Gibby, M. L. Barabash, C. Guardiani, D. G. Luchinsky, O. A. Fedorenko, S. K. Roberts, and P. V. E. McClintock. Theory and experiments on multi-ion permeation and selectivity in the NaChBac ion channel. *Fluct. Noise Lett.*, 18(02):1940007, 2019.

[43] W.A.T. Gibby, M.L. Barabash, C. Guardiani, D.G. Luchinsky, and P.V.E. McClintock. Statistical theory of mixed-valence selectivity in biological ion channels. In *25^{th} International Conference of Noise and Fluctuations (ICNF)*, pages 252–255, 2019.

[44] Michael Thomas, Dylan Jayatilaka, and Ben Corry. How does overcoordination create ion selectivity? *Biophysical Chemistry*, 172:37 – 42, 2013.

[45] Dezsö Boda, David D. Busath, Bob Eisenberg, Douglas Henderson, and Wolfgang Nonner. Monte carlo simulations of ion selectivity in a biological Na channel: Charge–space competition. *Phys. Chem. Chem. Phys.*, 4:5154–5160, 2002.

[46] Dirk Gillespie and Dezsö Boda. The anomalous mole fraction effect in calcium channels: A measure of preferential selectivity. *Biophys. J.*, 95:2658 – 2672, 2008.

[47] Gábor Rutkai, Dezső Boda, and Tamás Kristóf. Relating binding affinity to dynamical selectivity from dynamic Monte Carlo simulations of a model calcium channel. *J. Phys. Chem. Lett.*, 1(23):2179–2184, 2010.

[48] Boda Dezsö, Wolfgang Nonner, Douglas Henderson, Bob Eisenberg, and Dirk Gillespie. Volume exclusion in calcium selective channels. *Biophys. J.*, 94(9):3486 – 3496, 2008.

[49] Alexander M. Berezhkovskii, Leonardo Dagdug, and Sergey M. Bezrukov. Bulk-mediated surface transport in the presence of bias. *J. Chem.Phys.*, 147(1):014103, 2017.

[50] Nir Gavish, Chun Liu, and Bob Eisenberg. Do bistable steric Poisson–Nernst–Planck models describe single-channel gating? *J. Phys.Chem. B*, 122(20):5183–5192, 2018. PMID: 29715026.

[51] Sergey M. Bezrukov and John J. Kasianowicz. Current noise reveals protonation kinetics and number of ionizable sites in an open protein ion channel. *Phys. Rev. Lett.*, 70:2352–2355, Apr 1993.

[52] William A. Catterall. Ion channel voltage sensors: Structure, function, and pathophysiology. *Neuron*, 67(6):915 – 928, 2010.

[53] Richard S. Lewis, Paul E. Ross, and Michael D. Cahalan. Chloride channels activated by osmotic stress in T lymphocytes. *J. Gen. Physiol.*, 101:801–826, Jun 1993.

[54] Christopher Maffeo, Swati Bhattacharya, Jejoong Yoo, David Wells, and Aleksei Aksimentiev. Modeling and simulation of ion channels. *Chem. Rev.*, pages 6250–6284, 2012.

[55] Fatemeh Khalili-Araghi, James Gumbart, Po-Chao Wen, Marcos Sotomayor, Emad Tajkhorshid, and Klaus Schulten. Molecular dynamics simulations of membrane channels and transporters. *Curr. Opin. Struct. Biol.*, 19(2):128 – 137, 2009. Theory and simulation / Macromolecular assemblages.

[56] Vladimir Yarov-Yarovoy, Paul G. DeCaen, Ruth E. Westenbroek, Chien-Yuan Pan, Todd Scheuer, David Baker, and William A. Catterall. Structural basis for gating charge movement in the voltage sensor of a sodium channel. *Proc. Nat. Acad. Sci. (USA)*, 109(2):E93–E102, 2012.

[57] Guido Michels, Jan Matthes, Renate Handrock, Ute Kuchinke, Ferdi Groner, Leanne L. Cribbs, Alexey Pereverzev, Toni Schneider, Edward Perez-Reyes, and Stefan Herzig. Single-channel pharmacology of mibefradil in human native T-type and recombinant Cav3.2 calcium channels. *Mol. Pharmacol.*, 61(3):682–694, 2002.

[58] William Humphrey, Andrew Dalke, and Klaus Schulten. VMD: Visual molecular dynamics. *J. Mol. Graph.*, 14(1):33 – 38, 1996.

[59] T. W. Allen, A. Bliznyuk, A. P. Rendell, S. Kuyucak, and S.-H. Chung. The potassium channel: Structure, selectivity and diffusion. *J. Chem. Phys.*, 112(18):8191–8204, 2000.

[60] Simon Bernèche and Benoît Roux. A microscopic view of ion conduction through the K^+ channel. *Proc. Nat. Acad. Sci. (USA*, 100(15):8644–8648, 2003.

[61] Carmen Domene and Mark S.P. Sansom. Potassium channel, ions, and water: Simulation studies based on the high resolution X-Ray structure of KcsA. *Biophys. J.*, 85(5):2787 – 2800, 2003.

[62] Yufeng Zhou and Roderick MacKinnon. The occupancy of ions in the k+ selectivity filter: Charge balance and coupling of ion binding to a protein conformational change underlie high conduction rates. *J. Mol. Biol.*, 333(5):965 – 975, 2003.

[63] Roderick MacKinnon. Potassium channels. *FEBS Lett.*, 555(1):62–65, 2003.

[64] VB Luzhkov and J Aqvist. A computational study of ion binding and protonation states in the kcsa potassium channel. *BBA*, 1481(2):360—370, 2000.

[65] Johan Åqvist and Victor Luzhkov. Ion permeation mechanism of the potassium channel. *Nature*, 404:881–884, 2000.

[66] David A. Köpfer, Chen Song, Tim Gruene, George M. Sheldrick, Ulrich Zachariae, and Bert L. de Groot. Ion permeation in K^+ channels occurs by direct Coulomb knock-on. *Science*, 346(6207):352–355, 2014.

[67] Wojciech Kopec, David A. Köpfer, Owen N. Vickery, Anna S. Bondarenko, Thomas L. C. Jansen, Bert L. de Groot, and Ulrich Zachariae. Direct knock-on of desolvated ions governs strict ion selectivity in K^+ channels. *Nat. Chem.*, 10:813–820, 2018.

[68] Huong T. Kratochvil, Joshua K. Carr, Kimberly Matulef, Alvin W. Annen, Hui Li, Michał Maj, Jared Ostmeyer, Arnaldo L. Serrano, H. Raghuraman, Sean D. Moran, J. L. Skinner, Eduardo Perozo, Benoît Roux, Francis I. Valiyaveetil, and Martin T. Zanni. Instantaneous ion configurations in the K^+ ion channel selectivity filter revealed by 2D IR spectroscopy. *Science*, 353(6303):1040–1044, 2016.

[69] H. Schrempf, O. Schmidt, R. Kümmerlen, S. Hinnah, D. Müller, M. Betzler, T. Steinkamp, and R. Wagner. A prokaryotic potassium ion channel with two predicted transmembrane segments from *Streptomyces lividans*. *EMBO J.*, 14(21):5170–5178, 1995.

[70] D. Meuser, H. Splitt, R. Wagner, and H. Schrempf. Exploring the open pore of the potassium channel from *Streptomyces lividans*. *FEBS Lett.*, 462(3):447–452, 1999.

[71] E Zakharian and R.N Reusch. Streptomyces lividans potassium channel KcsA is regulated by the potassium electrochemical gradient. *Biochem. Biophys. Res. Comm.*, 316(2):429 – 436, 2004.

[72] E. Zakharian and R.N. Reusch. Functional evidence for a supramolecular structure for the *Streptomyces lividans* potassium channel KcsA. *Biochem. Biophys. Res. Comm.*, 322(3):1059 – 1065, 2004.

[73] Crina M. Nimigean and Christopher Miller. Na^+ block and permeation in a K^+ channel of known structure. *J. Gen. Physiol.*, 120(3):323–335, 2002.

[74] Crina M. Nimigean, Joshua S. Chappie, and Christopher Miller. Electrostatic tuning of ion conductance in potassium channels. *Biochemistry*, 42(31):9263–9268, 2003. PMID: 12899612.

[75] Meredith LeMasurier, Lise Heginbotham, and Christopher Miller. KcsA: it's a potassium channel. *J. Gen. Physiol.*, 118(3):303–314, 2001.

[76] Kene N. Piasta, Douglas L. Theobald, and Christopher Miller. Potassium-selective block of barium permeation through single kcsa channels. *The Journal of General Physiology*, 138(4):421–436, 2011.

[77] Shin-Ho Chung, Matthew Hoyles, Toby Allen, and Serdar Kuyucak. Study of ionic currents across a model membrane channel using Brownian Dynamics. *Biophysical Journal*, 75(2):793 – 809, 1998.

[78] Shin-Ho Chung, Toby W. Allen, Matthew Hoyles, and Serdar Kuyucak. Permeation of ions across the potassium channel: Brownian dynamics studies. *Biophys. J.*, 77(5):2517–2533, 1999.

[79] T.W. Allen and S.H. Chung. Brownian dynamics study of an open-state KcsA potassium channel. *BBA*, 1515(2):83 – 91, 2001.

[80] Peter Hugo Nelson. Modeling the concentration-dependent permeation modes of the KcsA potassium ion channel. *Phys. Rev. E*, 68:061908, Dec 2003.

[81] Shin-Ho Chung and Ben Corry. Conduction properties of KcsA measured using Brownian dynamics with flexible carbonyl groups in the selectivity filter. *Biophys. J.*, 93(1):44 – 53, 2007.

[82] Miten Jain, Hugh E. Olsen, Benedict Paten, and Mark Akeson. The Oxford Nanopore MinION: delivery of nanopore sequencing to the genomics community. *Genome Biol.*, 17(1):239, 2016.

[83] Mario Tagliazucchi and Igal Szleifer. Transport mechanisms in nanopores and nanochannels: can we mimic nature? *Materials Today*, 18(3):131 – 142, 2015.

[84] William Alexander Thomas Gibby, Miraslau Barabash, Carlo Guardiani, Dmitry Luchinsky, and Peter Vaughan Elsmere McClintock. The role of noise in determining selective ionic conduction through nano-pores. In *2018 IEEE 13th Nanotechnology Materials and Devices Conference (NMDC)*. IEEE, 1 2019.

[85] Ryan C. Rollings and Jene A. Kuan, Aaron T. Golovchenko. Ion selectivity of graphene nanopores. *Nat. Comm.*, 7, 2016.

[86] Zhi-Yong Wang and Jianzhong Wu. Ion association at discretely-charged dielectric interfaces: Giant charge inversion. *J. Chem. Phys.*, 147(2):024703, 2017.

[87] Zhongjin He, Jian Zhou, Xiaohua Lu, and Ben Corry. Bioinspired graphene nanopores with voltage-tunable ion selectivity for Na^+ and K^+. *ACS Nano*, 7:10148–10157, 2013.

[88] Michael M. Thackeray, Christopher Wolverton, and Eric D. Isaacs. Electrical energy storage for transportation—approaching the limits of, and going beyond, lithium-ion batteries. *Energy Environ. Sci.*, 5:7854–7863, 2012.

[89] Yang Ruan, Yudan Zhu, Yumeng Zhang, Qingwei Gao, Xiaohua Lu, and Linghong Lu. Molecular dynamics study of Mg^{2+}/Li^+ separation via

biomimetic graphene-based nanopores: The role of dehydration in second shell. *Langmuir*, 32(51):13778–13786, 2016. PMID: 27756127.

[90] Alessandro Siria, Philippe Poncharal, Anne-Laure Biance, Rémy Fulcrand, Xavier Blase, Stephen T. Purcell, and Lydéric Bocquet. Giant osmotic energy conversion measured in a single transmembrane boron nitride nanotube. *Nature*, 494:455–458, 2013.

[91] Benoît Roux, T. Allen, S. Berneche, and W. Im. Theoretical and computational models of biological ion channels. *Q. Rev. Biophys*, 37(1):15–103, Feb 2004.

[92] Jan Drenth and Jeroen Mesters. *Principles of Protein X-Ray Crystallography*. Springer, 3rd edition, 2007.

[93] Joachim Frank. *Three-Dimensional Electron Microscopy of Macromolecular Assemblies: Visualization of Biological Molecules in Their Native State*. Oxford University Press, 2006.

[94] RCSB protein data bank. `https://www.rcsb.org/pdb/home/home.do`.

[95] Martin Burger. Inverse problems in ion channel modelling. *Inverse Problems*, 27(8):083001, jul 2011.

[96] Bert Sakmann and Erwin Neher, editors. *Single-channel recording*. Springer, 1995.

[97] Nikita Gamper, editor. *Ion Channels: Methods and Protocols*. Humana Press, 2nd edition, 2013.

[98] Areles Molleman, editor. *Patch Clamping: An Introductory Guide To Patch Clamp Electrophysiology*. John Wiley & Sons, Ltd, 2002.

[99] Jie Zheng and Matthew C. Trudeau, editors. *Handbook of Ion Channels*. CRC Press, Taylor & Francis Group, 6000 Broken Sound Parkway NW, Suite 300; Boca Raton, FL 33487-2742, Oct 2015.

[100] Patch me if you can – what is the patch-clamp technique? https://puzzledponderer.wordpress.com. Online; accessed February 21, 2020.

[101] The patch-clamp technique an introduction. https://www.leica-microsystems.com/science-lab/the-patch-clamp-technique/. Online; accessed February 21, 2020.

[102] Michael Pusch and Erwin Neher. Rates of diffusional exchange between small cells and a measuring patch pipette. *Pflügers Archiv*, 411(2):204–211, Feb 1988.

[103] Musa Ozboyaci, Daria B. Kokh, Stefano Corni, and Rebecca C. Wade. Modeling and simulation of protein–surface interactions: achievements and challenges. *Q. Rev. Biophys.*, 49:e4, 2016.

[104] Tomasz Pieńko and Joanna Trylska. Computational methods used to explore transport events in biological systems. *J. Chem. Inform. Modeling*, 59(5):1772–1781, 2019. PMID: 30879306.

[105] Serdar Kuyucak, Olaf Sparre Andersen, and Shin-Ho Chung. Models of permeation in ion channels. *Rep. Prog. Phys.*, 64:1427, Oct 2001.

[106] Shin-Ho Chung and Ben Corry. Three computational methods for studying permeation, selectivity and dynamics in biological ion channels. *Soft Matter*, 1:417–427, Nov 2005.

[107] Jin Kyoung Park, Kelin Xia, and Guo-Wei Wei. Atomic scale design and three-dimensional simulation of ionic diffusive nanofluidic channels. *Microfluidics and Nanofluidics*, 19(3):665–692, Sep 2015.

[108] Dominik Marx and Juerg Hutter. *Ab-initio Molecular Dynamics: Theory and Implementation*, chapter 13, pages 301–449. NIC. Forschungszentrum Jülich, i edition, 2000. Publicly available at the URL http://www2.fz-juelich.de/nic-series/Volume3/marx.pdf.

[109] Hu Qiu, Minmin Xue, Chun Shen, Zhuhua Zhang, and Wanlin Guo. Graphynes for water desalination and gas separation. *Adv. Mat.*, 0(0):1803772, 2019.

[110] M. P. Allen and D. J. Tildesley. *Computer Simulation of Liquids*. Clarendon Press, New York, NY, USA, 1987.

[111] Ben Leimkuhler and Charles Matthews. *Molecular Dynamics*, volume 39 of *Interdisciplinary Applied Mathematics*. Springer, 2015.

[112] Jonathan N. Sachs, Paul S. Crozier, and Thomas B. Woolf. Atomistic simulations of biologically realistic transmembrane potential gradients. *J. Chem. Phys.*, 121(22):10847–10851, 2004.

[113] Jeffrey Comer and Aleksei Aksimentiev. Predicting the DNA sequence dependence of nanopore ion current using atomic-resolution Brownian dynamics. *J. Phys. Chem. C*, 116(5):3376–3393, 2012.

[114] Denis Bucher and Ursula Rothlisberger. Molecular simulations of ion channels: a quantum chemist's perspective. *J. Gen. Physiol.*, 135(6):549–554, 2010.

[115] Ron O. Dror, Morten Ø. Jensen, David W. Borhani, and David E. Shaw. Exploring atomic resolution physiology on a femtosecond to millisecond timescale using molecular dynamics simulations. *J. Gen. Physiol.*, 135(6):555–562, 2010.

[116] Michael Thomas, Ben Corry, and Tamsyn A. Hilder. What have we learnt about the mechanisms of rapid water transport, ion rejection and selectivity in nanopores from molecular simulation? *Small*, 10(8):1453–1465, 2014.

[117] D. Peter Tieleman, Phil C. Biggin, Graham R. Smith, and Mark S. P. Sansom. Simulation approaches to ion channel structure–function relationships. *Q. Rev. Biophys.*, 34(4):473–561, 2001.

[118] Christopher M. Baker. Polarizable force fields for molecular dynamics simulations of biomolecules. *Wiley Interdisciplinary Reviews: Comput. Mol. Sci.*, 5(2):241–254, 2015.

[119] Celeste Sagui and Thomas A. Darden. Molecular dynamics simulations of biomolecules: long-range electrostatics effects. *Annu. Rev. Biophys. Biomol. Struct.*, 28:155–79, 1999.

[120] John G. Kirkwood. Statistical mechanics of fluid mixtures. *J. Chem. Phys.*, 3(5):300–313, 1935.

[121] Benoît Roux. The calculation of the potential of mean force using computer simulations. *Comput. Phys. Commun.*, 91(1):275 – 282, 1995.

[122] Benoît Roux. Statistical mechanical equilibrium theory of selective ion channels. *Biophys. J.*, 77(1):139 – 153, 1999.

[123] Arieh Ben-Naim. *Molecular Theory of Solutions*. OUP Oxford, 2006.

[124] Bernhard Egwolf and Benoît Roux. Ion selectivity of the KcsA channel: A perspective from multi-ion free energy landscapes. *J. Mol. Biol.*, 401(5):831 – 842, 2010.

[125] A. Burykin, C. N. Schutz, J. Villá, and A. Warshel. Simulations of ion current in realistic models of ion channels: The kcsa potassium channel. *Proteins: Struct., Funct., and Bioinf.*, 47(3):265–280, 2002.

[126] A. Warshel, F. Sussman, and G. King. Free energy of charges in solvated proteins: microscopic calculations using a reversible charging process. *Biochemistry*, 25(26):8368–8372, 1986. PMID: 2435316.

[127] G.M. Torrie and J.P. Valleau. Nonphysical sampling distributions in Monte Carlo free-energy estimation: Umbrella sampling. *J. Comput. Phys.*, 23(2):187 – 199, 1977.

[128] Sergei Izrailev, Sergey Stepaniants, Barry Isralewitz, Dorina Kosztin, Hui Lu, Ferenc Molnar, Willy Wriggers, and Klaus Schulten. Steered molecular dynamics. In Peter Deuflhard, Jan Hermans, Benedict Leimkuhler, Alan E. Mark, Sebastian Reich, and Robert D. Skeel, editors, *Computational Molecular Dynamics: Challenges, Methods, Ideas*, pages 39–65, Berlin, Heidelberg, 1999. Springer Berlin Heidelberg.

[129] Donald L. Ermak and J. A. McCammon. Brownian dynamics with hydrodynamic interactions. *The Journal of Chemical Physics*, 69(4):1352–1360, 1978.

[130] Matthew Hoyles, Serdar Kuyucak, and Shin-Ho Chung. Computer simulation of ion conductance in membrane channels. *Phys. Rev. E*, 58:3654–3661, Sep 1998.

[131] Artem B. Mamonov, Rob D. Coalson, Abraham Nitzan, and Maria G. Kurnikova. The role of the dielectric barrier in narrow biological channels: A novel composite approach to modeling single-channel currents. *Biophys. J.*, 84(6):3646 – 3661, 2003.

[132] Claudio Berti, Simone Furini, Dirk Gillespie, Dezsö Boda, Robert S. Eisenberg, Enrico Sangiorgi, and Claudio Fiegna. Three-dimensional Brownian dynamics simulator for the study of ion permeation through membrane pores. *J. Chem. Theory Comput.*, 10(8), 2014.

[133] Carlos J. F. Solano, Karunakar R. Pothula, Jigneshkumar D. Prajapati, Pablo M. De Biase, Sergei Yu. Noskov, and Ulrich Kleinekathöfer. BROMOCEA code: an improved grand canonical Monte Carlo/Brownian dynamics algorithm including explicit atoms. *J. Chem. Theor. Comput.*, 12(5):2401–2417, 2016.

[134] W. F. van Gunsteren and H. J. C. Berendsen. Algorithms for Brownian dynamics. *Mol. Phys.*, 45(3):637–647, 1982.

[135] A. Singer, Z. Schuss, and B. Nadler. Unidirectional flux in brownian and Langevin simulations of diffusion. *AIP Conf. Proc.*, 800(1):400–406, 2005.

[136] Jim C Chen and Albert S Kim. Brownian dynamics, molecular dynamics, and Monte Carlo modeling of colloidal systems. *Adv. Colloid Interface Sci.*, 112(1-3):159—173, December 2004.

[137] Dan Gordon, Vikram Krishnamurthy, and Shin-Ho Chung. Generalized Langevin models of molecular dynamics simulations with applications to ion channels. *J. Chem. Phys.*, 131(13):134102, 2009.

[138] A. Singer and Z. Schuss. Brownian simulations and unidirectional flux in diffusion. *Phys. Rev. E*, 71:026115, Feb 2005.

[139] Charles R. Doering and Jonathan C. Gadoua. Resonant activation over a fluctuating barrier. *Phys. Rev. Lett.*, 69:2318–2321, Oct 1992.

[140] Ben Corry et al. Reservoir boundaries in Brownian dynamics simulations of ion channels. *Biophys. J.*, 82(4):1975 – 1984, 2002.

[141] Wonpil Im, Stefan Seefeld, and Benoît Roux. A grand canonical Monte Carlo–Brownian dynamics algorithm for simulating ion channels. *Biophys. J.*, 79(2):788 – 801, 2000.

[142] Ben Corry, Toby W. Allen, Serdar Kuyucak, and Shin-Ho Chung. Mechanisms of permeation and selectivity in calcium channels. *Biophysical Journal*, 80(1):195 – 214, 2001.

[143] D. G. Luchinsky, R. Tindjong, I. Kaufman, P. V. E. McClintock, and R. S. Eisenberg. Charge fluctuations and their effect on conduction in biological ion channels. *J. Stat. Mech.: Theor. and Exp.*, 2009(01):P01010, 2009.

[144] S. O. Yesylevskyy and V. N. Kharkyanen. Quasi-particles in the selectivity filter can explain permeation in a channel with multiple occupancy. *Phys. Chem. Chem. Phys.*, 6:3111–3122, 2004.

[145] Bernhard Egwolf, Yun Luo, D. Eric Walters, and Benoît Roux. Ion selectivity of α-hemolysin with β-cyclodextrin adapter. ii. multi-ion effects studied with grand canonical Monte Carlo/Brownian dynamics simulations. *J. Phys. Chem. B*, 114(8):2901–2909, 2010. PMID: 20146515.

[146] Robert S Eisenberg. Interacting ions in biophysics: Real is not ideal. *Biophys J*, 104(9):1849–1866, May 2013.

[147] Robert S. Eisenberg. Updating Maxwell with electrons, charge, and more realistic polarization. ArXiV preprint, 2019.

[148] Uwe Winter and Tihamér Geyer. Coarse grained simulations of a small peptide: Effects of finite damping and hydrodynamic interactions. *J. Chem. Phys.*, 131(10):104102, 2009.

[149] Paul S. Crozier, Douglas Henderson, Richard L. Rowley, and David D. Busath. Model channel ion currents in NaCl-extended simple point charge water solution with applied-field molecular dynamics. *Biophys. J.*, 81(6):3077 – 3089, 2001.

[150] Masayuki Iwamoto and Shigetoshi Oiki. Counting ion and water molecules in a streaming file through the open-filter structure of the K channel. *J. Neurosci.*, 31(34):12180–12188, 2011.

[151] Adrian H. Elcock. Molecule-centered method for accelerating the calculation of hydrodynamic interactions in Brownian dynamics simulations containing many flexible biomolecules. *J. Chem. Theory Comput.*, pages 3224–3239, 2013.

[152] Carlos J. F. Solano, Jigneshkumar D. Prajapati, Karunakar R. Pothula, and Ulrich Kleinekathöfer. Brownian dynamics approach including explicit atoms for studying ion permeation and substrate translocation across nanopores. *J. Chem. Theor. Comput.*, 14(12):6701–6713, 2018. PMID: 30407818.

[153] Z. Schuss, B. Nadler, and R. S. Eisenberg. Derivation of Poisson and Nernst-Planck equations in a bath and channel from a molecular model. *Phys. Rev. E*, 64:036116, Aug 2001.

[154] Boaz Nadler, Uwe Hollerbach, and R. S. Eisenberg. Dielectric boundary force and its crucial role in gramicidin. *Phys. Rev. E*, 68:021905, Aug 2003.

[155] Nikolai N. Bogoliubov. Kinetic equations. *Sov. Phys. JETP*, 10:265–274, 1946.

[156] Paul C. Bressloff and Jay M. Newby. Stochastic models of intracellular transport. *Rev. Mod. Phys.*, 85:135–196, Jan 2013.

[157] John David Jackson. *Classical Electrodynamics*. John Wiley & Sons, 3rd edition, 1998.

[158] Michael Zwolak, James Wilson, and Massimiliano Di Ventra. Dehydration and ionic conductance quantization in nanopores. *J. Phys.: Cond. Matt.*, 22(45):454126, 2010.

[159] Ben Corry, S Kuyucak, and S H Chung. Tests of continuum theories as models of ion channels. II. Poisson-Nernst-Planck theory versus Brownian dynamics. *Biophys J.*, 78:2364, May 2000.

[160] Scott Edwards, Ben Corry, Serdar Kuyucak, and Shin-Ho Chung. Continuum electrostatics fails to describe ion permeation in the Gramicidin channel. *Biophys. J.*, 83(3):1348 – 1360, 2002.

[161] R. S. Eisenberg, M. M. Kl/osek, and Z. Schuss. Diffusion as a chemical reaction: Stochastic trajectories between fixed concentrations. *J. Chem. Phys.*, 102(4):1767–1780, 1995.

[162] Ben Corry, Serdar Kuyucak, and Shin-Ho Chung. Test of Poisson-Nernst-Planck theory in ion channels. *J. Gen. Physiol.*, 114(4):597–600, 1999.

[163] Matt Krems and Massimiliano Di Ventra. Ionic coulomb blockade in nanopores. *Journal of Physics: Condensed Matter*, 25(6):065101, 2013.

[164] Peter Graf, Abraham Nitzan, Maria G. Kurnikova, and Rob D. Coalson. A dynamic lattice Monte Carlo model of ion transport in inhomogeneous dielectric environments: method and implementation. *J. Phys. Chem.*, pages 12324–12338, 2000.

[165] Chen Song and Ben Corry. Testing the applicability of Nernst-Planck theory in ion channels: Comparisons with Brownian dynamics simulations. *PLOS ONE*, 6(6):1–11, 06 2011.

[166] Bob Eisenberg, Yun Kyong Hyon, and Chun Liu. Energy variational analysis of ions in water and channels: Field theory for primitive models of complex ionic fluids. *J. Chem. Phys.*, 133(10), 2010.

[167] Tzyy-Leng Horng, Tai-Chia Lin, Chun Liu, and Bob Eisenberg. Pnp equations with steric effects: A model of ion flow through channels. *The Journal of Physical Chemistry B*, 116(37):11422–11441, 2012. PMID: 22900604.

[168] Jinn-Liang Liu and Bob Eisenberg. Poisson-Nernst-Planck-Fermi theory for modeling biological ion channels. *J. Chem. Phys.*, 141(22), 2014.

[169] Jinn-Liang Liu, Hann-jeng Hsieh, and Bob Eisenberg. Poisson-Fermi modeling of the ion exchange mechanism of the sodium/calcium exchanger. *J. Phys. Chem. B*, 120(10):2658–2669, 2016. PMID: 26906748.

[170] Dirk Gillespie, Wolfgang Nonner, and Robert S Eisenberg. Coupling Poisson Nernst Planck and density functional theory to calculate ion flux. *J. Phys.: Cond. Matt.*, 14(46):12129–12145, nov 2002.

[171] Nikolay A. Simakov and Maria G. Kurnikova. Soft wall ion channel in continuum representation with application to modeling ion currents in α-hemolysin. *J. Phys. Chem. B*, 114(46):15180–15190, 2010.

[172] Boaz Nadler, Zeev Schuss, Amit Singer, and Robert S. Eisenberg. Ionic diffusion through confined geometries: from Langevin equations to partial differential equations. *J. Phys. Condens. Matter*, 16(22):S2153, 2004.

[173] W. Rocchia, E. Alexov, and B. Honig. Extending the applicability of the nonlinear Poisson-Boltzmann equation: Multiple dielectric constants and multivalent ions. *J. Phys. Chem. B*, 105(28):6507–6514, 2001.

[174] Nathan A. Baker, David Sept, Simpson Joseph, Michael J. Holst, and J. Andrew McCammon. Electrostatics of nanosystems: Application to microtubules and the ribosome. *Proc. Nat. Acad. Sci. (USA)*, 98(18):10037–10041, 2001.

[175] I. Borukhov, D. Andelman, and H. Orland. Adsorption of large ions from an electrolyte solution: a modified Poisson–Boltzmann equation. *Electrochimica Acta*, 46(2):221 – 229, 2000.

[176] William Alexander Thomas Gibby. *Statistical Theory of Selectivity and Conductivity in Narrow Biological Ion Channels: Studies of KcsA*. PhD thesis, Lancaster University, 2018.

[177] I Kaufman, D G Luchinsky, R R Tindjong, P V E McClintock, and R S Eisenberg. Multi-ion conduction bands in a simple model of calcium ion channels. *Phys. Biol.*, 10(2):026007, 2013.

[178] J. Zhang, A. Kamenev, and B. I. Shklovskii. Conductance of ion channels and nanopores with charged walls: A toy model. *Phys. Rev. Lett.*, 95:148101, Sep 2005.

[179] J. Zhang, A. Kamenev, and B. I. Shklovskii. Ion exchange phase transitions in water-filled channels with charged walls. *Phys. Rev. E*, 73:051205, May 2006.

[180] R.S. Eisenberg. Computing the field in proteins and channels. *J. Membr. Biol.*, 150(1):1–25, Mar 1996.

[181] Crispin Gardiner. *Stochastic Methods.* Springer Series in Synergetics. Springer, 2009.

[182] Peter Hänggi, Peter Talkner, and Michal Borkovec. Reaction-rate theory: fifty years after Kramers. *Rev. Mod. Phys.*, 62:251–341, Apr 1990.

[183] B. Corry and S.-H. Chung. Mechanisms of valence selectivity in biological ion channels. *Cellular and Molecular Life Sciences CMLS*, 63(3):301–315, Feb 2006.

[184] Robert S. Eisenberg. From structure to function in open ionic channels. *J. Membrane Biol.*, 171:1–24, May 1999.

[185] Robert S Eisenberg. Mass action and conservation of current. *Hung. J. Ind. Chem.*, 44:1–28, 2016.

[186] R. Jay Mashl, Yuzhou Tang, Jim Schnitzer, and Eric Jakobsson. Hierarchical approach to predicting permeation in ion channels. *Biophys. J.*, 81(5):2473 – 2483, 2001.

[187] S. Bek and E. Jakobsson. Brownian dynamics study of a multiply-occupied cation channel: application to understanding permeation in potassium channels. *Biophys. J.*, 66(4):1028 – 1038, 1994.

[188] R. P. Feynman, Robert B. Leighton, and Matthew Sands. The Feynman Lectures on Physics, 1963.

[189] Berk Hess, Carsten Kutzner, David van der Spoel, and Erik Lindahl. GROMACS 4: algorithms for highly efficient, load-balanced, and scalable molecular simulation. *J. Chem. Theor. Comput.*, 4(3):435–447, 2008. PMID: 26620784.

[190] Atomic resolution Brownian dynamics. `http://bionano.cpanel.engr.illinois.edu/arbd`. Online; accessed February 21, 2020.

[191] Glenn Moy, Ben Corry, Serdar Kuyucak, and Shin-Ho Chung. Tests of continuum theories as models of ion channels. i. Poisson-Boltzmann theory versus Brownian dynamics. *Biophys. J.*, 78(5):2349 – 2363, 2000.

[192] Taira Vora, Ben Corry, and Shin-Ho Chung. A model of sodium channels. *BBA*, 1668(1):106 – 116, 2005.

[193] Riccardo Mannella. Integration of stochastic differential equations on a computer. *Int. J. Mod. Phys. C*, 13(9):1177–1194, 2002.

[194] Nawaf Bou-Rabee. Time integrators for molecular dynamics. *Entropy*, 16(1):138–162, 2014.

[195] A. C. Brańka and D. M. Heyes. Algorithms for Brownian dynamics simulation. *Phys. Rev. E*, 58:2611–2615, Aug 1998.

[196] Michael P. Allen. Algorithms for Brownian dynamics. *Mol. Phys.*, 47(3):599–601, 1982.

[197] Kyu Il Lee, Sunhwan Jo, Huan Rui, Bernhard Egwolf, Benoît Roux, Richard W. Pastor, and Wonpil Im. Web interface for Brownian dynamics simulation of ion transport and its applications to beta-barrel pores. *J. Comput. Chem.*, 33(3):331–339, 2012.

[198] Ben Corry, Taira Vora, and Shin-Ho Chung. Electrostatic basis of valence selectivity in cationic channels. *BBA*, 1711(1):72 – 86, 2005.

[199] D G Luchinsky, R Tindjong, I Kaufman, P V E McClintock, and R S Eisenberg. Ion channels as electrostatic amplifiers of charge fluctuations. *J. Phys.: Conference Series*, 142:012049, dec 2008.

[200] L Pauling. *The Nature of Chemical Bond*. Cornell University Press, Ithaca, NY, 1942.

[201] Frank H. Stillinger and Aneesur Rahman. Improved simulation of liquid water by molecular dynamics. *The Journal of Chemical Physics*, 60(4):1545–1557, 1974.

[202] Benoît Roux, Simon Bernèche, and Wonpil Im. Ion channels, permeation, and electrostatics: Insight into the function of kcsa. *Biochemistry*, 39(44):13295–13306, 2000. PMID: 11063565.

[203] M. Hoyles, S. Kuyucak, and S.H. Chung. Energy barrier presented to ions by the vestibule of the biological membrane channel. *Biophys. J.*, 70(4):1628 – 1642, 1996.

[204] Amy Kaufman Katz, Jenny P. Glusker, Scott A. Beebe, and Charles W. Bock. Calcium ion coordination: A comparison with that of beryllium, magnesium, and zinc. *J. Amer. Chem. Soc.*, 118(24):5752–5763, 1996.

[205] S.M. Cosseddu, I.A. Khovanov, M.P. Allen, P.M. Rodger, D.G. Luchinsky, and P.V.E. McClintock. Dynamics of ions in the selectivity filter of the KcsA channel. *EPJ Special Topics*, 222(10):2595–2605, Oct 2013.

[206] Niraj Modi, Mathias Winterhalter, and Ulrich Kleinekathöfer. Computational modeling of ion transport through nanopores. *Nanoscale*, 4:6166–6180, 2012.

[207] M. L. Barabash, W. A. T. Gibby, C. Guardiani, D. G. Luchinsky, and P. V. E. McClintock. From the potential of the mean force to a quasiparticle's effective potential in narrow ion channels. *Fluct. Noise Lett.*, 18(02):1940006, 2019.

[208] S. Aboud, D. Marreiro, M. Saraniti, and R. Eisenberg. A poisson p3m force field scheme for particle-based simulations of ionic liquids. *Journal of Computational Electronics*, 3(2):117–133, Apr 2004.

[209] Aleksij Aksimentiev and Klaus Schulten. Imaging α-hemolysin with molecular dynamics: Ionic conductance, osmotic permeability, and the electrostatic potential map. *Biophys. J.*, 88(6):3745 – 3761, 2005.

[210] Andrey A. Gurtovenko. Asymmetry of lipid bilayers induced by monovalent salt: Atomistic molecular-dynamics study. *J. Chem. Phys.*, 122(24):244902, 2005.

[211] Lucie Delemotte, François Dehez, Werner Treptow, and Mounir Tarek. Modeling membranes under a transmembrane potential. *J. Phys. Chem. B*, 112(18):5547–5550, 2008. PMID: 18412411.

[212] S W De Leeuw, J W Perram, and E R Smith. Computer simulation of the static dielectric constant of systems with permanent electric dipoles. *Ann. Rev. Phys. Chem.*, 37(1):245–270, 1986. PMID: 21819241.

[213] Sanjib Senapati and Amalendu Chandra. Dielectric constant of water confined in a nanocavity. *J. Phys. Chem. B*, 105(22):5106–5109, 2001.

[214] L. Fumagalli, A. Esfandiar, R. Fabregas, S. Hu, P. Ares, A. Janardanan, Q. Yang, B. Radha, T. Taniguchi, K. Watanabe, G. Gomila, K. S. Novoselov, and A. K. Geim. Anomalously low dielectric constant of confined water. *Science*, 360(6395):1339–1342, 2018.

[215] Toshiya Ohtsuki and Koji Okano. Diffusion coefficients of interacting Brownian particles. *J. Chem. Phys.*, 77(3):1443–1450, 1982.

[216] Toby W. Allen, Serdar Kuyucak, and Shin-Ho Chung. Molecular dynamics study of the KcsA potassium channel. *Biophys. J.*, 77(5):2502 – 2516, 1999.

[217] Artem B. Mamonov, Maria G. Kurnikova, and Rob D. Coalson. Diffusion constant of K^+ inside Gramicidin A: A comparative study of four computational methods. *Biophys. Chem.*, 124(3):268 – 278, 2006. Ion Hydration Special Issue.

[218] Donald M. McQuarrie. *Statistical Mechanics*. University Science Books, Sausalito, California, USA, 2000.

[219] P.L. Paine and P. Scherr. Drag coefficients for the movement of rigid spheres through liquid-filled cylindrical pores. *Biophys. J.*, 15(10):1087 – 1091, 1975.

[220] M. Jardat, O. Bernard, P. Turq, and G. R. Kneller. Transport coefficients of electrolyte solutions from smart Brownian dynamics simulations. *J. Chem. Phys.*, 110(16):7993–7999, 1999.

[221] S.W. Chiu, J.A. Novotny, and E. Jakobsson. The nature of ion and water barrier crossings in a simulated ion channel. *Biophys. J.*, 64(1):98 – 109, 1993.

[222] Siu Cheung Li, Matthew Hoyles, Serdar Kuyucak, and Shin-Ho Chung. Brownian dynamics study of ion transport in the vestibule of membrane channels. *Biophys. J.*, 74(1):37 – 47, 1998.

[223] Britton W. Boras, Sophia P. Hirakis, Lane Votapka, Robert Malmstrom, Andrew McCulloch, and Rommie Amaro. Bridging scales through multiscale modeling: a case study on protein kinase A. *Front. Physiol.*, 6:250, 2015.

[224] G. Batôt, V. Dahirel, G. Mériguet, A. A. Louis, and M. Jardat. Dynamics of solutes with hydrodynamic interactions: Comparison between Brownian dynamics and stochastic rotation dynamics simulations. *Phys. Rev. E*, 88:043304, Oct 2013.

[225] E. Hairer. Variable time step integration with symplectic methods. *App. Numer. Math.*, 25(2):219 – 227, 1997. Special Issue on Time Integration.

[226] Arieh L. Edelstein and Noam Agmon. Brownian dynamics simulations of reversible reactions in one dimension. *The Journal of Chemical Physics*, 99(7):5396–5404, 1993.

[227] Jean Pierre Hansen and Ian R. McDonald. *Theory of simple liquids*. Academic Press Inc. (London) Ltd., 1976.

[228] Attila Malasics, Dirk Gillespie, and Dezső Boda. Simulating prescribed particle densities in the grand canonical ensemble using iterative algorithms. *J. Chem. Phys.*, 128(12):124102, 2008.

[229] Attila Malasics and Dezsö Boda. An efficient iterative grand canonical Monte Carlo algorithm to determine individual ionic chemical potentials in electrolytes. *J. Chem. Phys.*, 132(24):244103, 2010.

[230] Nicholas Metropolis, Arianna W. Rosenbluth, Marshall N. Rosenbluth, Augusta H. Teller, and Edward Teller. Equation of state calculations by fast computing machines. *J. Chem. Phys.*, 21(6):1087–1092, 1953.

[231] G. E. Norman and V. S. Filinov. Investigations of phase transition by a Monte Carlo method. *High Temp. (USSR)*, 7:216–222, 1969.

[232] Andreas Vitalis, Nathan A. Baker, and J. Andrew McCammon. ISIM: A program for grand canonical Monte Carlo simulations of the ionic environment of biomolecules. *Mol. Simul.*, 30(1):45–61, 2004.

[233] D.J. Adams. Grand canonical ensemble Monte Carlo for a Lennard-Jones fluid. *Mol. Phys.*, 29(1):307–311, 1975.

[234] John P. Valleau and L. Kenneth Cohen. Primitive model electrolytes. i. grand canonical monte Carlo computations. *J. Chem. Phys.*, 72(11):5935–5941, 1980.

[235] Yingting Liu and Fangqiang Zhu. Collective diffusion model for ion conduction through microscopic channels. *Biophys. J.*, 104(2):368 – 376, 2013.

[236] James C. Gumbart, Benoît Roux, and Christophe Chipot. Standard binding free energies from computer simulations: What is the best strategy? *J. Chem. Theory Comput.*, pages 201391794–802, 2012.

[237] Wolfgang Nonner, Alexander Peyser, and Bob Gillespie, Dirk Eisenberg. Relating microscopic charge movement to macroscopic currents: The Ramo-Shockley theorem applied to ion channels. *Biophys. J.*, 87:3716–3722, 2004.

[238] COMSOL MultiPhysics. `https://www.comsol.com/`. Online; accessed February 21, 2020.

[239] Dezsö Boda, Dirk Gillespie, Wolfgang Nonner, Douglas Henderson, and Bob Eisenberg. Computing induced charges in inhomogeneous dielectric media: Application in a Monte Carlo simulation of complex ionic systems. *Phys. Rev. E*, 69:046702, Apr 2004.

[240] S.O. Yesylevskyy and V.N. Kharkyanen. Hierarchy of motions and quasi-particles in a simplified model of potassium channel selectivity filter. *J. Biol. Phys.*, 30(2):187–201, Jun 2004.

[241] Valery N. Kharkyanen, Semen O. Yesylevskyy, and Natalia M. Berezetskaya. Approximation of super-ions for single-file diffusion of multiple ions through narrow pores. *Phys. Rev. E*, 82:051103, Nov 2010.

[242] M.L. Barabash, W.A.T. Gibby, C. Guardiani, D.G. Luchinsky, I. A. Khovanov, and P.V.E. McClintock. The dynamics of quasiparticles in a toy model of the KcsA biological ion channel. In *25^{th} International Conference of Noise and Fluctuations (ICNF)*, 2019. EasyChair Preprint no. 930.

[243] R. Elber, D. P. Chen, D. Rojewska, and R. S. Eisenberg. Sodium in gramicidin: an example of a permion. *Biophys. J.*, 68(3):906 – 924, 1995.

[244] T. Becker, K. Nelissen, B. Cleuren, B. Partoens, and C. Van den Broeck. Diffusion of interacting particles in discrete geometries: Equilibrium and dynamical properties. *Phys. Rev. E*, 90:052139, Nov 2014.

[245] Indira H. Shrivastava and Mark S.P. Sansom. Simulations of ion permeation through a potassium channel: molecular dynamics of KcsA in a phospholipid bilayer. *Biophys. J.*, 78(2):557 – 570, 2000.

[246] Z. Schuss. *Brownian dynamics at Boundaries and Interfaces: In Physics, Chemistry, and Biology.* Applied Mathematical Sciences. Springer New York, 2013.

[247] Michael Zwolak, Johan Lagerqvist, and Massimiliano Di Ventra. Quantized ionic conductance in nanopores. *Phys. Rev. Lett.*, 103:128102, Sep 2009.

[248] W. Clark Still, Anna Tempczyk, Ronald C. Hawley, and Thomas Hendrickson. Semianalytical treatment of solvation for molecular mechanics and dynamics. *J. Amer. Chem. Soc.*, 112(16):6127–6129, 1990.

[249] Michael S. Lee, Freddie R. Salsbury, and Charles L. Brooks. Novel generalized Born methods. *J. Chem. Phys.*, 116(24):10606–10614, 2002.

[250] John Mongan, Carlos Simmerling, J. Andrew McCammon, David A. Case, and Alexey Onufriev. Generalized Born model with a simple, robust molecular volume correction. *J. Chem. Theor. Comput.*, 3(1):156–169, 2007. PMID: 21072141.

[251] Subin Sahu and Michael Zwolak. Ionic selectivity and filtration from fragmented dehydration in multilayer graphene nanopores. *Nanoscale*, 9:11424–11428, 2017.

[252] C. Satheesan Babu and Carmay Lim. Theory of ionic hydration: Insights from molecular dynamics simulations and experiment. *J. Phys. Chem. B*, 103(37):7958–7968, 1999.

[253] Alexander A. Rashin and Barry Honig. Reevaluation of the Born model of ion hydration. *J. Phys. Chem.*, 89(26):5588–5593, 1985.

[254] Oliver Beckstein and Mark S. P. Sansom. Liquid–vapor oscillations of water in hydrophobic nanopores. *Proc. Nat. Acad. Sci. (USA)*, 100(12):7063–7068, 2003.

[255] Oliver Beckstein and Mark S P Sansom. The influence of geometry, surface character, and flexibility on the permeation of ions and water through biological pores. *Physical Biology*, 1(1):42–52, mar 2004.

[256] Oliver Beckstein, Kaihsu Tai, and Mark S. P. Sansom. Not ions alone: Barriers to ion permeation in nanopores and channels. *J. Amer. Chem. Soc.*, 126(45):14694–14695, 2004. PMID: 15535674.

[257] Pekka Mark and Lennart Nilsson. Structure and dynamics of the TIP3P, SPC, and SPC/E water models at 298 K. *J. Phys. Chem. A*, 105(43):9954–9960, 2001.

[258] John G. Kirkwood and Elizabeth Monroe Boggs. The radial distribution function in liquids. *J. Chem. Phys.*, 10(6):394–402, 1942.

[259] Gerhard Hummer and Dikeos Mario Soumpasis. Computation of the water density distribution at the ice-water interface using the potentials-of-mean-force expansion. *Phys. Rev. E*, 49:591–596, Jan 1994.

[260] I. Z. Fisher and B. L. Kopeliovich. Refinement of superposition approximation in the theory of liquids. *Dokl. Akad. Nauk SSSR*, 133:81–83, 1960.

[261] Fumio Hirata. *Molecular Theory of Solvation*. Kluwer Academic Publishers, Dordrecht, 2004.

[262] Michael Feig. *Modeling Solvent Environments: Applications to Simulations of Biomolecules*. WILEY-VCH Verlag GmbH & Co. KGaA, Weinheim, 2010.

[263] James C. Phillips, Rosemary Braun, Wei Wang, James Gumbart, Emad Tajkhorshid, Elizabeth Villa, Christophe Chipot, Robert D. Skeel, Laxmikant Kalé, and Klaus Schulten. Scalable molecular dynamics with NAMD. *J. Comput. Chem.*, 26(16):1781–1802, 2005.

[264] William L. Jorgensen, Jayaraman Chandrasekhar, Jeffry D. Madura, Roger W. Impey, and Michael L. Klein. Comparison of simple potential functions for simulating liquid water. *J. Chem. Phys.*, 79(2):926–935, 1983.

[265] MATLAB. `https://www.mathworks.com`. Online.

[266] Alan Grossfield. Dependence of ion hydration on the sign of the ion's charge. *J. Chem. Phys.*, 122(2):024506, 2005.

[267] Debra L. McCaffrey, Son C. Nguyen, Stephen J. Cox, Horst Weller, A. Paul Alivisatos, Phillip L. Geissler, and Richard J. Saykally. Mechanism of ion adsorption to aqueous interfaces: Graphene/water vs. air/water. *Proc. Nat. Acad. Sci. (USA)*, 114(51):13369–13373, 2017.

[268] Zhi Zhu, Chao Chang, Yousheng Shu, and Bo Song. Transition to a super-permeation phase of confined water induced by a terahertz electromagnetic wave. *J. Phys. Chem. Lett.*, 11(1):256–262, 2020. PMID: 31855440.

[269] Raúl Guerrero-Avilés and Walter Orellana. Energetics and diffusion of liquid water and hydrated ions through nanopores in graphene: ab initio molecular dynamics simulation. *Phys. Chem. Chem. Phys.*, 19:20551–20558, 2017.

[270] Carlo Guardiani, William A. T. Gibby, Miraslau L. Barabash, Dmitry G. Luchinsky, and Peter V. E. McClintock. Exploring the pore charge dependence of K^+ and Cl^- permeation across a graphene monolayer: a molecular dynamics study. *RSC Adv.*, 9:20402–20414, 2019.

[271] A. Esfandiar, B. Radha, F. C. Wang, Q. Yang, S. Hu, S. Garaj, R. R. Nair, A. K. Geim, and K. Gopinadhan. Size effect in ion transport through angstrom-scale slits. *Science*, 358(6362):511–513, 2017.

[272] Simone Furini and Carmen Domene. Selectivity and permeation of alkali metal ions in K^+-channels. *J. Mol. Biol.*, 409(5):867 – 878, 2011.

[273] Kaufman, Igor Kh., Fedorenko, Olena A., Luchinsky, Dmitri G., Gibby, William A.T., Roberts, Stephen K., McClintock, Peter V.E., and Eisenberg, Robert S. Ionic Coulomb blockade and anomalous mole fraction effect in the NaChBac bacterial ion channel and its charge-varied mutants. *EPJ Nonlinear Biomed. Phys.*, 5:4, 2017.

[274] Tzyy-Leng Horng, Robert S. Eisenberg, Chun Liu, and Francisco Bezanilla. Continuum gating current models computed with consistent interactions. *Biophys. J.*, 116(2):270 – 282, 2019.

[275] Michael J. Lenaeus, Tamer M. Gamal El-Din, Christopher Ing, Karthik Ramanadane, Régis Pomès, Ning Zheng, and William A. Catterall. Structures of closed and open states of a voltage-gated sodium channel. *Proc. Nat. Acad. Sci. (USA)*, 114(15):E3051–E3060, 2017.

[276] Kim Cooper, Eric Jakobsson, and Peter Wolynes. The theory of ion transport through membrane channels. *Prog. Biophys. Mol. Biol.*, 46(1):51 – 96, 1985.

[277] Max Born. Volumen und hydratation-swarme der ionen. *Z. Phys.*, 1:45–48, 1920.